Modelling the 2D-Raman-THz Response of Water – From Anharmonic Oscillators to All-Atom Molecular Dynamics

Dissertation
zur
Erlangung der naturwissenschaftlichen Doktorwürde
(Dr. sc. nat.)

vorgelegt der
Mathematisch-naturwissenschaftlichen Fakultät
der
Universität Zürich

von
David Sidler
aus
Nottwil LU

Promotionskommission
Prof. Dr. Peter Hamm (Vorsitz)
Prof. Dr. Jürg Hutter
Prof. Dr. Markus Meuwly

Zürich, 2020

Abstract

Most chemical reactions relevant for life occur in the presence of liquid water, where the rearrangement of its hydrogen bonding network plays an important role. 2D-Raman-THz spectroscopy is a novel spectroscopic technique, which can directly probe the intermolecular dynamics of this hydrogen bonding network [Proc. Natl. Acad. Sci. USA **110**, 20402 (2013)]. However, being a relatively new technique, its information content is not fully explored as to date.

Our journey started with the goal to develop a force field, which can quantitatively reproduce the experimental 2D-Raman-THz spectrum of liquid water. From such a force field, one could potentially understand the signal to full extent by detailed analysis of molecular dynamics trajectories. The starting point was TL4P – a polarizable force field, which was developed on the basis of mixed quantum-mechanical and empirical methods [J. Phys. Chem. B **117** , 9486 (2013)]. The dipole moment and polarizability surfaces of this force field were systematically modified in order to improve agreement with experimental THz absorption and Raman spectra. Namely, addition of intermolecular charge transfer increased the intensity of the hydrogen bond stretching mode in the THz absorption spectrum, whereas anisotropic molecular polarizability introduced the libration band in the Raman spectrum. We hypothesized that these corrections should also improve the 2D-Raman-THz signal. It was however found that the changes to the force field affect the signal in unpredicted ways. This unexpected behaviour is likely due to a process, in which intermolecular oscillations couple to diffusive motion.

Investigation of amorphous ice can give further insight into the origin of the 2D-Raman-THz signal of water, as it is structurally similar to liquid water, but follows simpler dynamics. Simulation of amorphous ice yields 2D-Raman-THz responses, which not only lack the diffusion signal, but also consist of well-separated, narrow features.

This motivated the interpretation of 2D-Raman-THz spectra from a completely different perspective, namely by using simple model systems based on harmonic oscillators. This allows for an intuitive description of spectral features based on energy level diagrams. It turns out that the signal of a truly harmonic system vanishes due to its strict selection rules, and the 2D-Raman-THz signal arises from anharmonicities, as well as from mode interactions. This simple model system was then extended to describe condensed phase systems and was finally applied for fitting the simulated amorphous ice responses. In this way, all spectral features produced by amorphous ice could be assigned to underlying microscopic processes. This detailed analysis suggests, that anharmonic couplings in-between hydrogen bond stretching modes constitute the major contribution to the simulated 2D-Raman-THz spectrum of amorphous ice.

Contents

Chapter 1

Introduction

Due to its ability to form a network of directional hydrogen bonds, water is a highly complex liquid. Rearrangement of the hydrogen bonding network, which is an essential part for aqueous solvation, is by itself a complicated process which involves opposing energetic and entropic driving forces being in a sensitive balance. Most chemical processes relevant for biology take place in water, where the role of water molecules is undeniably essential,[1] and water molecules can actively take part in biomolecular reactions. In-depth understanding of the solvent is crucial for the correct prediction of reaction pathways, as well as a variety of solvation effects (*e.g.* hydrophobic binding and Hoffmeister series). Even on its own, the behaviour of bulk water is quite puzzling, showing many anomalies compared to other liquids.[2–4]

1.1 Water Anomalies

Upon heating, most liquids expand in a monotonic fashion between freezing and boiling point. At the same time, they get more compressible. At higher pressure, the mobility of individual atoms is reduced due to confinement, which reflects in a smaller diffusion coefficient. For all of these properties water actually follows opposite trends at low temperature. Temperature dependent density is one of the first reported anomalous properties of water. The fact that ice floats on liquid water is by itself quite remarkable. Not only does water expand upon freezing, but already as it is cooled below 4°C (Figure 1.1*a*). Furthermore, water becomes more compressible upon cooling[8] (Figure 1.1*c*) , and the diffusion coefficient increases at high pressure[10] or upon confinement.[11] These are just some of many examples where water shows extraordinary behaviour.

In search of possible explanations for these anomalies, many different theories have been developed. For the correct description of turning points observed in the thermodynamic responses, liquid

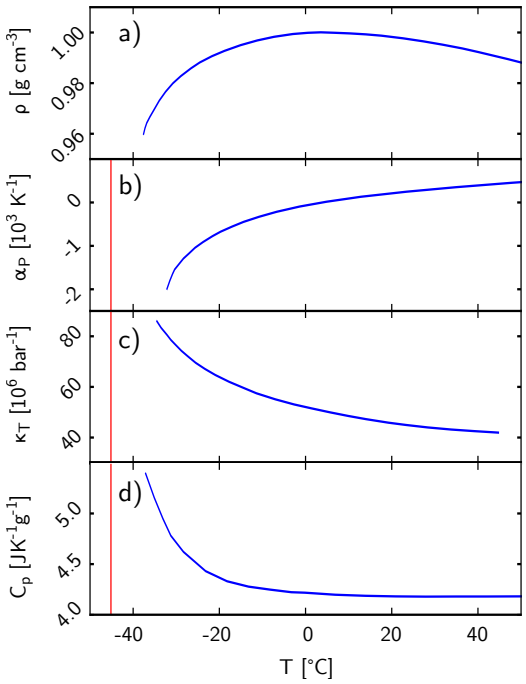

Figure 1.1: Thermodynamic properties of water, which show anomalous temperature dependence. *a*) Temperature dependent density, which shows a maximum at 4°C.[5] *b*) Thermal expansion coefficient[6,7] *c*) Isothermal compressibility,[8] and *d*) heat capacity,[9] which seem to diverge toward a temperature of -45°C (red line),

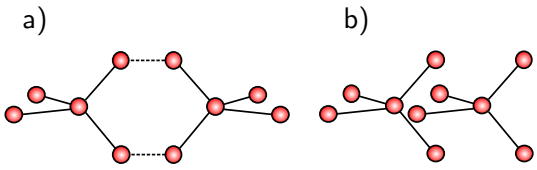

Figure 1.2: Illustration of local structure of *a*) low density and *b*) high density liquid water. Each red circle represents a water molecule.

water is assumed to be a mixture of at least two components. This raises questions about structure and dynamics of these components. Development of X-ray crystallography allowed to elucidate the crystal structure of ice.[12] In hexagonal ice, the molecules are arranged in a spacious tetrahedral structure. This explains the low density of hexagonal ice compared to liquid water. The tendency to form tetrahedral structures is an intrinsic property of water molecules. Based on this, one can speculate about local structure of liquid water. Water is assumed to be a mixture of low-density ice-like structures (Figure 1.2 *a*) and less ordered, high-density structures (Figure 1.2 *b*). Using this mixture model, the density curve is explained as follows: At low temperature, low density liquid is prevalent due to its stability. Upon heating, the ice-like structures collapse to a less ordered high-density liquid structure due to entropic effects. This is counteracted by the normal thermal expansion of both components. These two opposing effects produce a maximum in the temperature-dependent density.

A further breakthrough in the study of water anomalies was the measurement of thermodynamic properties in the supercooled regime below 0°C,[6] where the anomalies become more pronounced. Approaching a temperature of -45°C, various properties, such as the thermal expansion coefficient α_P (Figure 1*b*), isothermal compressibility κ_T (Figure 1*c*) and heat capacity C_p (Figure 1*d*) even seem to diverge. The question arises, what happens at this critical temperature. Different descriptions of water thereby predict different behaviour at this temperature.

In search of a unifying description of liquid water, three main hypotheses crystallized. The *stability limit hypothesis*[13] states that the spinodal line (line in the phase diagram, within which water can exist in its liquid state) is connected between the superheated and supercooled region over negative pressure region in the phase diagram (where water is stretched). Approaching this spinodal would lead to the divergence of thermodynamic properties. On the other hand, the *percolation model*,[14,15] which categorizes water molecules based on their connectivity, would rather predict a singularity free case. Despite hydrogen bonds being formed randomly (with a constant probability p), there is a spacial correlation between different types of water molecules (*i.e.* a four-fold coordinated species cannot be adjacent to a non-bonded species). Finally, the discovery of multiple glassy states of water (low density and high density amorphous ice) led to the hypothesis of *liquid to liquid phase transition* below a critical temperature.[16]

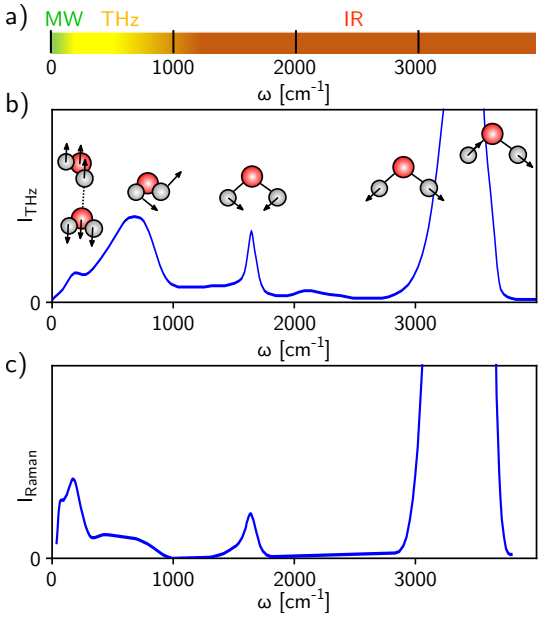

Figure 1.3: *a*) Spectral ranges covered by microwave (MW), terahertz (THz), and infrared (IR) spectroscopy. *b*) Vibrational absorption spectrum of liquid water (Ref. 21). The nuclear motion behind the different absorption modes is illustrated by arrows on the atoms. *c*) In Raman spectroscopy, the same modes are observed with different intensities (Ref. 22).

The temperature where one can directly distinguish the three cases is hardly accessible by experiment. Therefore, little experimental evidence exists for either hypothesis. Recent experiments[17] and simulations[18] support the presence of a liquid to liquid phase transition. Still, many question about the structure and dynamics of high density and low density liquid remain unanswered. The commonly accepted picture is that water molecules are on average tetrahedrally coordinated, with fast switching of hydrogen bonds. However, this picture is challenged by experimental[19] and theoretical work,[20] which states that water is on average two-fold coordinated. In this picture, chains of water molecules form strings or branched "polymers".

1.2 Vibrational Spectroscopy of Water

1.2.1 1D spectroscopy

Infrared (IR) spectroscopy of water directly observes the vibrational motion of its molecules (Figure 1.3 *b*). The main features in the water spectrum are the $3400\,\mathrm{cm}^{-1}$ band, which originates from symmetric and antisymmetric OH stretch-

ing modes, as well as a band around 1650 cm^{-1}, where bending modes appear. At frequencies below 1000 cm^{-1}, far IR and THz spectroscopy directly observe motions of the hydrogen bonding network. The THz spectrum of water contains three main features. Centered at 600 cm^{-1}, a broad feature of librations (hindered rotations) is present. A smaller band at 200 cm^{-1} is indicative of hydrogen bond stretching modes. Moreover, hydrogen bond bending modes are visible as a faint shoulder at 50 cm^{-1}. The local vibrational motions for the respective modes are illustrated in Figure 1.3 *b* (Keep in mind that these motions are realistically delocalized over several coordination shells[23]). At frequencies below 10 cm^{-1}, dielectric relaxation spectroscopy is able to observe relaxation processes. A maximum at 3.57 cm^{-1} indicates a relaxation time of 9.3 ps.[24–26] The presence of a second, faster relaxation process is speculated to originate from unbound water molecules. The same processes can be observed in Raman spectroscopy (Figure 1.3 *c*) where the same bands appear, but with different intensities.

The condensed phase spectral features are broadened due to the structure and dynamics of the local hydrogen bonding environment. If a water molecule is involved in hydrogen bonding, its intra-molecular bonds are weakened, which reduces the frequency of the OH stretching vibrations. The amount of red-shift is hereby related to the number of hydrogen bonds, and their respective strength. Therefore, the rich structure of the OH stretching mode directly reflects the complexity of the hydrogen bonding network (Figure 1.4, black line). In a more detailed analysis of the OH stretching mode, one could decompose the band into different Gaussian contributions, which each can be assigned to different local structures (Figure 1.4). Although this assignment is oversimplified (*e.g.* the OH stretching band contains both symmetric and antisymmetric contributions) it illustrates the structural information, which is potentially accessible in IR spectroscopy. The highly dynamic nature of liquid water reduces the structural resolution which can be obtained.

The structural and dynamic information about liquid water is hidden in the spectral line shapes. A spectral feature has a certain width, representing the range of frequencies which can be explored by an oscillator due to varying environment. Depending on the dynamics of the environment, we distinguish two limits. In *inhomogeneous broadening*, the frequency fluctuations are slow relative to the timescales of the experiment. In this case, one observes a distribution of oscillators which are distinguishable in principle (Figure 1.5 a). If the

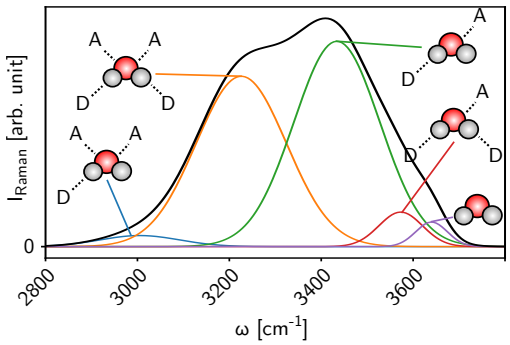

Figure 1.4: OH stretching band of the Raman spectrum and the decomposition into Gaussian contributions (adapted from ref. 27). The different sub-bands are related to the number of hydrogen bond donors (D) and acceptors (A).

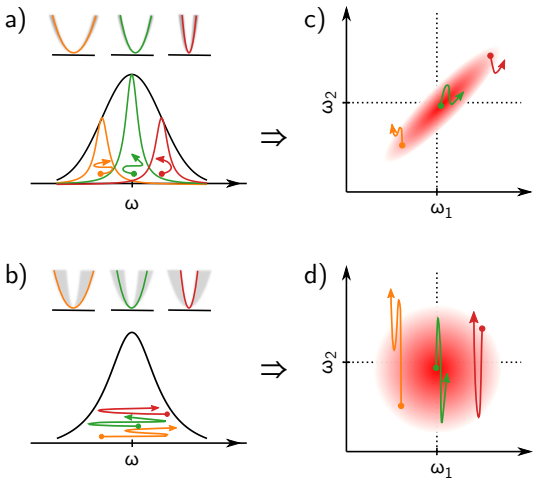

Figure 1.5: Broadening Mechanisms in 1D and 2D spectroscopy. Frequency fluctuations of three selected oscillators (orange, green, and red) during the waiting time T is illustrated as arrows in the same colors. *a*) Inhomogeneous and *b*) homogeneous broadening in 1D. *c*) Inhomogeneous and *d*) homogeneous broadening in 2D spectroscopy.

frequency fluctuations are fast compared to the experimental timescales, one speaks of *homogeneous broadening* (Figure 1.5 b). In this case, the different oscillators can interconvert so fast that they become indistinguishable. In 1D spectroscopy, these scenarios lead to very similar line shapes.

1.2.2 2D spectroscopy

In 2D IR spectroscopy, the oscillation frequency of the system is interrogated twice, therefore revealing additional information abut the structural dynamics of the system.[28,29] With a first laser pulse, one can selectively excite a sub-ensemble of oscillators at a given frequency ω_1 (this sub-ensemble

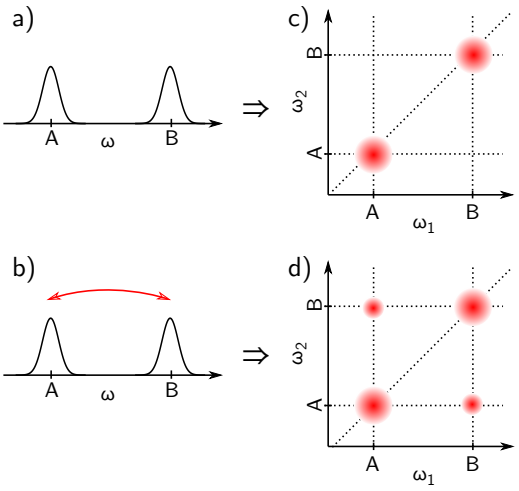

Figure 1.6: *a*) Two uncoupled modes lead to a *c*) set of two diagonal peaks in the 2D spectrum. *b*) On the other hand, two interacting modes lead to *d*) cross peaks in the 2D spectrum, which appear beside the diagonal peaks.

presumably has a distinct hydrogen bonding environment, such as illustrated in Figure 1.4). At a later time T, the frequency of this sub-ensemble is probed again. Since the environment can undergo fluctuations during this time, the frequency of the excited sub-ensemble randomizes to a certain extent. If the environment is quasi-static during T (inhomogeneous limit), the 2D spectrum will reveal a correlated peak (Figure 1.5 c). On the other hand, if the environment can fully rearrange during T (homogeneous limit), the frequencies fully randomize, which leads to an uncorrelated peak in the 2D spectrum (Figure 1.5 d). In that way, 2D spectroscopy can conclusively distinguish between homogeneous and inhomogeneous broadening.

Several examples exist, where the OH stretching mode is examined by 2D-IR spectroscopy in order to address assignment of sub-features within this band.[30–36] These experiments examine a mixtures of HOD and D_2O rather than pure H_2O in order to decouple the OH vibration from the other vibrations. In this case, the OH bond can be used as a local probe of the environment. Using different polarization geometries, one can furthermore separate rotational from structural dynamics during population time T. These methods see faster timescales for the high frequency portions of the OH stretching band. Similar experiments have been performed on the bending mode of water.[37]

As a further advantage, 2D IR spectroscopy is sensitive to the coupling between modes. Interaction of oscillators produce cross peaks in the 2D spectrum (Figure 1.6 d *versus* c). In the context of water, this has been applied to examine the interaction between intramolecular stretching and bending modes.[38–40]

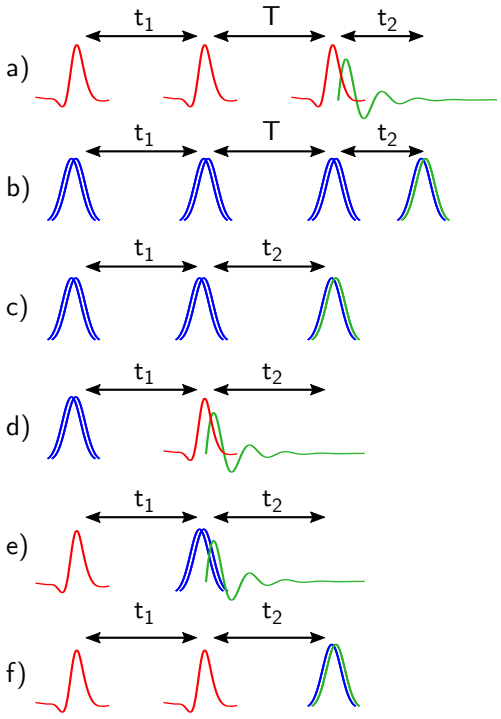

Figure 1.7: Pulse sequences for measuring 2D spectra in the THz range. The red pulses represent the THz fields, and the blue Gaussians show the envelopes of the Raman pulses. Green lines are the detected signal (Which can be either a low-frequency THz field, or a high frequency field in the Raman case). *a*) 2D-THz equivalent to 2D-IR, *b*) Raman-Echo, *c*) 2D-Raman spectroscopy. The two sequences *d*) RTT, and *e*) TRT, which constitute 2D-Raman-THz spectroscopy, and the complementary *f*) TTR sequence.

1.2.3 2D Spectroscopy in THz Range

THz spectroscopy directly probes motion of the hydrogen bonding network. The bands in the THz spectrum are strongly overlapping, which renders the assignment of different sub-bands difficult. Spreading out the THz spectrum into two dimensions can potentially increase the resolution, which would simplify the assignment of sub-bands. Moreover, 2D spectroscopy in THz range potentially brings along information about the inhomogeneity of the hydrogen bonding network in liquid water (Figure 1.5),[41] as well as the coupling between intermolecular modes (Figure 1.6).

The most obvious approach to measure 2D spectra in THz range would be to take the same approaches already established in 2D IR spec-

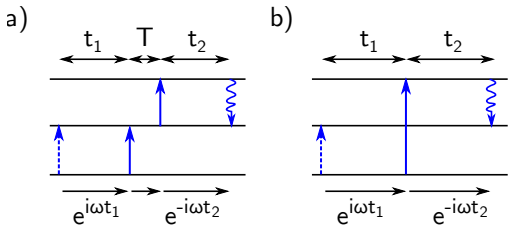

Figure 1.8: The pathways which are responsible for the echo signal in *a)* third order perturbation theory, and *b)* second order perturbation theory. Due to the missing interaction in second order perturbation theory, one of the interactions needs to induce a two-quantum transition.

troscopy, but replacing the IR pulses with THz pulses. In this 2D-THz experiment, the system is excited by three THz pulses (Figure 1.7 a). The first two pulses are separated by time t_1. After a waiting time T, the system is perturbed by an additional THz pulse. The emitted signal, which is third order in the THz field, can be detected at time t_2 after the last pulse. This experiment can also be performed in a simplified pump-probe geometry, where the second and third interaction are caused by the same laser pulse (and therefore $T = 0$). THz technology is yet in its infancy,[42] and it is still a technical challenge to produce the short THz pulses which are necessary for 2D-THz spectroscopy. Due to the low power of available THz pulses, 2D-THz spectroscopy has only been applied to a few selected systems, which have large transition dipole moments.[43–48]

Even before the emergence of THz technology, low frequency vibrations could be observed by non-resonant interaction with light. In Raman spectroscopy, the incident non-resonant light can excite vibrational states of the system. The frequency of the scattered light is thereby modified in order to conserve energy. In this way, the vibrational energies are imprinted in the frequency shifts of the scattered light.[49] With the help of short non-resonant laser pulses, the same nuclear dynamics can be observed in time-domain (as the optical Kerr effect).[50–57] In this approach, the system is perturbed by a non-resonant laser pulse. The so induced nuclear dynamics can be recorded in time-domain by a probe-pulse. Additional non-resonant pulses can be used in order to record 2D spectra. The non-resonant equivalent to 2D-IR spectroscopy is the Raman-Echo experiment (Figure 1.7 b). If all three interactions are replaced by non-resonant interactions, the resulting response is 7^{th} order in the electric field. As such, it yields a very small signal.[58–60] Application to liquid water is further hindered due to its small Raman cross-section.

The idea of performing multidimensional Raman spectroscopy in order to investigate the inhomogeneity of liquids has been elaborated by Y. Tanimura and S. Mukamel. In their work, they proposed the 5^{th} order 2D-Raman spectroscopy (Figure 1.7 c).[61] Compared to the previously mentioned 2D methods, 2D-Raman spectroscopy has one interaction less. Therefore, the physical background behind the signal is slightly different (Figure 1.8 b *versus* a). This promising method attracted much interest from both experimental,[62–67] as well as from theoretical side.[68–76] It has been found that the signal is dominated by cascading third order signals, which obscure the view on the higher order dynamics. Consequently, much effort went into the elimination of these artefacts. Due to these technical difficulties, 2D-Raman spectroscopy has not been applied to water with its relatively low Raman activity.

Hybrid 2D-Raman-THz spectroscopy has been proposed as an alternative method, which prevents these unwanted cascades. In this method, the system is perturbed once with a resonant THz pulse, and once with a non-resonant pulse, separated by a time t_1. The emitted THz field is then recorded after time t_2 (Figure 1.7 d and e). The resulting signal is third order in electric field. Because it has only one Raman interaction, it can also be applied to liquids with low Raman cross-sections. Moreover, THz pulse power is less critical than for the 2D-THz experiment, since the system is perturbed only once by a THz pulse. The 2D-Raman-THz experiment can detect three different pulse sequences, RTT (Figure 1.7 d), TRT (Figure 1.7 e), and TTR (Figure 1.7 f). By means of 2D-Raman-THz spectroscopy, the higher order dynamics of liquid water could finally be recorded.[77,78] It has been furthermore applied to the measurement of aqueous salt solutions,[79] as well as halogenated liquids.[80] The TTR pulse sequence (Figure 1.7 f) has a different detection scheme and as such cannot be measured with the same instrument. THz-THz-Raman spectroscopy has been successfully applied to halogenated liquids and solid-state systems.[81–84]

1.3 2D-Raman-THz Spectroscopy of Water

1.3.1 Experiment

The 2D-Raman-THz signal of liquid water has been recorded in our group with the following experimental setup (Figure 1.9):[77] Ultrashort 800 nm

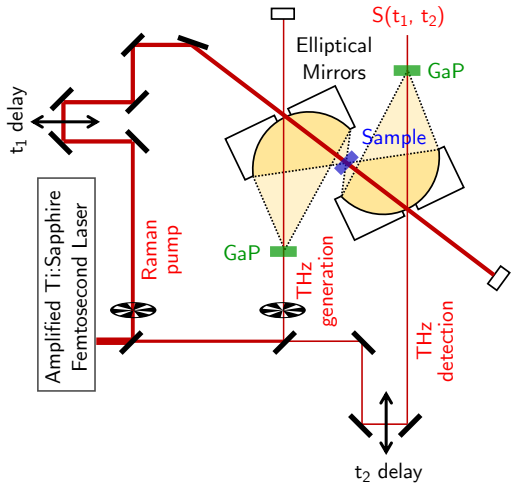

Figure 1.9: Experimental setup for recording the 2D-Raman-THz signal.

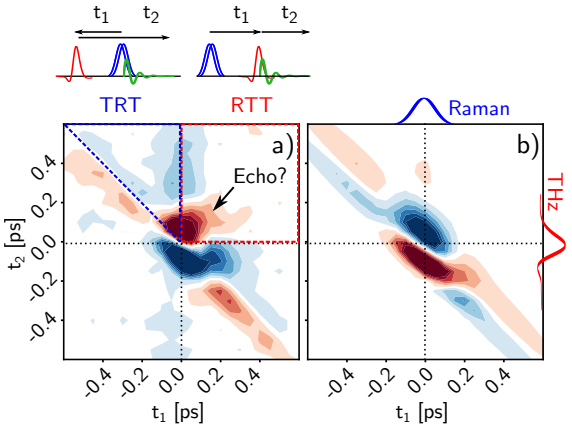

Figure 1.10: *a*) Experimental 2D-Raman-THz response of liquid water *b*) . Instrument response function of the 2D-Raman-THz experiment.

pulses are generated by an amplified Ti:Sapphire femtosecond laser source. With the use of beam-splitters, the light is split into three paths: Raman pump, THz generation, and THz detection path. The 800 nm Raman pump pulse runs over a delay stage, where its delay time relative to the THz excitation is controlled (t_1) and is then focussed onto the sample. In the THz generation path, the 800 nm pulse travels through a gallium phosphite (GaP) crystal, in which a THz field is generated by optical rectification.[85,86] In this nonlinear process, the incident oscillating field generates a DC component, roughly in the shape of the pulse envelope of incident light. By means of elliptical mirrors the THz pulse is focussed onto the sample, collected, and then re-focussed through a second GaP crystal, where the modified THz field is detected by electrooptic sampling. In this process, the THz light causes birefringence in the GaP crystal, which is detected at time t_2 by the 800 nm pulse from the THz detection path.

If the THz pulse arrives at the sample after the Raman pulse ($t_1 > 0, t_2 > 0$), one records the RTT pulse sequence, which appears in the upper right quadrant of the signal (Figure 1.10 a, red quadrant). If, on the other hand, the THz pulse arrives before the Raman pulse ($t_1 < 0$, $t_2 > -t_1$) the TRT sequence is recorded (Figure 1.10 a, blue quadrant). The obtained signal results from a convolution of the molecular response with the laser pulses. The effect of the laser pulses alone (assuming the molecular response is instantaneous) is given by the instrument response function

$$I(t_1, t_2) = \frac{d}{dt_2} I_{\text{Raman}}(t_1 + t_2) E_{\text{THz}}(t_2), \qquad (1.1)$$

which is illustrated in Figure 1.10 b. The water signal (Figure 1.10 a) shows additional features protruding from the instrument response. In the center of attention is the signal extending along the $t_1 = t_2$ diagonal in the RTT quadrant. This so-called echo signal is the time-domain analogue to elongated line shapes in frequency domain (Figure 1.5 c). Thus, the lifetime of the echo signal gives direct insight into the inhomogeneity of the sample. Studying the echo lifetimes at different temperatures, and in the presence of different solutes led to new insight about the dynamics of liquid water.[78,79]

1.3.2 Theory

The experimental 2D-Raman-THz signal of water contains more information than what is currently interpreted. This calls for further theoretical investigation. Beside current efforts to describe 2D-Raman-THz spectroscopy,[87–92] many theoretical considerations have been made already in the context of 2D-Raman spectroscopy. The theoretical basis is given by time-dependent perturbation theory. In this formulation, the 2D-Raman-THz responses are given by the nested commutators[93]

$$\begin{aligned} R_{RTT} &= -\text{Tr}\{\hat{\mu}(t_1 + t_2)[\hat{\mu}(t_1), [\hat{\alpha}(0), \rho_{eq}]]\} \\ R_{TRT} &= -\text{Tr}\{\hat{\mu}(t_1 + t_2)[\hat{\alpha}(t_1), [\hat{\mu}(0), \rho_{eq}]]\} \\ R_{TTR} &= -\text{Tr}\{\hat{\alpha}(t_1 + t_2)[\hat{\mu}(t_1), [\hat{\mu}(0), \rho_{eq}]]\}. \end{aligned} \qquad (1.2)$$

In order to calculate spectra, one needs to know energy levels (which define the time-evolution of the system ρ), dipole moment $\hat{\mu}$, and polarizability $\hat{\alpha}$ of the system. Such a model system can be defined in many different ways. Here, we will discuss two fundamentally different approaches.

If a system is near a minimum of its potential energy surface (*e.g.* at low temperature), its motion

can be approximated as the independent oscillations of normal modes. The spectral response of a single normal mode can be determined using the quantum harmonic oscillator model. This leads to an intuitive description of the response based on energy level diagrams. It turns out that the signal of a truly harmonic system vanishes due to its strict selection rules, and the 2D-Raman-THz signal arises from anharmonicities, as well as from mode interactions. The full range of possible responses can be explored by 1D and 2D oscillator models. This abstraction allows us to ignore the complex molecular systems behind the normal modes and concentrate on the essential system properties. Such oscillator models have been studied in the context of 2D-Raman spectroscopy,[68,69,71,73,74] as well as for hybrid IR-Raman methods.[93,94]

In a different approach, the spectral responses are derived from realistic molecular structures and motion.[70,72,73,75,76] In molecular dynamics (MD) simulations, the system moves on a potential energy surface which is usually fitted to reproduce structure and thermodynamic properties of the real system. Dipole moment and polarizability of the system are derived from a set of atomic charges and polarizable sites. Since the responses are derived from realistic structures and dynamics, this method intrinsically produces reasonable spectral line shapes. Moreover, this method considers various symmetry aspects of the system. On the downside, it comes at much higher cost. A study of different polarizable water force fields has shown that the signal is very sensitive to the details of the force field, especially on the treatment of polarizability.[89,92] To date, no force field could quantitatively reproduce the experimental response. A polarizable water forcefield is needed, which accurately describes potential energy, dipole and polarizability of the system.

1.4 Outline

This work builds on previous theoretical considerations of 2D-Raman and 2D-Raman-THz spectroscopy with the goal to understand the experimental 2D-Raman-THz signal of liquid water. In a first part, simple oscillator models are used in order to explore the range of possible 2D-Raman-THz signal. The effects of mechanical and electrical anharmonicity are studied on the example of a 1D oscillator (Chapter 2). The anharmonicities are thereby treated perturbatively. This allows us to express the responses as a linear combination of "basis responses", whose peak patterns are characteristic for the type of anharmonicity. Interaction between modes by mechanical and electrical couplings result in cross-peak patterns. These effects are studied on the basis of a 2D oscillator model (Chapter 3). In a different approach, the 2D-Raman-THz responses are calculated from MD simulations. A study of different force fields advocated for the TL4P force field.[89,95] Based on TL4P, a series of force fields is developed, which selectively correct features of the 1D THz and Raman spectra of liquid water (Chapter 4). These force fields are then applied to derive 2D-Raman-THz signals in a range of conditions, from liquid water to amorphous ice (Chapter 5). The amorphous ice spectra, which are rich in long-lived oscillations, are interpreted by the coupled oscillator model (Chapter 6). This allows for a detailed understanding of simulated spectra.

Chapter 2

Feynman Pathways of 1D Oscillators

The content of this chapter has been published under the title "Feynman Diagram Description of 2D-Raman-THz Spectroscopy Applied to Water" [D. Sidler, P. Hamm, *J. Chem. Phys* **150**, 044202 (2019)]

2.1 Abstract

2D-Raman-THz spectroscopy of liquid water, which has been presented recently [Proc. Natl. Acad. Sci. USA **110**, 20402 (2013)], directly probes the intermolecular degrees of freedom of the hydrogen-bond network. However, being a relatively new technique, its information content is not fully explored as to date. While the spectroscopic signal can be simulated based on molecular dynamics simulation in connection with a water force field, it is difficult to relate spectroscopic signatures to the underlying microscopic features of the force field. Here, a completely different approach is taken that starts from an as simple as possible model, i.e., a single vibrational mode with electrical and mechanical anharmonicity augmented with homogeneous and inhomogeneous broadening. An intuitive Feynman diagram picture is developed for all possible pulse sequences of hybrid 2D-Raman-THz spectroscopy. It is shown that the model can explain the experimental data essentially quantitatively with a very small set of parameters, and it is tentatively concluded that the experimental signal originates from the hydrogen-bond stretching vibration around $170\,\mathrm{cm}^{-1}$. Furthermore, the echo observed in the experimental data can be quantified by fitting the model. A dominant fraction of its linewidth is attributed to quasi-inhomogeneous broadening in the slow-modulation limit with a correlation time of 370 fs, reflecting the lifetime of the hydrogen-bond networks giving rise the absorption band.

2.2 Introduction

THz spectroscopy of liquids probes their intermolecular modes directly. Applied to liquid water, it reveals three distinct bands, which are assigned to hydrogen bond bending modes ($50\,\mathrm{cm}^{-1}$), hydrogen bond vibrations ($170\,\mathrm{cm}^{-1}$), and librations, which are hindered rotations of water molecules ($600\,\mathrm{cm}^{-1}$).[21] These spectra can give us a picture of the motions in water, however, vibrational coherences are very short lived in water due to the fast, chaotic dynamics of the hydrogen bonding network, causing very broad and blurred bands. This limits the amount of information that can effectively be extracted from these spectra.

Extending the spectroscopy into two dimensions can thin out the information, and thus increase the amount of accessible information, and can furthermore disentangle homogeneous from inhomogeneous broadening.[61,71] There has been significant effort to extend the very concept of 2D spectroscopy into the THz regime, either in the form of 2D Raman spectroscopy,[58,59,62–67,96,97] 2D-THz spectroscopy,[43–48] or hybrid 2D-Raman-THz methods.[79,81,82,98] Due to technical limitations, the latter is as of now the only 2D spectroscopy in the THz range that has been successfully applied to water and aqueous salt solutions.[78,79,98] Of particular interest in these experiments is the observation of a very short-lived echo, whose decay time has been related to the relevant time-scales in water. However, a detailed understanding of the 2D-Raman-THz response is still lacking.

Unlike conventional 2D IR spectroscopy,[29] 2D-Raman spectroscopy as well as 2D-Raman-THz spectroscopy are described by second-order perturbation theory, despite the fact that it is a 3rd-order response with regard to the electrical fields. This is since the Raman process is electronically non-resonant and thus instantaneous, and it is assumed that the two field interactions giving rise to the Raman process occur at the same time. The three instead of four interactions of the system (includ-

ing the emission process) bring about that one has to induce a two-quantum transition, which would be forbidden in the harmonic approximation. This forbidden transition is a bottleneck of the signal, which is why its very cause (i.e., electrical or mechanical anharmonicity) determines the shape of the signal. Thus, the two-quantum transition must be an integral part of any model used to describe 2D-Raman-THz spectroscopy.

Time dependent perturbation theory is the starting point to calculate the 2D-Raman-THz response. The response functions for the three different time-orderings are:[93]

$$\begin{aligned} R_{\mathrm{RTT}} &= -\mathrm{Tr}\{\hat{\mu}(t_1+t_2)[\hat{\mu}(t_1),[\hat{\alpha}(0),\rho_{\mathrm{eq}}]]\} \\ R_{\mathrm{TRT}} &= -\mathrm{Tr}\{\hat{\mu}(t_1+t_2)[\hat{\alpha}(t_1),[\hat{\mu}(0),\rho_{\mathrm{eq}}]]\} \\ R_{\mathrm{TTR}} &= -\mathrm{Tr}\{\hat{\alpha}(t_1+t_2)[\hat{\mu}(t_1),[\hat{\mu}(0),\rho_{\mathrm{eq}}]]\} \end{aligned} \tag{2.1}$$

where $\hat{\mu}$ is the dipole operator, $\hat{\alpha}$ the polarizability operator, t_1 the time between the first and the second laser pulse interacting with the sample, and t_2 the time from the second laser pulse to the detection process. We have concentrated on the Raman-THz-THz (RTT) and the THz-Raman-THz (TRT) pulse sequences,[41,78,79,87–89,98] where the detection step measures an emitted THz field, while Blake and coworkers looked at the THz-THz-Raman (TTR) pulse sequence with a Raman process for detection.[81,82]

The theory of 2D-Raman-THz spectroscopy is similar to 2D-Raman spectroscopy,[61,68–76] as well as hybrid IR-Raman techniques.[93,94,99–101] In addition, a fair share of theory has been published tailored specifically for 2D-Raman-THz spectroscopy.[87–92,102–104] Since typical THz experiments work in a frequency range equivalent to k_BT, the response can be derived in the classical limit from molecular dynamics (MD) simulation.[76] This approach appears to be the method of choice for complicated systems like water, since basically all effects, apart from possible quantum effects,[78] are captured implicitly by a MD force field, including anharmonicities, mode coupling, chemical exchange, and orientational averaging. It has been shown that the MD approach reveals responses, which strongly depend on the force field used, especially on the description of polarizability, albeit in a rather nonintuitive and indirect way.[89,102] These MD simulations are largely "black-box" and it is difficult to disentangle the contributions to the 2D-Raman-THz response and to relate spectroscopic signatures to the underlying microscopic features of a water force field.

In order to learn more about the microscopic mechanism giving rise to the 2D-Raman-THz response, we take a completely different approach here and start from an as simple as possible model, i.e., a single vibrational mode augmented with homogeneous and inhomogeneous broadening. To that end, we follow the conceptual framework introduced in Ref. 74 for the description of 2D Raman spectroscopy, starting from a quantum-mechanical harmonic oscillator in an eigenstate representation and adding electrical and/or mechanical anharmonicity. The response functions Eq. 2.1 can then be depicted in a very intuitive way in terms of Feynman diagrams, from which one can directly read off the peak position in a 2D spectrum. We will see that the model can explain the experimental data essentially quantitatively with a small set of parameters.

2.3 Model System

2.3.1 Zero-Order Description: Harmonic oscillator

Due to its simplicity and the fact that it is often a very good approximation for molecular vibrations, the harmonic oscillator is an obvious starting point to set the stage:

$$\hat{H}^{(0)} = \frac{\hbar\omega}{2}\left(\hat{p}^2+\hat{q}^2\right). \tag{2.2}$$

Analytical solutions of energy levels and eigenfunctions exist. From the thermal population of eigenstates, the equilibrium density matrix ρ_{eq} in Eq. 2.1 can readily be constructed. Furthermore, the dimensionless position operator $\hat{q} = \sqrt{\frac{m\omega}{\hbar}}\hat{x}$ can be expressed in an harmonic oscillator eigenstate basis $|\varphi_i\rangle$

$$(\boldsymbol{q_H})_{ij} \equiv \langle\varphi_i|\hat{q}|\varphi_j\rangle = \tfrac{1}{\sqrt{2}}\left[\sqrt{j}\delta_{i+1,j}+\sqrt{i}\delta_{i-1,j}\right] \tag{2.3}$$

(where the subscript in $\boldsymbol{q_H}$ stands for "harmonic"), which can be seen from the common creation ($\hat{b}$) and annihilation ($\hat{b}^\dagger$) operator formalism with $\hat{q} = 1/\sqrt{2}(\hat{b}^\dagger+\hat{b})$.[105] With that, the dipole and polarizability operators can be expanded in $\boldsymbol{q_H}$:

$$\begin{aligned} \boldsymbol{\alpha} &\propto \boldsymbol{q_H} + ... \\ \boldsymbol{\mu} &\propto \boldsymbol{q_H} + ... \end{aligned} \tag{2.4}$$

The proportionality factors are irrelevant for the purpose of this paper, as they give rise to an overall intensity of the 2D-Raman-THz signal, which however is typically not determined experimentally in an absolute sense. The $\delta_{i+1,j}$ and $\delta_{i-1,j}$ terms in $\boldsymbol{q_H}$ couple states i and $i\pm1$, which leads to the well-known $i \rightarrow i\pm1$ selection rules of the harmonic oscillator. This level of description is often sufficient to describe linear (1D) THz or Raman spectroscopy.

The $i \rightarrow i \pm 1$ selection rules cause coherence pathways, in which the density matrix is alternating between population and coherence states. As one starts from a thermal population state ρ_{eq}, an even number of interactions would be needed to return to a population state after the emission of a signal. Therefore, due to the odd number of interactions in 2D-Raman-THz spectroscopy, the harmonic oscillator together with Eq. 2.4 would predict a vanishing signal. The appearance of a signal requires zero- or two-quantum transitions, which can be accomplished by breaking the symmetry of the system; either by considering nonlinearity of $\boldsymbol{\mu}$ and $\boldsymbol{\alpha}$ (electrical anharmonicity), or by perturbing the potential of the oscillator (mechanical anharmonicity). Softening the selection rules results in a bottleneck for the response, hence the signal shape is very sensitive to the specific nature of the anharmonicity, which thus is a crucial aspect of the modelling of 2D-Raman-THz spectra.

2.3.2 Electrical Anharmonicity

Electrical anharmonity is introduced by considering higher order terms in equation Eq. (2.4):[74]

$$\begin{aligned}\boldsymbol{\alpha} &\propto \boldsymbol{q_H} + \sigma_\alpha \boldsymbol{q_H}^2 + ... \\ \boldsymbol{\mu} &\propto \boldsymbol{q_H} + \sigma_\mu \boldsymbol{q_H}^2 + ...\end{aligned} \tag{2.5}$$

with dimensionless smallness parameters $|\sigma_\mu| \ll 1$ and/or $|\sigma_\alpha| \ll 1$. In an harmonic eigenstate basis, the quadratic term is:

$$(\boldsymbol{q_H}^2)_{ij} = \tfrac{1}{2}\Big[(2i+1)\delta_{i,j} + \sqrt{(i+1)(i+2)}\delta_{i,j-2} + \sqrt{(j+1)(j+2)}\delta_{i,j+2}\Big], \tag{2.6}$$

which again can be seen from the creation/annihilation operator formalism.[105] In analogy to an electrical quadrupole transition, the $\delta_{i,j}$-term allows for zero-quantum transitions $i \rightarrow i$, and the $\delta_{i,j\pm2}$-terms for two-quantum transitions $i \rightarrow i \pm 2$.

2.3.3 Mechanical Anharmonicity

Mechanical anharmonicity (which has not been considered in Ref. 74) breaks the symmetry by modifying the potential energy function. We consider a cubic anharmonic oscillator by adding $\sigma_{\mathrm{M}}\hbar\omega q^3$ to the harmonic Hamiltonian:

$$\hat{H} = \hat{H}^{(0)} + \sigma_{\mathrm{M}}\hbar\omega q^3 \tag{2.7}$$

with dimensionless smallness parameter $|\sigma_{\mathrm{M}}| \ll 1$. The eigenstates of the anharmonic oscillator $|\varphi_i^{(anh)}\rangle$ can be calculated perturbatively.[106] Although the position operator $\hat{q}$ *per se* is not affected by this addition, its matrix representation in an anharmonic eigenstate basis is. It can be shown (see Appendix 2.6) that this matrix representation takes the form $\langle\varphi_i^{(anh)}|\hat{q}|\varphi_j^{(anh)}\rangle = (\boldsymbol{q_H})_{ij} + \sigma_{\mathrm{M}}(\boldsymbol{q_M})_{ij}$ with:

$$(\boldsymbol{q_M})_{ij} = \tfrac{1}{2}\Big[-3(2i+1)\delta_{i,j} + \sqrt{(i+1)(i+2)}\delta_{i,j-2} + \sqrt{(j+1)(j+2)}\delta_{i,j+2}\Big], \tag{2.8}$$

where the subscript "M" stands for "mechanic anharmonicity". $\boldsymbol{q_M}$ has the same structure as $\boldsymbol{q_H}^2$ (Eq. 2.6) with the $\delta_{i,j}$-term causing zero-quantum transitions and the $\delta_{i,j\pm2}$-terms causing two-quantum transitions, however the prefactors determining the transition probabilities and the signs of the peaks are different.

For a system with mechanical and electrical anharmonicity at the same time, the operators are:

$$\begin{aligned}\boldsymbol{\alpha} &= \boldsymbol{q_H} + \sigma_{\mathrm{M}}\boldsymbol{q_M} + \sigma_\alpha\left(\boldsymbol{q_H} + \sigma_{\mathrm{M}}\boldsymbol{q_M}\right)^2 \\ &\approx \boldsymbol{q_H} + \sigma_{\mathrm{M}}\boldsymbol{q_M} + \sigma_\alpha \boldsymbol{q_H}^2 \\ \boldsymbol{\mu} &= \boldsymbol{q_H} + \sigma_{\mathrm{M}}\boldsymbol{q_M} + \sigma_\mu\left(\boldsymbol{q_H} + \sigma_{\mathrm{M}}\boldsymbol{q_M}\right)^2 \\ &\approx \boldsymbol{q_H} + \sigma_{\mathrm{M}}\boldsymbol{q_M} + \sigma_\mu \boldsymbol{q_H}^2\end{aligned} \tag{2.9}$$

where we neglected in the second step terms that are higher than first order in any of the smallness parameters σ_μ, σ_α and σ_{M}. For the same reason, we also neglect coherence pathways that contain more than one forbidden transition.

2.3.4 Feynman Diagrams

Based on Eq. 2.9, the response functions of Eq. 2.1 can be separated into:

$$\begin{aligned}R_{\mathrm{RTT}} &\propto \sigma_\alpha R^\alpha_{\mathrm{RTT}} + \sigma_\mu R^\mu_{\mathrm{RTT}} + \sigma_{\mathrm{M}} R^{\mathrm{M}}_{\mathrm{RTT}} \\ R_{\mathrm{TRT}} &\propto \sigma_\alpha R^\alpha_{\mathrm{TRT}} + \sigma_\mu R^\mu_{\mathrm{TRT}} + \sigma_{\mathrm{M}} R^{\mathrm{M}}_{\mathrm{TRT}} \\ R_{\mathrm{TTR}} &\propto \sigma_\alpha R^\alpha_{\mathrm{TTR}} + \sigma_\mu R^\mu_{\mathrm{TTR}} + \sigma_{\mathrm{M}} R^{\mathrm{M}}_{\mathrm{TTR}}\end{aligned} \tag{2.10}$$

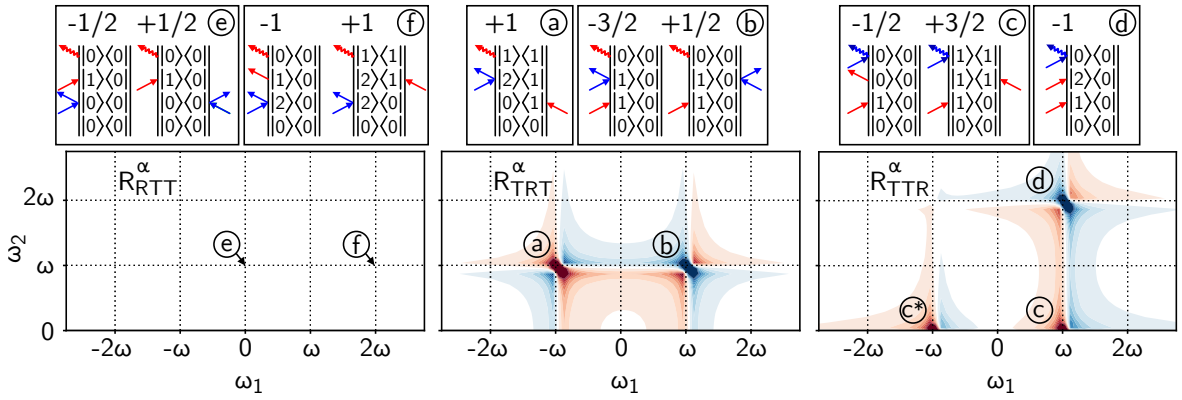

Figure 2.1: Feynman diagrams and 2D frequency-domain spectra of $R^{\alpha}_{\mathrm{RTT}}$ (left), $R^{\alpha}_{\mathrm{TRT}}$ (middle) and $R^{\alpha}_{\mathrm{TTR}}$ (right), showing the real part. The various 2D peaks are labeled with letters and the corresponding Feynman diagrams are shown above the spectra with THz interactions depicted in red and the Raman interaction as blue double-arrow. The weighting factor of each pathway is denoted above the Feynman diagram. The respons-e functions were exponentially damped according to Eq. 2.14 with a time-constant long enough (i.e., $T_1 = 12\omega^{-1}$) so that all peaks are resolved. Peak (c*) is the conjugate complex of peak (c).

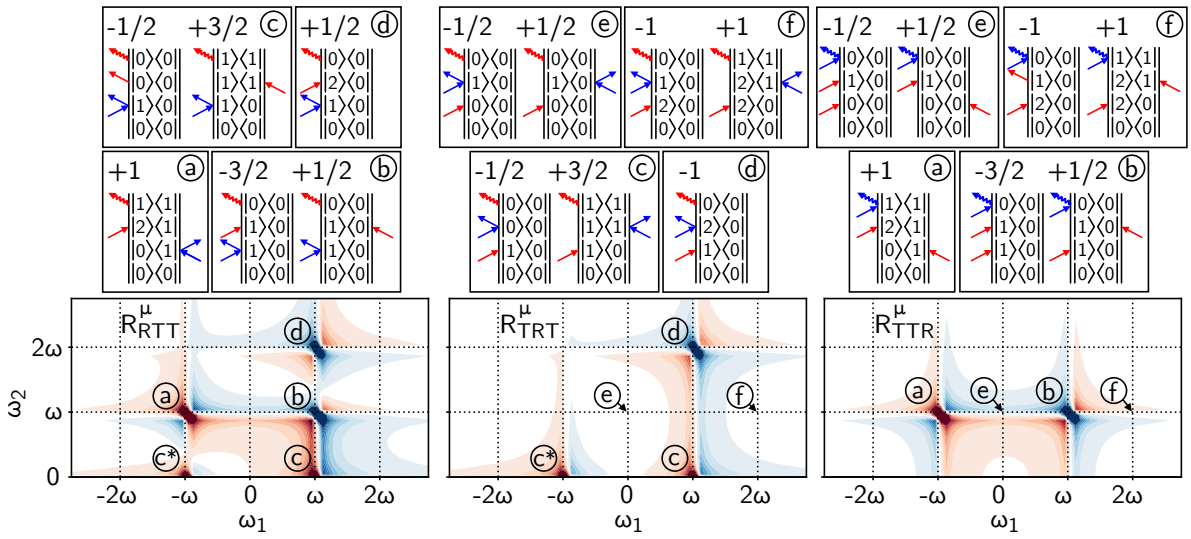

Figure 2.2: Feynman diagrams and 2D frequency-domain spectra of R^{μ}_{RTT} (left), R^{μ}_{TRT} (middle) and R^{μ}_{TTR} (right); for a description see caption of Fig. 2.1.

with

$$
\begin{aligned}
R^{\alpha}_{\mathrm{RTT}} &= -\operatorname{Tr}\left\{\boldsymbol{q_H}(t_1+t_2)\left[\boldsymbol{q_H}(t_1),\left[\boldsymbol{q_H}^2(0),\rho_{\mathrm{eq}}\right]\right]\right\}\\
R^{\alpha}_{\mathrm{TRT}} &= -\operatorname{Tr}\left\{\boldsymbol{q_H}(t_1+t_2)\left[\boldsymbol{q_H}^2(t_1),\left[\boldsymbol{q_H}(0),\rho_{\mathrm{eq}}\right]\right]\right\}\\
R^{\alpha}_{\mathrm{TTR}} &= -\operatorname{Tr}\left\{\boldsymbol{q_H}^2(t_1+t_2)\left[\boldsymbol{q_H}(t_1),\left[\boldsymbol{q_H}(0),\rho_{\mathrm{eq}}\right]\right]\right\}\\
R^{\mu}_{\mathrm{RTT}} &= -\operatorname{Tr}\left\{\boldsymbol{q_H}(t_1+t_2)\left[\boldsymbol{q_H}^2(t_1),\left[\boldsymbol{q_H}(0),\rho_{\mathrm{eq}}\right]\right]\right\}\\
&\quad -\operatorname{Tr}\left\{\boldsymbol{q_H}^2(t_1+t_2)\left[\boldsymbol{q_H}(t_1),\left[\boldsymbol{q_H}(0),\rho_{\mathrm{eq}}\right]\right]\right\}\\
R^{\mu}_{\mathrm{TRT}} &= -\operatorname{Tr}\left\{\boldsymbol{q_H}(t_1+t_2)\left[\boldsymbol{q_H}(t_1),\left[\boldsymbol{q_H}^2(0),\rho_{\mathrm{eq}}\right]\right]\right\}\\
&\quad -\operatorname{Tr}\left\{\boldsymbol{q_H}^2(t_1+t_2)\left[\boldsymbol{q_H}(t_1),\left[\boldsymbol{q_H}(0),\rho_{\mathrm{eq}}\right]\right]\right\}\\
R^{\mu}_{\mathrm{TTR}} &= -\operatorname{Tr}\left\{\boldsymbol{q_H}(t_1+t_2)\left[\boldsymbol{q_H}(t_1),\left[\boldsymbol{q_H}^2(0),\rho_{\mathrm{eq}}\right]\right]\right\}\\
&\quad -\operatorname{Tr}\left\{\boldsymbol{q_H}(t_1+t_2)\left[\boldsymbol{q_H}^2(t_1),\left[\boldsymbol{q_H}(0),\rho_{\mathrm{eq}}\right]\right]\right\}\\
R^{\mathrm{M}}_{\mathrm{RTT}} &= -\operatorname{Tr}\left\{\boldsymbol{q_M}(t_1+t_2)\left[\boldsymbol{q_H}(t_1),\left[\boldsymbol{q_H}(0),\rho_{\mathrm{eq}}\right]\right]\right\}\\
&\quad -\operatorname{Tr}\left\{\boldsymbol{q_H}(t_1+t_2)\left[\boldsymbol{q_M}(t_1),\left[\boldsymbol{q_H}(0),\rho_{\mathrm{eq}}\right]\right]\right\}\\
&\quad -\operatorname{Tr}\left\{\boldsymbol{q_H}(t_1+t_2)\left[\boldsymbol{q_H}(t_1),\left[\boldsymbol{q_M}(0),\rho_{\mathrm{eq}}\right]\right]\right\}\\
&= R^{\mathrm{M}}_{\mathrm{TRT}} = R^{\mathrm{M}}_{\mathrm{TTR}}, \qquad (2.11)
\end{aligned}
$$

which allows us to discuss the contributions from electrical (σ_α,σ_μ) and mechanical anharmonicity (σ_{M}) separately. To this end, we expand the nested commutators in Eqs. 2.11 and represent all terms in the form of Feynman diagrams (Figs. 2.1, 2.2 and 2.3). The corresponding 2D peaks are also summarized in Tab. 2.1 together with their intensities, which originate from products of the prefactors of the corresponding δ-terms in Eqs. 2.3, 2.6 and 2.8, and their sums when contributions overlap in frequency space. The frequency positions of the in total four peaks, $(-\omega,\omega)$, (ω,ω), $(\omega,0)$, and $(\omega,2\omega)$, are the same as in Ref. 74, but their intensities differ since the selection rules of the three pulse sequences of 2D-Raman-THz spectroscopy differ from those in 2D-Raman spectroscopy. The various spectra are discussed in the following.

In $R^{\alpha}_{\mathrm{RTT}}$, $R^{\alpha}_{\mathrm{TRT}}$, and $R^{\alpha}_{\mathrm{TTR}}$ (Fig. 2.1), the nonlinearity of $\boldsymbol{\alpha}$ allows the Raman interaction to induce a zero- or a two-quantum transition via the contribution of $\boldsymbol{q_H}^2$. Starting with $R^{\alpha}_{\mathrm{RTT}}$, four Feynman diagrams can be constructed (Fig. 2.1, top left). In this case the first Raman interaction induces a forbidden transition, i.e. a zero-quantum or a two-quantum transition. The pathways contributing to peak (e) start with a zero-quantum transition from either the left and the right, which however lead to two equivalent contributions of opposite sign that perfectly cancel out. Peak (f), on the other hand, starts with a two-quantum transition from the left. From there, the system goes into a $|1\rangle\langle 0|$ coherence by the second interaction from the left, or into $|2\rangle\langle 1|$ coherence via an interaction from the right. For a harmonic potential, the energy levels are equally spaced and both coherences oscillate with the same frequency. If we furthermore assume that the 0-1 and the 1-2 dephasing times are the same (see Eq. 2.14 below),[74] both contributions again cancel, and we have $R^{\alpha}_{\mathrm{RTT}} = 0$ altogether.

In contrast, two peaks appear in the TRT pulse sequence. For peak (a), the first interaction brings the system into a $|0\rangle\langle 1|$ coherence, and the second Raman interaction does a two-quantum transition to bring the system into the $|2\rangle\langle 1|$ coherence, hence the peak appears at $(-\omega,\omega)$. Peak (b), in contrast, is diagonal at (ω,ω), since the second interaction does a zero-quantum transition, which does not affect the state. The zero-quantum transition can either act from the left or the right side, giving rise to two contributions with opposite sign. However, these contributions do not fully cancel, since the interaction from left is weighted by the $(\boldsymbol{q_H}^2)_{1,1} = -3/2$ element, and the interaction from

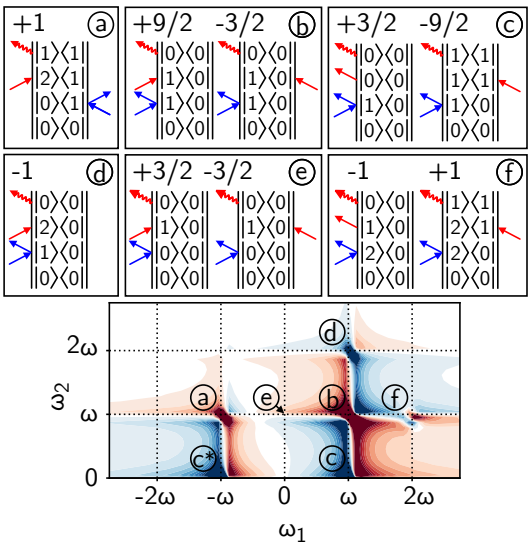

Figure 2.3: Feynman diagrams and 2D frequency-domain spectrum of $R^{M}_{\mathrm{RTT}} = R^{M}_{\mathrm{TRT}} = R^{M}_{\mathrm{TTR}}$; for a description see caption of Fig. 2.1.

Table 2.1: Intensities of all non-zero peaks appearing in Eq. (2.11).

	Peak			
	(a)	(b)	(c)	(d)
Response	$(-\omega,\omega)$	(ω,ω)	$(\omega,0)$	$(\omega,2\omega)$
$R^{\alpha}_{\mathrm{RTT}}$	0	0	0	0
$R^{\alpha}_{\mathrm{TRT}}$	1	-1	0	0
$R^{\alpha}_{\mathrm{TTR}}$	0	0	1	-1
R^{μ}_{RTT}	1	-1	1	-1
R^{μ}_{TRT}	0	0	1	-1
R^{μ}_{TTR}	1	-1	0	0
R^{M}_{RTT}	1	3	-3	-1
R^{M}_{TRT}	1	3	-3	-1
R^{M}_{TTR}	1	3	-3	-1

right by $(\boldsymbol{q_H}^2)_{0,0} = +1/2$. Finally, the TTR sequence has its forbidden transition in the emission step with zero-quantum coherences for peak (c), and two-quantum coherences for peak (d). Peak (c), with $\omega_2 = 0$, appears together with its conjugate complex (c*). The conjugate complex of all other peaks show up at negative frequencies ω_2, but the negative ω_2-half-space is not shown in Fig. 2.1 for clarity.

There are more peaks in R^{μ}_{RTT}, R^{μ}_{TRT}, and R^{μ}_{TTR} (Fig. 2.2), since there are two interactions with $\boldsymbol{\mu}$ and the forbidden transition can occur with either one of it. However, Eq. 2.11 shows that each term of R^{μ} can be written as a sum of two terms that we already discussed in the context of R^{α}, e.g. $R^{\mu}_{\mathrm{RTT}} = R^{\alpha}_{\mathrm{TRT}} + R^{\alpha}_{\mathrm{TTR}}$. The corresponding 2D spectra in Fig. 2.2 therefore are overlays of two spectra each from Fig. 2.1.

Finally, the responses $R^{\mathrm{M}}_{\mathrm{RTT}}$, $R^{\mathrm{M}}_{\mathrm{TRT}}$ and $R^{\mathrm{M}}_{\mathrm{TTR}}$ originating from mechanical anharmonicity are shown in Fig. 2.3. The term $\sigma_{\mathrm{M}}\boldsymbol{q_M}$ contributes to $\boldsymbol{\mu}$ and $\boldsymbol{\alpha}$ equally, and the forbidden transition can occur at any of the tree interactions. Since $\boldsymbol{\mu} = \boldsymbol{\alpha}$ for this case, the order of interactions does not matter, and $R^{\mathrm{M}}_{\mathrm{RTT}} = R^{\mathrm{M}}_{\mathrm{TRT}} = R^{\mathrm{M}}_{\mathrm{TTR}}$. The corresponding 2D spectrum is in essence an overlay of all three spectra shown in Fig. 2.1, except for the fact that the features that include zero-quantum transitions (b,c) change signs and amplitudes due to the different diagonal element of $\boldsymbol{q_M}$. Furthermore, peak (f) is now nonzero due to the anharmonic shift of the energy levels.

As in Ref. 74, we considered so far only Feynman diagrams starting from the $|0\rangle\langle 0|$ element of the density matrix in Figs. 2.1, 2.2 and 2.3, implicitly assuming a temperature T=0 K. It can however be shown that the overall response function does not depend on the starting level, despite the fact that more Feynman diagrams come into play, and hence is in fact temperature independent (see Appendix 2.7 for details). For that we however need to assume that the lineshape functions depend on level differences only (see Eq. 2.14 below), and that the effect of mechanical anharmonicity is on the transitions probabilities only (via $\boldsymbol{q_M}$), while we keep the energy spectrum equidistant. Fig. 2.3 shows that this is a good approximation. That is, the anharmonic shift $\omega_{21} - \omega_{10}$ is small, and for any reasonable, not too narrow spectral linewidth both contributions giving rise to peak (f) largely cancel each other. In comparison, the effect of mechanical anharmonicity on the transition probabilities, giving rise to peaks (a)-(e), is much larger. Within that approximation, quantum and classical response functions are in fact identical, and simple analytic expressions can be derived for the three response functions by collecting all terms (without that approximation, an explicit sum over Boltzmann-weighted initial states would be needed that converges extremely slowly for $\hbar\omega \ll k_B T$):

$$
\begin{aligned}
R_{\mathrm{RTT}}(t_1,t_2) \propto \Theta(t_1,t_2)\big(&(\sigma_\mu+\sigma_{\mathrm{M}})\cos(\omega t_1-\omega t_2)\Gamma_{-\omega,\omega}(t_1,t_2)+(-\sigma_\mu+3\sigma_{\mathrm{M}})\cos(\omega t_1+\omega t_2)\Gamma_{\omega,\omega}(t_1,t_2)\\
&+(\sigma_\mu-3\sigma_{\mathrm{M}})\cos(\omega t_1)\Gamma_{\omega,0}(t_1,t_2)+(-\sigma_\mu-\sigma_{\mathrm{M}})\cos(\omega t_1+2\omega t_2)\Gamma_{\omega,2\omega}(t_1,t_2)\big)\\
R_{\mathrm{TRT}}(t_1,t_2) \propto \Theta(t_1,t_2)\big(&(\sigma_\alpha+\sigma_{\mathrm{M}})\cos(\omega t_1-\omega t_2)\Gamma_{-\omega,\omega}(t_1,t_2)+(-\sigma_\alpha+3\sigma_{\mathrm{M}})\cos(\omega t_1+\omega t_2)\Gamma_{\omega,\omega}(t_1,t_2)\\
&+(\sigma_\mu-3\sigma_{\mathrm{M}})\cos(\omega t_1)\Gamma_{\omega,0}(t_1,t_2)+(-\sigma_\mu-\sigma_{\mathrm{M}})\cos(\omega t_1+2\omega t_2)\Gamma_{\omega,2\omega}(t_1,t_2)\big)\\
R_{\mathrm{TTR}}(t_1,t_2) \propto \Theta(t_1,t_2)\big(&(\sigma_\mu+\sigma_{\mathrm{M}})\cos(\omega t_1-\omega t_2)\Gamma_{-\omega,\omega}(t_1,t_2)+(-\sigma_\mu+3\sigma_{\mathrm{M}})\cos(\omega t_1+\omega t_2)\Gamma_{\omega,\omega}(t_1,t_2)\\
&+(\sigma_\alpha-3\sigma_{\mathrm{M}})\cos(\omega t_1)\Gamma_{\omega,0}(t_1,t_2)+(-\sigma_\alpha-\sigma_{\mathrm{M}})\cos(\omega t_1+2\omega t_2)\Gamma_{\omega,2\omega}(t_1,t_2)\big)
\end{aligned}
\tag{2.12}
$$

where $\Theta(t_1,t_2)$ is the Heaviside function ensuring that the response vanishes for $t_1 < 0$ or $t_2 < 0$. In second order perturbation theory, the complex conjugate of a term can be generated by two permutations in the commutator. Therefore, the two complex conjugate components have the same sign and reveal cos-functions upon addition.

We augment these response functions with dephasing terms $\Gamma(t_1,t_2)$ in essence along the lines of Ref. 69, but replacing the part originating from vibrational T_1 relaxation with Eq. 36, rather than Eq. 37, from Ref. 74. That is, each response function in Eq. 2.12 contains one term each for peaks at $(-\omega,\omega)$, (ω,ω), $(\omega,0)$ and $(\omega,2\omega)$, respectively, which are multiplied with the following damping functions:

$$
\begin{aligned}
\Gamma_{-\omega,\omega}(t_1,t_2) &= e^{-\frac{t_1+t_2}{2T_1}} e^{-2g(t_1)-2g(t_2)+g(t_1+t_2)}\\
\Gamma_{\omega,\omega}(t_1,t_2) &= e^{-\frac{t_1+t_2}{2T_1}} e^{-g(t_1+t_2)}\\
\Gamma_{\omega,0}(t_1,t_2) &= e^{-\frac{t_1+2t_2}{2T_1}} e^{-g(t_1)}\\
\Gamma_{\omega,2\omega}(t_1,t_2) &= e^{-\frac{t_1+2t_2}{2T_1}} e^{+g(t_1)-2g(t_2)-2g(t_1+t_2)}
\end{aligned}
\tag{2.13}
$$

As discussed in Ref. 74, the damping terms caused by vibrational relaxation depend on quan-

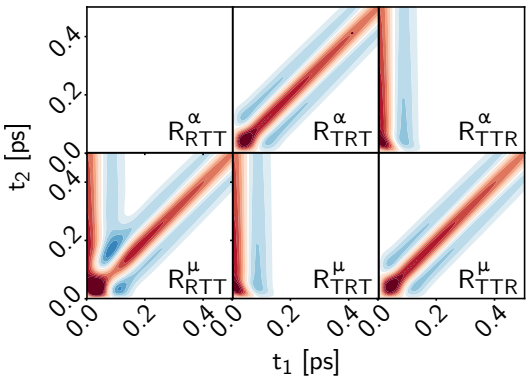

Figure 2.4: Time-domain signals R_{RTT}, R_{TRT}, and R_{TTR} for an inhomogeneously broadened system, using the parameters from Tab. 2.2 for the hydrogen-bond stretching vibration, but setting τ_c =100 ps and T_1 = 1 ps. The effects of nonlinear polarizability is shown in the top row, and that of nonlinear dipole moment in the bottom row.

tum numbers according to:

$$T_1^{(n,n)} = T_1$$
$$T_2^{(n,m)} = \frac{2T_1}{|n-m|}. \tag{2.14}$$

The lineshape function $g(t)$ is:

$$g(t) = \Delta\omega^2\tau_c^2\left(e^{-t/\tau_c} + t/\tau_c - 1\right), \tag{2.15}$$

whose origin are Gaussian fluctuations of the transition frequency $\omega(t)$ with standard deviation $\Delta\omega$ and correlation time τ_c:

$$\langle\delta\omega(t)\delta\omega(0)\rangle = \Delta\omega^2 e^{-t/\tau_c}, \tag{2.16}$$

where $\delta\omega(t) = \omega(t) - \langle\omega(t)\rangle$. In the limes $\Delta\omega\tau_c \ll 1$, Eq. 2.15 causes pure dephasing with $T_2^* = (\Delta\omega^2\tau_c)^{-1}$, in the limes $\Delta\omega\tau_c \gg 1$ inhomogeneous dephasing with a Gaussian lineshape with width $\Delta\omega$.

2.3.5 Inhomogeneous Broadening and Echoes

In any of the responses, peak (a) with frequencies of opposite signs $(-\omega, \omega)$ is a rephasing pathway,[41] as a coherence that dephased during the first time period might rephase during the second, provided the band is inhomogeneously broadened and maintains some amount of memory on the oscillation frequency. Rephasing requires an "inversion of coherence", and the only possibility to achieve that are coherence pathways that start with a $|0\rangle\langle 1|$ coherence and are then brought into a $|2\rangle\langle 1|$ coherence by the second pulse (see Figs. 2.1, 2.2 and 2.3). In a time-domain representation, rephasing will generate an echo along $t_1 = t_2$; in a frequency-domain representation tilted 2D lineshapes. Peak (b), in contrast, is a non-rephasing pathway.

To explore the appearance of echoes (Fig. 2.4), we choose lineshape parameters for the hydrogen-bond stretching vibration as listed in Tab. 2.2 (see below), except of unrealistically long values for τ_c =100 ps and T_1 = 1 ps. Echoes along $t_1 = t_2$ are seen for R^{α}_{TRT}, R^{μ}_{RTT}, and R^{μ}_{TTR}, i.e., coherence pathways with their two-quantum transition for the second pulse to induce the required two-quantum transition. Experimentally, one can distinguish between R_{RTT}, R_{TRT}, and R_{TTR} by the choice of a pulse sequence, hence when observing an echo, one gets an handle on determining the major source of anharmonicity. The vertical features in R^{α}_{TTR}, R^{μ}_{RTT} and R^{μ}_{TRT} originate from peak (c), which does not experience any inhomogeneous dephasing in the t_2 direction, since its frequency in ω_2 is always zero.

2.4 Comparison to Water Experiments

2.4.1 Instrument Response Function

We now explore to what extent the model derived here can explain the experimental data of liquid water from Ref. 98. We start with noting that this experiment measured the R_{RTT} and R_{TRT} responses by interchanging the timing between the Raman and THz-pump pulses, but not the R_{TTR} response, which would require a different detection scheme.[81,82] With the particular arrangement of the delay lines in the experiment of Ref. 98, we measured:

$$R(t_1, t_2) = R_{\mathrm{RTT}}(t_1, t_2) + R_{\mathrm{TRT}}(-t_1, t_2 - t_1), \tag{2.17}$$

where time t_1 is from the Raman pump pulse to the THz pump pulse and time t_2 from the THz pump pulse to detection (which is why $t_2 - t_1$ appears as argument of R_{TRT} where the THz pump comes before the Raman pump, while t_2 is the time from the second Raman interaction to detection in the definition of R_{TRT} in Eq. 2.12). Furthermore, the experimental signal is obtained from the response functions by a convolution with the instrument response function (IRF):

$$S(t_1, t_2) = I(t_1, t_2) \circledast R(t_1, t_2), \tag{2.18}$$

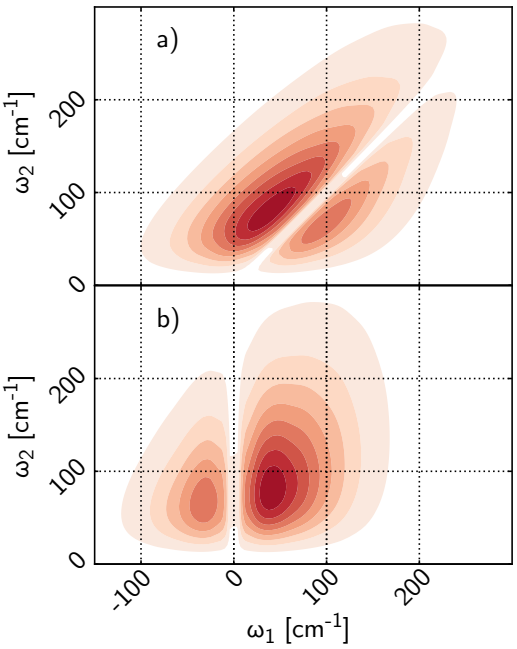

Figure 2.5: The absolute value of the IRF in the frequency domain for (a) the RTT pulse sequence and (b) the TRT pulse sequence, which have been derived from Eq. 2.19 with the experimentally determined pulses and transfer function.[98]

which is calculated from the THz field E_{THz} and the envelope of the Raman pulse I_{Raman}:

$$I(t_1,t_2) \propto \frac{d}{dt_2} E_{\mathrm{THz}}(t_2) I_{\mathrm{Raman}}(t_2+t_1). \quad (2.19)$$

Eq. 2.19 is an idealized expression to illustrate the basic idea; in the real experiment the IRF contains in addition a transfer function describing how the emitted THz field reshapes as it propagates from the sample to the detection crystal, as well as a correction for a non-perfect Gouy phase (see Refs.[77,98] for details).

It is illustrative to look at the IRF in the frequency domain (Fig. 2.5), as it shows which one of the peaks in the 2D responses (Figs. 2.1, 2.2 and 2.3) the experiment is sensitive to. The IRF spectrum for the RTT pulse sequence (Fig. 2.5a) has two nodal lines, one at $\omega_2 = 0$, which is caused by the derivative d/dt_2 in Eq. 2.19, and one at $\omega_1 = \omega_2$, which caused by the fact that the THz pump pulse does not have any DC component (i.e., $\int E_{\mathrm{THz}}(t)dt = 0$). Peaks (b) and (c) lie on these nodal lines, as they would contain zero-quantum transitions for either the THz pump pulse or the THz emission process. We will nevertheless see these peaks to a certain extent since the damping in water is very fast, hence they have a significant spectral width that extends into regions where the IRF is non-zero. Furthermore, a smaller

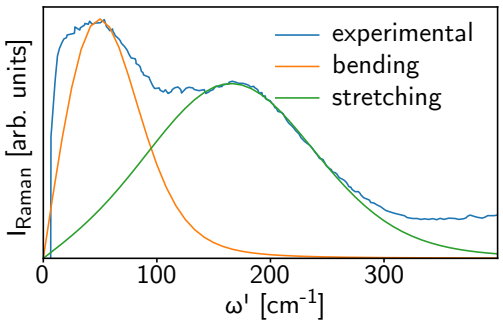

Figure 2.6: The experimental anisotropic Raman spectrum of water (blue) together with two lineshape functions used to fit the two hydrogen-bond modes with the parameters listed in Tab. 2.2. The experimental data have been taken from Ref. 50

bandwidth is observed in the rephasing quadrant ($\omega_1 < 0$, $\omega_2 > 0$) than in the non-rephasing quadrant ($\omega_1, \omega_2 > 0$), reflecting the fact that the peak at $\omega_2 = -\omega_1$ includes a two-quantum transition which requires a higher bandwidth of the THz pulse.

For the R_{TRT} response, the IRF has to be transformed to account for the time shift applied in Eq. 2.17 (Fig. 2.5b). The effect of a time transform $t_1 = -t_1'$ and $t_2 = t_2' - t_1'$ on the frequency domain can be derived by inspecting the effect on a single basis function of the Fourier transformation:

$$\begin{aligned} \exp\left(i\left[\omega_1 t_1 + \omega_2 t_2\right]\right) &= \exp\left(i\left[\omega_1(-t_1') + \omega_2(t_2' - t_1')\right]\right) \\ &= \exp\left(i\left[\omega_1' t_1' + \omega_2' t_2'\right]\right) \quad (2.20) \end{aligned}$$

with $\omega_1' = -\omega_1 - \omega_2$ and $\omega_2' = \omega_2$. The transformed instrument response has nodal lines at $\omega_1 = 0$ and $\omega_2 = 0$. Hence, in this case, the diagonal peak (b) lies in a region where the IRF is large, since the envelope of the Raman pulse has a zero-frequency component.

2.4.2 1D Spectra and 2D Response

Fig. 2.6 shows the 1D Raman spectrum of water in the relevant frequency range, which contains two spectroscopic features: the hydrogen-bond bending vibration around 50 cm^{-1} and the hydrogen-bond stretch vibration around 170 cm^{-1} (the librational mode around 600 cm^{-1} is not considered here since it is completely ouside our experimental observation window). Also shown in Fig. 2.6 are fits to these two bands, assuming a linear response function

$$R_{\mathrm{R}}(\omega') = \Im \int_0^\infty \sin(\omega t) e^{-\frac{t}{2T_1}} e^{-g(t)} e^{-i\omega' t} dt \quad (2.21)$$

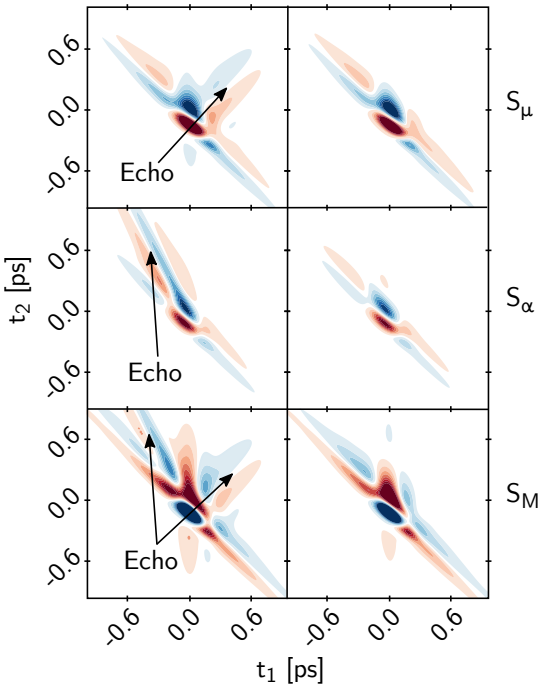

Figure 2.7: Time domain signals of the responses S^μ (top), S^α (middle), and S^{M} (bottom) after convolution of Eq. 2.17 with the IRF Eq. 2.18 and 2.19. The right column uses the parameters as in Tab. 2.2, the left column sets τ_c =100 ps and $T_1 = 1$ ps to more clearly demonstrate the echoes. Discernible echoes are marked by arrows.

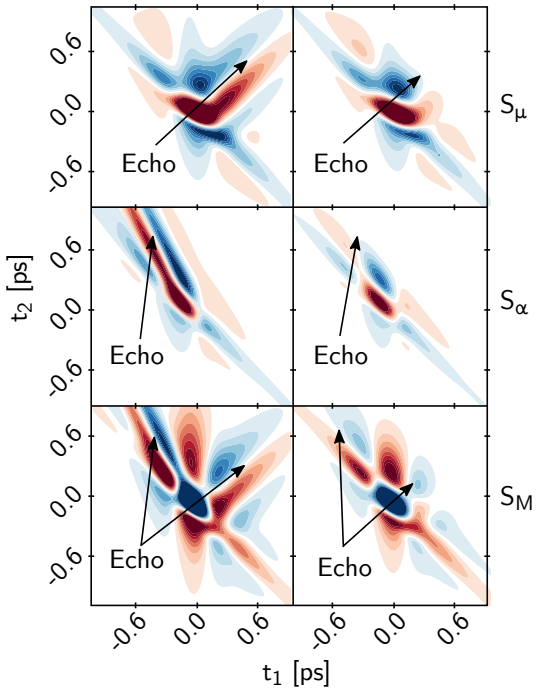

Figure 2.8: Time domain signals of the responses S^μ (top), S^α (middle), and S^{M} (bottom) after convolution of Eq. 2.17 with the IRF Eqs. 2.18 and 2.19. The right column uses the parameters as in Tab. 2.2, the left column sets τ_c =100 ps and $T_1 = 1$ ps to more clearly demonstrate the echoes. Discernible echoes are marked by arrows.

The parameters are listed in Tab. 2.2 and will be justified later based on the fit of the echo observed in the 2D response.

Starting with the hydrogen-bond stretching vibration, Fig. 2.7 (left column) shows the corresponding 2D results in the time domain, i.e., the convolution of Eq. 2.17 with the IRF. The lineshape parameters of Tab. 2.2 were assumed, except for τ_c =100 ps and $T_1 = 1$ ps, which in a first step was chosen unrealistically slow in order to more clearly demonstrate the resulting echoes (i.e., the same parameters as in Fig. 2.4). Each one of the three types of anharmonicities give rise to a different 2D response. The echoes shown in Fig. 2.4 survive the convolution and are marked by arrows in Fig. 2.7. In the case of a nonlinear dipole moment, the rephasing peak is in R^{μ}_{RTT} and the echo is visible in the (upper right) RTT quadrant along $t_1 = t_2$. On the other hand, for S_α with the nonlinearity in the polarizability, the rephasing peak is in the $R^{\alpha}_{\mathrm{TRT}}$ response and the echo appears in the upper left quadrant along the $t_2 = -2t_1$ due to the time transformation in Eq. 2.17. Finally, S_{M} is a mix of both (albeit with different signs), since mechanical anharmonicity allows for all coherence pathways at the same time. Fig. 2.7 (right column) shows the same, but now for τ_c = 370 fs and T_1=250 fs (which will be justified later based on a fit to the experimental data).The echoes are now masked by the instrument response function.

Modelling the hydrogen-bond bending vibration around 50 cm^{-1} on the same footing reveals similar results, see Fig. 2.8. The echoes are clearer in this case, even when using realistic parameters for τ_c and T_1 (Fig. 2.8, right column). In addition the signal intensity is significantly larger (Fig. 2.7 has been upscaled by a factor 2), reflecting the the limited bandwidth of the THz pulses in the experiment, that peak at 50 cm^{-1} but only partially cover the 170 cm^{-1} band.[98]

2.4.3 Fit of the Water Response

The free parameters of the model are σ_μ, σ_α, σ_{M}, T_1, τ_c, ω and $\Delta\omega$. In an iterative process, we varied the dephasing parameter T_1, τ_c to reproduce the 2D-response, and ω as well as $\Delta\omega$ to reproduce the position and width of the hydrogen-bond bending vibration in the 1D spectrum (Fig. 2.6). In addition, small variations of the delay-time zeros and the correction for the Gouy phase were allowed,

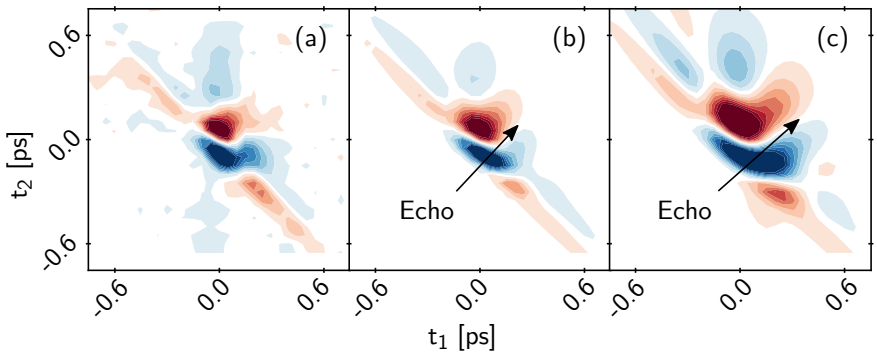

Figure 2.9: (a) Experimental water response at room temperature and signal calculated from the anharmonic oscillator model form (b) the hydrogen-bond stretching vibrations and (c) the hydrogen-bond bending vibrations with the parameters listed in Tab. 2.2. Discernible echoes are marked by arrows. The experimental data have been taken from Ref. 98.

which are not very accurately defined in the experiment.[98] Once these nonlinear parameters are fixed, the 2D responses of Figs. 2.7 and 2.8 (right column) can be considered a basis in which the experimental response is expanded in order to minimize the RMSD between experimental and fitted spectrum. Fig. 2.9 shows that this procedure results in a remarkably good agreement with the experimental data, despite the simplicity of the model and the small number of parameters. Tab. 2.2 summarizes the resulting parameters for the two modes.

The RMSD of the fit for the hydrogen-bond stretching vibration is smaller by a significant factor 0.7 as compared to that of the hydrogen-bond bending vibration. It has in fact not been possible to find a minimum in the RMSD for the hydrogen-bond bending vibration (see footnote in Tab. 2.2), and in addition, the shift in t_2 required to obtain the best fit for hydrogen-bond bend vibration is larger (i.e., Δt_2=170 fs) than what we would think is its experimental uncertainty (the corresponding value for the hydrogen-bond stretching vibration is Δt_2 = 35 fs). We therefore suggest that the observed experimental signal originates predominantly from the hydrogen-bond stretching vibration, despite the fact its response is reduced to a certain extent as it is at the very edge of the experimentally accessible frequency window. We have not considered scenarios in which both bands contribute in parallel, or even more so, couple with each other, because the number of fitting parameters would be too large and the fitting problem would be under-determined.

Table 2.2: Parameters obtained from the fit of the hydrogen-bond bending vibration and hydrogen-bond stretching vibration.

	stretching	bending
ω [cm^{-1}]	165[1]	45[1]
$\Delta\omega$ [cm^{-1}]	75	40
τ_c [fs]	370	300[2]
T_1 [fs]	250	300[2]
$\sigma_\mu/\sigma_\mathrm{M}$	1.4	0.96
$\sigma_\alpha/\sigma_\mathrm{M}$	-0.1	0.01

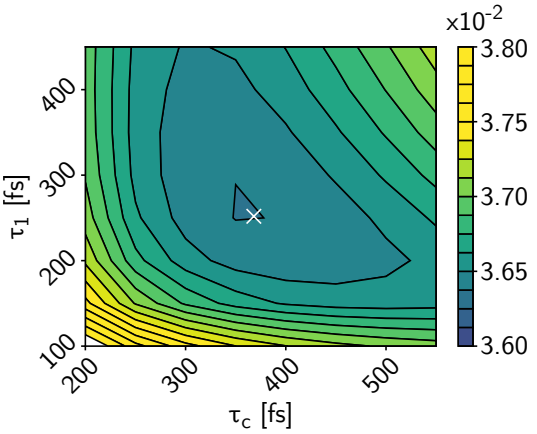

Figure 2.10: RMSD between experimental and simulated spectrum as a function of τ_c and T_1, considering the hydrogen-bond stretching vibration. The parameters for ω and $\Delta\omega$ were kept fixed to the values reported in Tab. 2.2, since they are determined mostly by the 1D spectrum (Fig. 2.6), which in turn changes only very little when varying τ_c and T_1. The linear parameters σ_μ, σ_α, σ_M, on the other hand, were optimized for each (τ_c,T_1)-point in this plot.

Fig. 2.10 plots the RMSD of the fit for the hydrogen-bond stretching vibration as a function of τ_c and T_1, revealing that both parameters are not strongly correlated. As these two parameters determine the relative contribution of inhomogeneous vs homogeneous dephasing, we conclude that the signatures of the echo are still present in the 2D response. In that regard it is fortunate that the rephasing peak (a) in R^{μ}_{RTT} (Fig. 2.2, bot-

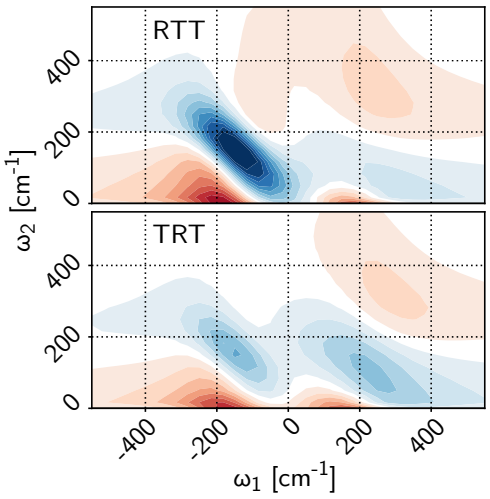

Figure 2.11: Same model as in Fig. 2.9b, but before convolution with the instrument response function and in the frequency domain, plotting R_{RTT} (top) and R_{TRT} (bottom) separately.

tom left) and $R^{\mathrm{M}}_{\mathrm{RTT}}$ (Fig. 2.3, bottom) have the same sign, while all other peaks have opposite sign (and the contribution of R^{μ}_{RTT} is negligible, see Tab. 2.2). Together with the corresponding weights of the two contributions ($\sigma_\mu/\sigma_{\mathrm{M}}$=1.4), the rephasing peak will actually dominate in the overall response. That is illustrated in Fig. 2.11, which shows the response in the the frequency domain and without the convolution with the instrument response function for the same parameters as in in Fig. 2.9b; R_{RTT} is dominated by one rephasing peak that is strongly elongated along the diagonal due to the inhomogeneous broadening. As a result, an echo is discernible in in the time-domain data of Fig. 2.9b, despite the fact that is essentially completely masked in the individual contributions of Fig. 2.7 (right column).

During the fit, the absolute intensity of the experimental signal was not considered. Likewise, the proportionality constants in Eq. 2.4, $d\mu/dq$ and $d\alpha/dq$, are not known. Therefore, the three parameters σ_μ, σ_α, and σ_{M} are only known modulo an overall scaling factor, and only their relative contributions to the signal (e.g.., $\sigma_\mu/\sigma_{\mathrm{M}}$ and $\sigma_\alpha/\sigma_{\mathrm{M}}$) can be extracted. The sign of the overall signal can however be determined. The sign of the overall signal is given by the signs of σ_{M} times that of $d\alpha/dq$ (since $d\mu/dq$ enters quadratically in Eq. 2.10). To reproduce the experimentally observed sign, we either have σ_{M} negative and $d\alpha/dq$ positive (which is what we assumed here), or *vice versa*.

2.5 Discussion and Conclusion

We have shown that the experimental 2D-Raman-THz response of liquid water can be explained almost quantitatively by describing the hydrogen bond bending modes with the help of a very simple anharmonic oscillator model. The model contains only six independent parameters, i.e., $\sigma_\mu/\sigma_{\mathrm{M}}$ and $\sigma_\alpha/\sigma_{\mathrm{M}}$ as well as ω_0, $\Delta\omega$, τ_c, and T_1. Despite the fact that the instrument response function masks the information content of the molecular 2D response to a significant extent, it is still sufficient to determine these parameters with confidence (Fig. 2.10), if we assume the response originates from predominantly one of the two bands in the observation window of the experiment. We tentatively conclude that this dominating band is the hydrogen-bond stretching vibration at 170 cm^{-1}, but we cannot exclude additional contributions from the hydrogen-bond bending vibration around 50 cm^{-1}, or from couplings between both bands. The librational mode around 600 cm^{-1}, on the other hand, is completely outside our experimental observation window (Fig. 2.5).

The physical interpretation of σ_μ, σ_α, and σ_{M} is not straight forward, since the low frequency modes of water are collective in nature and presumably delocalized to a certain extent. It is nonetheless worth noting that the biggest contribution to the signal originates from mechanical anharmonicity σ_{M} and the dipole nonlinearity σ_μ, while the contribution from the nonlinearity in the polarizability is negligible with $\sigma_\alpha = 0.1\sigma_{\mathrm{M}}$ (Tab. 2.2). This observation is in stark contrast to results from recent MD work, which revealed an echo for the TRT pulse sequence.[88,91,102] That echo originated from the hindered rotation band around 600 cm^{-1}, which we however do not observe in the experiment due to the limited bandwidth. A large nonlinearity in the polarizability for that mode can be understood from the fact that a strict $\Delta J = 2$ selection rule would apply for a Raman interaction, together with a $\Delta J = 1$ selection rule for a THz interaction, in the limiting case of a free rather than hindered rotor.[41] This explanation obviously does not apply for the hydrogen-bond bending and stretching vibrations.

Regarding the line shape function, on the other hand, the parameters for τ_c, $\Delta\omega$ and T_1 quantify the degree of inhomogeneous broadening of the hydrogen-bond-bending vibration (Tab. 2.2). That is, with $\Delta\omega\tau_c \approx 5$, the lineshape function is in the "slow-modulation", or "quasi-inhomogeneous" limit.[29] At the same time, vibrational relaxation

with T_1 =250 fs contributes only 20 cm^{-1} to the total linewidth. The correlation time τ_c =370 fs, in turn, is a measure of the lifetime of the hydrogen-bond networks giving rise to the hydrogen-bond stretching vibration. The typical lifetime of a single hydrogen bond is 1 ps,,[34,35,107,108] hence we conclude that those modes are delocalized over ≈ 3 hydrogen bonds.

The quality of the fit of Fig. 2.9 is much better than that of much more sophisticated calculations based on a water force field in connection with MD simulations.[89] The problem with the MD approach arises from the fact that a water force field needs to describe the thermodynamics and dynamics of water reasonably well in the first place, while the anharmonicities, that are the bottleneck of the 2D-Raman-THz signal, result from these constraints only in an indirect way. Anharmonicities are typically not fitted explicitly, except if very specific effects, such as nuclear quantum effects,[109] are to be described. Furthermore, in particular when polarizability is included in a water force field, the number of parameters is typically very large, and the problem is underdetermined. Electrical anharmonicity has a lot to do with the redistribution of charges during the motion of water molecules, and being able to quantify it might reveal guidelines to design better water models.[110] To that end, it would be important to infer the anharmonicity parameters σ_μ, σ_α, and σ_{M} from a MD simulation of a realistic water force field.

In conclusion, we think that 2D-Raman-THz spectroscopy has the highest information content as to date with regard to the intermolecular degrees of freedom water, but learning how to extract that information from the experimental response is challenging. The present work constitutes a significant step in that direction.

Acknowledgments: We thank Yoshitaka Tanimura for very valuable discussions. The work has been supported by the Swiss National Science Foundation (SNF) through the NCCR MUST.

2.6 Appendix A: Position Operator in an Anharmonic Eigenstate Basis

In the cubic anharmonic oscillator model, the harmonic oscillator Hamiltonian $\hat{H}_0$ is perturbed by $\sigma_M \hbar\omega q^3$.

$$\hat{H} = \hat{H}_0 + \sigma_M \hbar\omega \hat{q}^3 \tag{2.22}$$

where $\hat{q} = \sqrt{m\omega/\hbar}\hat{x}$ is the unitless position operator, and σ_M the size of the perturbation. To first order in σ_M, the eigenfunctions of $\hat{H}$ are expressed as linear combination of the harmonic eigenfunctions $|\varphi_n\rangle$.[106]

$$\begin{aligned}|\varphi_n^{(anh)}\rangle = |\varphi_n\rangle + \sigma_M\big(&a_n|\varphi_{n+1}\rangle + b_n|\varphi_{n-1}\rangle \\ &+ c_n|\varphi_{n+3}\rangle + d_n|\varphi_{n-3}\rangle\big)\end{aligned} \tag{2.23}$$

with

$$\begin{aligned}a_n &= -3\left(\frac{n+1}{2}\right)^{3/2} \\ b_n &= 3\left(\frac{n}{2}\right)^{3/2} \\ c_n &= -\frac{1}{3}\left[\frac{(n+3)(n+2)(n+1)}{8}\right]^{1/2} \\ d_n &= \frac{1}{3}\left[\frac{n(n-1)(n-2)}{8}\right]^{1/2}.\end{aligned} \tag{2.24}$$

Mechanical anharmonicity does not affect the position operator $\hat{q}$ *per se*, but rather changes its matrix representation due to a change of the basis functions $\{|\varphi_i\rangle\} \rightarrow \{|\varphi_i^{(anh)}\rangle\}$. We will call $\hat{q}$ in a harmonic eigenfunction basis $\boldsymbol{q_H}$, and $\boldsymbol{q_A}$ if it is expressed in anharmonic eigenfunctions. Expressing $(\boldsymbol{q_A})_{i,j} \equiv \langle\varphi_i^{(anh)}|\hat{q}|\varphi_j^{(anh)}\rangle$ in terms of $(\boldsymbol{q_H})_{k,l} \equiv \langle\varphi_k|\hat{q}|\varphi_l\rangle$, using Eq. 2.23, we get a large collection of terms:

$$\begin{aligned}(\boldsymbol{q_A})_{i,j} = (\boldsymbol{q_H})_{i,j} + \sigma_M\big(&a_j(\boldsymbol{q_H})_{i,j+1} + a_i(\boldsymbol{q_H})_{i+1,j} \\ &+ b_j(\boldsymbol{q_H})_{i,j-1} + b_i(\boldsymbol{q_H})_{i-1,j} \\ &+ c_j(\boldsymbol{q_H})_{i,j+3} + c_i(\boldsymbol{q_H})_{i+3,j} \\ &+ d_j(\boldsymbol{q_H})_{i,j-3} + d_i(\boldsymbol{q_H})_{i-3,j}\big),\end{aligned} \tag{2.25}$$

where terms higher than first order in σ_M have been discarded. The matrix form of the position operator in harmonic oscillator eigenbasis is (see Eq. 2.3):

$$\boldsymbol{q_H} = \frac{1}{\sqrt{2}}\begin{pmatrix} 0 & \sqrt{1} & 0 & 0 & \\ \sqrt{1} & 0 & \sqrt{2} & 0 & \\ 0 & \sqrt{2} & 0 & \sqrt{3} & \\ 0 & 0 & \sqrt{3} & 0 & \ddots \\ & & & \ddots & \ddots \end{pmatrix}. \tag{2.26}$$

A matrix with $(\boldsymbol{q_H})_{i,j+1}$ is the matrix $\boldsymbol{q_H}$ shifted up by one row:

$$\frac{1}{\sqrt{2}}\begin{pmatrix} \sqrt{1} & 0 & \sqrt{2} & \\ 0 & \sqrt{2} & 0 & \ddots \\ 0 & 0 & \sqrt{3} & \ddots \\ & & & \ddots \end{pmatrix}. \tag{2.27}$$

Hence, the elements $\sqrt{j}\delta_{i+1,j}$ are transformed to $\sqrt{i+1}\delta_{i,j}$ terms in that shifted matrix, and

$\sqrt{i}\delta_{i-1,j}$ of $\boldsymbol{q_H}$ to $\sqrt{i}\delta_{i-2,j}$. Using this procedure, the shifted matrices in Eq. 2.25 become:

$$
\begin{aligned}
(\boldsymbol{q_H})_{i,j+1} &= \tfrac{1}{\sqrt{2}}\Big(\sqrt{i+1}\delta_{i,j} + \sqrt{i}\delta_{i-2,j}\Big)\\
(\boldsymbol{q_H})_{i+1,j} &= \tfrac{1}{\sqrt{2}}\Big(\sqrt{j+1}\delta_{i,j} + \sqrt{j}\delta_{i,j-2}\Big)\\
(\boldsymbol{q_H})_{i,j-1} &= \tfrac{1}{\sqrt{2}}\Big(\sqrt{i}\delta_{i,j} + \sqrt{i+1}\delta_{i,j-2}\Big)\\
(\boldsymbol{q_H})_{i-1,j} &= \tfrac{1}{\sqrt{2}}\Big(\sqrt{j}\delta_{i,j} + \sqrt{j+1}\delta_{i-2,j}\Big)\\
(\boldsymbol{q_H})_{i,j+3} &= \tfrac{1}{\sqrt{2}}\Big(\sqrt{i+1}\delta_{i-2,j} + \sqrt{i}\delta_{i-4,j}\Big)\\
(\boldsymbol{q_H})_{i+3,j} &= \tfrac{1}{\sqrt{2}}\Big(\sqrt{j+1}\delta_{i,j-2} + \sqrt{j}\delta_{i,j-4}\Big)\\
(\boldsymbol{q_H})_{i,j-3} &= \tfrac{1}{\sqrt{2}}\Big(\sqrt{i}\delta_{i,j-2} + \sqrt{i+1}\delta_{i,j-4}\Big)\\
(\boldsymbol{q_H})_{i-3,j} &= \tfrac{1}{\sqrt{2}}\Big(\sqrt{j}\delta_{i-2,j} + \sqrt{j+1}\delta_{i-4,j}\Big) \qquad (2.28)
\end{aligned}
$$

which include zero- ($\delta_{i,j}$), two- ($\delta_{i-2,j}$ and $\delta_{i,j-2}$), and four-quantum ($\delta_{i-4,j}$ and $\delta_{i,j-4}$) contributions. Collecting all terms, we obtain:

$$
\begin{aligned}
\tfrac{1}{\sqrt{2}}\Big(a_j\sqrt{i+1} + a_i\sqrt{j+1} + b_j\sqrt{i} + b_i\sqrt{j}\Big)\delta_{i,j} &= \\
-\tfrac{3}{2}\big(2i+1\big)\delta_{i,j} &\\
\tfrac{1}{\sqrt{2}}\Big(a_j\sqrt{i} + b_i\sqrt{j+1} + c_j\sqrt{i+1} + d_i\sqrt{j}\Big)\delta_{i-2,j} &= \\
\tfrac{1}{2}\sqrt{i}\sqrt{i-1}\delta_{i-2,j} &\\
\tfrac{1}{\sqrt{2}}\Big(a_i\sqrt{j} + b_j\sqrt{i+1} + c_i\sqrt{j+1} + d_j\sqrt{i}\Big)\delta_{i,j-2} &= \\
\tfrac{1}{2}\sqrt{j}\sqrt{j-1}\delta_{i,j-2} &\\
\tfrac{1}{\sqrt{2}}\Big(c_j\sqrt{i} + d_i\sqrt{j+1}\Big)\delta_{i-4,j} = 0 &
\end{aligned}
\qquad (2.29)
\qquad (2.30)
$$

We see that the $\delta_{i-4,j}$ elements cancel (likewise for $\delta_{i,j-4}$), and only zero- and two-quantum transitions remain in $\boldsymbol{q_A}$, in addition to the one quantum transitions from $\boldsymbol{q_H}$. Inserting Eq. 2.30 into Eq. 2.25 we get

$$\boldsymbol{q_A} = \boldsymbol{q_H} + \sigma_M \boldsymbol{q_M}, \qquad (2.31)$$

where the second term describes the correction to the position matrix due to anharmonicity with the final expression of $\boldsymbol{q_M}$ given in Eq. 2.8.

2.7 Appendix B: Temperature Independence of the Response Function

Temperature enters via the thermal population of the initial density matrix ρ_{eq}. In IR spectroscopy, one usually assumes that only the ground state is initially populated due to $\hbar\omega \gg k_B T$, but that assumption no longer holds in THz spectroscopy, and the contributions from many initial states have to be considered. Fig. 2.12 exemplifies that for R^{μ}_{RTT} by showing all contributing Feynman diagrams sorted according to their initial state. Since that response functions contain all four nonzero peaks (a), (b), (c), and (d), the result is universal and applies in the same way for the other response functions. It can be seen that the overall intensities do not depend on initial state and hence also not on temperature. However, a prerequisite for this to work is the assumption that the lineshape functions depend on energy level differences only (Eq. 2.14), and that the energy spacing between states is equidistant, i.e. that of a harmonic oscillator, and that the effect of mechanical anharmonicity only enters via the softened selection rules that allow for zero- and two-quantum transitions. Fig. 2.3 demonstrates that this is a good approximation (see discussion in the main text).

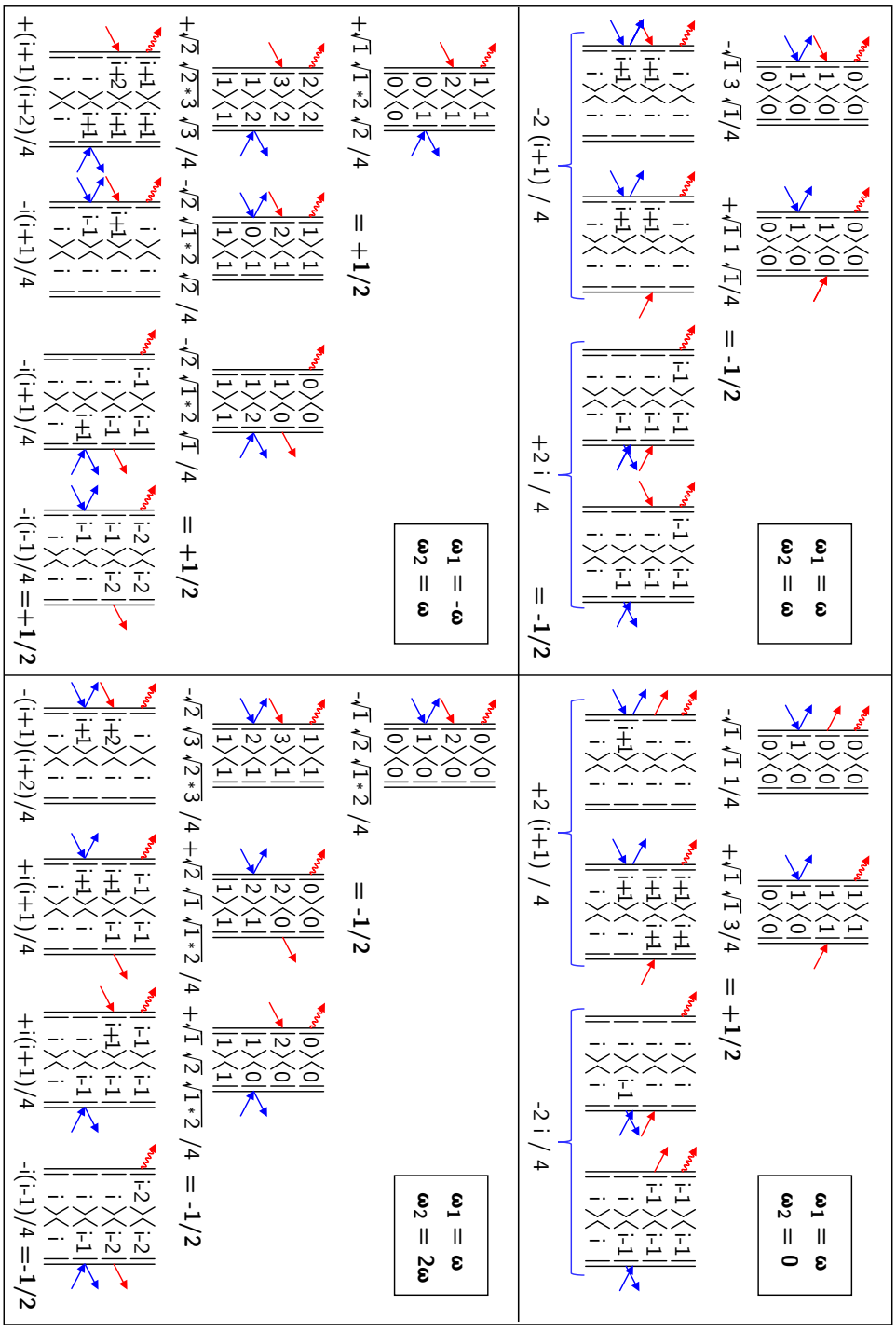

Figure 2.12: Collection of all Feynman diagrams responsible for the four peaks (ω,ω), $(\omega,0)$, $(-\omega,\omega)$, and $(\omega,2\omega)$ present in R^{μ}_{RTT}. The pathways are ordered by their initial state, and the intensity of each pathway is denoted below the corresponding Feynman diagrams.

Chapter 3

Feynman Pathways of 2D Oscillators

3.1 Introduction

Chemical bonds couple the motion of individual atoms. Therefore, the atoms do not move independently but rather in a correlated manner. For a harmonic system, however, a set of normal mode coordinates can be found, whose motion is independent from each other. In this way, the high-dimensional motion is reduced to a collection of independent one-dimensional harmonic oscillators, for which simple, analytical solutions exist. For this reason, the harmonic oscillator is the model of choice for the description of vibrational spectroscopy.

The responses which contribute to 2D-Raman-THz signals cannot be described by a perfectly harmonic system; anharmonicity is crucial for the description of these methods. In Chapter 2, the possible 2D-Raman-THz signals have been derived for 1D anharmonic oscillators. Each oscillator with frequency ω can give rise to four distinct signals: $\cos[\omega(t_1 + t_2)]$, $\cos[\omega(t_1 - t_2)]$, $\cos[\omega(t_1 + 2t_2)]$, and $\cos[\omega t_1]$. The weights of these signals are determined by the kind of anharmonicity (electrical *versus* mechanical anharmonicity). Peak patterns give direct insight into these anharmonicities. It has been demonstrated that the experimental 2D-Raman-THz response can be described to a large extent by a collection of 1D oscillators which represent hydrogen bond stretching modes (Figure 2.9).

As a strength of nonlinear spectroscopy, cross peaks can give insight into coupling between modes. Measurements of halogenated liquids (which have well-defined transitions in the THz range) have shown the importance of couplings to the 2D-Raman-THz signals.[80–83]

In this chapter, we will discuss the possible signal originating from anharmonic 2D oscillators; especially how the cross peaks are generated from electrical and mechanical couplings. The focus is hereby put on the positions and intensities of possible cross peaks appearing in 2D-Raman-THz spectra. Along the lines of Chapter 2, the effects of mechanical couplings will be treated in a perturbative manner. The resulting responses depend linearly on the different perturbations. In this way, the total system response can be expanded in terms of "basis responses", which allows for very simple interpretation of the different signal generation mechanisms.

In order that the model can be applied to physically relevant problems, spectral line shapes need to be addressed on an adequate level of theory.

3.2 Harmonic System

A two dimensional harmonic oscillator, which has oscillation frequency ω_A in q_A direction and ω_B in q_B direction is described by the Hamiltonian

$$\hat{H}^{(0)} = \frac{\hbar\omega_A}{2}\left(\hat{p}_A^2 + \hat{q}_A^2\right) + \frac{\hbar\omega_B}{2}\left(\hat{p}_B^2 + \hat{q}_B^2\right). \qquad (3.1)$$

For this Hamiltonian, the Schrödinger equation can be separated into pure $\hat{q}_A$ and $\hat{q}_B$ oscillator parts, which can be solved independently. For both 1D oscillators, this gives a set of states $|n\rangle = \varphi_n(q_{A,B})$ with corresponding energies $E_n := \hbar\omega_{A,B}(n + \frac{1}{2})$. The solution to the 2D oscillator is given by the product states

$$|m, n\rangle := \varphi_m(q_A)\varphi_n(q_B) \qquad (3.2)$$

where m is the quantum number describing the state of oscillator A, and n is the quantum number of oscillator B. The energy of the $|m, n\rangle$ state is the sum of two single-oscillator energies

$$E_{m,n} = \hbar\omega_A(m + \tfrac{1}{2}) + \hbar\omega_B(n + \tfrac{1}{2}). \qquad (3.3)$$

In order to describe interactions of the system with light, dipole $\hat{\mu}$ and polarizability $\hat{\alpha}$ operators are needed. In equivalence to the 1D oscillator, these operators are expanded in powers of position oper-

ators $\hat{q}_A$ and $\hat{q}_B$.

$$\hat{\mu} = \left(\frac{\partial \mu}{\partial q_A}\right)_0 \hat{q}_A + \left(\frac{\partial \mu}{\partial q_B}\right)_0 \hat{q}_B + \cdots \tag{3.4}$$

$$\hat{\alpha} = \left(\frac{\partial \alpha}{\partial q_A}\right)_0 \hat{q}_A + \left(\frac{\partial \alpha}{\partial q_B}\right)_0 \hat{q}_B + \cdots . \tag{3.5}$$

In order to determine responses by time-dependent perturbation theory, we need to know the transitions induced by dipole $\hat{\mu}$ and polarizability $\hat{\alpha}$ operators. As these operators are expanded in position operators, it is sufficient to know the transitions caused by the operators $\hat{q}_A$ and $\hat{q}_B$. Expressing these operators in terms of ladder operators makes apparent, how the action of a position operator changes the state. The position operators are given by

$$\hat{q}_A = \tfrac{1}{\sqrt{2}}\left(a_A + a_A^\dagger\right) \tag{3.6}$$

$$\hat{q}_B = \tfrac{1}{\sqrt{2}}\left(a_B + a_B^\dagger\right). \tag{3.7}$$

Action of a ladder operator excites or de-excites the state by one quantum. Operator $\hat{q}_A$ therefore causes transitions $|00\rangle \leftrightarrow |10\rangle$, while action of $\hat{q}_B$ induces $|00\rangle \leftrightarrow |01\rangle$ transitions – the transitions following selection rules of the harmonic 1D oscillator.

The 2D-Raman-THz response vanishes in the harmonic case Eq. (3.1) with linear dipole (3.4) and polarizability (3.5). It was demonstrated for the 1D oscillator (Chapter 2) that breaking the symmetry, either by anharmonicity of the potential, or by nonlinearities of dipole and polarizability, lead to 2D-Raman-THz signals. In the 2D oscillator, the potential energy surface can be further disturbed by mechanical couplings, the lowest effective order being $\hat{q}_A^2\hat{q}_B$ and $\hat{q}_A\hat{q}_B^2$. Furthermore, nonlinearity of dipole and polarizability surfaces can couple both states electrically. The effects of anharmonic and electrical couplings have been explored in the context of 2D Raman spectra[70,71,74] and IR-IR-Visible spectroscopy,[93,94] which are conceptually very similar to 2D-Raman-THz spectroscopy. Here, we derive the results in equivalence to the 1D oscillator (Chapter 2) and apply them to 2D-Raman-THz spectroscopy.

3.3 Electrical Coupling

One way, by which cross peaks can be created, are electrical couplings through nonlinearity of dipole moment and polarizability surface. Instead of assuming dipole and polarizability to be linear in position operators (Eq. (3.4)), one can continue the expansion by the terms $\hat{q}_A^2$ or $\hat{q}_B^2$. This will allow zero- and two-quantum transitions of a single oscillator, and therefore lead to the one-body responses

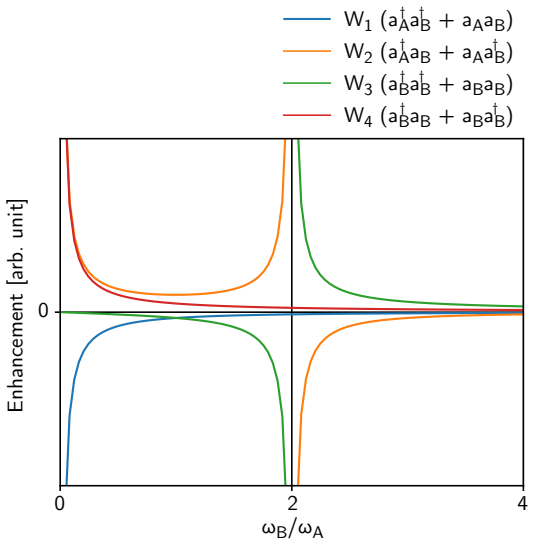

Figure 3.1: The transitions caused by anharmonic coupling λ_{AAB}, are scaled by the frequency dependent factors W_1 - W_4. $|00\rangle \leftrightarrow |11\rangle$ (W_1), $|01\rangle \leftrightarrow |10\rangle$ (W_2), $|00\rangle \leftrightarrow |02\rangle$ (W_3), and $|01\rangle \leftrightarrow |01\rangle$ (W_4) depends on the ratio $w = \omega_B/\omega_A$.

discussed in Chapter 2. In contrast, nonlinearities of the form $\hat{q}_A\hat{q}_B$ will couple the two oscillators in the presence of a field. We shall consider dipole and polarizability operators of the form

$$\hat{\mu} = \underbrace{\left(\frac{\partial \mu}{\partial q_A}\right)_0}_{\mu_A} \hat{q}_A + \underbrace{\left(\frac{\partial \mu}{\partial q_B}\right)_0}_{\mu_B} \hat{q}_B + \underbrace{\frac{1}{2}\left(\frac{\partial^2 \mu}{\partial q_A \partial q_B}\right)_0}_{\mu_{AB}} \hat{q}_A\hat{q}_B \tag{3.8}$$

$$\hat{\alpha} = \underbrace{\left(\frac{\partial \alpha}{\partial q_A}\right)_0}_{\alpha_A} \hat{q}_A + \underbrace{\left(\frac{\partial \alpha}{\partial q_B}\right)_0}_{\alpha_B} \hat{q}_B + \underbrace{\frac{1}{2}\left(\frac{\partial^2 \alpha}{\partial q_A \partial q_B}\right)_0}_{\alpha_{AB}} \hat{q}_A\hat{q}_B. \tag{3.9}$$

Expressing the product $\hat{q}_A\hat{q}_B$ in the form of ladder operators gives

$$\begin{aligned}\hat{q}_A\hat{q}_B &= \tfrac{1}{2}\left(a_A^\dagger + a_A\right)\left(a_B^\dagger + a_B\right) \\ &= \tfrac{1}{2}(a_A^\dagger a_B^\dagger + a_A a_B) + \tfrac{1}{2}(a_A^\dagger a_B + a_A a_B^\dagger),\end{aligned} \tag{3.10}$$

where two terms $a_A^\dagger a_B^\dagger$ and $a_A a_B$ cause $|00\rangle \leftrightarrow |11\rangle$ transitions, whereas the second bracket contains terms $a_A^\dagger a_B$ and $a_A a_B^\dagger$, which cause $|01\rangle \leftrightarrow |10\rangle$ transitions .

3.4 Mechanical Coupling

The lowest order coupling of two modes A and B can occur via contribution $\hat{q}_A\hat{q}_B$ to the harmonic potential (3.1). Couplings of this type can be eliminated by the right choice of normal mode coordinates.

The next higher couplings are cubic terms of the form $\hat{q}_A^2\hat{q}_B$ and $\hat{q}_A\hat{q}_B^2$. Let us have a closer look at

the first coupling by treating it as a perturbation to the harmonic oscillator

$$\begin{aligned}\hat{H}^{(1)} &= \lambda_{AAB}\hbar\omega_A \hat{q}_A^2 \hat{q}_B \\ &= 2^{-2/3}\lambda_{AAB}\hbar\omega_A \\ &\quad \times \left[{a_A^\dagger}^2 + a_A^2 + a_A^\dagger a_A + a_A a_A^\dagger\right]\left[a_B^\dagger + a_B\right].\end{aligned} \tag{3.11}$$

The anharmonic coupling $\lambda_{AAB}\hbar\omega_A = \frac{1}{6}\frac{\partial^3 V}{\partial q_A^2 \partial q_B}$ describes, how much the frequency ω_A is modulated with the deflection of oscillator B. The complementary coupling $\lambda_{ABB}\hbar\omega_B = \frac{1}{6}\frac{\partial^3 V}{\partial q_A \partial q_B^2}$ does not require separate derivation, as its solutions are obtained from the λ_{AAB} contribution by interchanging indices A and B.

Applying the perturbation (3.11) to the 2D oscillator gives perturbed wave functions $|\psi_{m,n}\rangle$ as linear combinations of harmonic oscillator eigenfunctions $|\varphi_{m,n}\rangle$ (Appendix 3.7, equation (3.44)). Operators $\hat{q}_A$ and $\hat{q}_B$ can then be expressed in the perturbed basis $|\psi_{m,n}\rangle$, which yields (Appendix 3.7)

$$\hat{q}_A = \underbrace{\left(a_A^\dagger + a_A\right)}_{\hat{q}_A^H} \tag{3.12}$$
$$+ \lambda_{AAB}\underbrace{\left[2W_1\left(a_A a_B + a_A^\dagger a_B^\dagger\right) + 2W_2\left(a_A^\dagger a_B + a_A a_B^\dagger\right)\right]}_{\hat{q}_A^{AAB}}$$

$$\hat{q}_B = \underbrace{\left(a_B^\dagger + a_B\right)}_{\hat{q}_B^H} \tag{3.13}$$
$$+ \lambda_{AAB}\underbrace{\left[W_3\left({a_A^\dagger}^2 + {a_A}^2\right) + 2W_4\left(a_A^\dagger a_A + a_A a_A^\dagger\right)\right]}_{\hat{q}_B^{AAB}}.$$

with

$$\begin{aligned}W_1 &= \frac{1}{2+w} - \frac{1}{w} \\ W_2 &= \frac{1}{2-w} + \frac{1}{w} \\ W_3 &= \frac{1}{2+w} - \frac{1}{2-w} \\ W_4 &= \frac{1}{w}.\end{aligned} \tag{3.14}$$

The factors W_1 to W_4 are dependent on the relative frequency $w = \omega_B/\omega_A$ (Figure 3.1). The first terms in equations (3.12) and (3.13) are simply $\hat{q}_A$ and $\hat{q}_B$ in harmonic eigenstate basis ($\hat{q}_A^H$ and $\hat{q}_B^H$). The small additional contributions to $\hat{q}_A$ containing $a_A a_B$ and $a_A^\dagger a_B^\dagger$ allow for the simultaneous excitation or de-excitation of both oscillators $|00\rangle \leftrightarrow |11\rangle$. The scaling factor W_1 enhances these contributions for small ω_B (strong coupling to diffusion). The last terms of equation (3.12), $a_A^\dagger a_B$ and $a_A a_B^\dagger$ cause transitions, in which excitation is transferred from one to the other oscillator ($|10\rangle \leftrightarrow |01\rangle$). These terms are scaled by W_2, which is enhanced both at $w = 0$ (diffusion coupling) and $w = 2$ (Fermi resonance).

While action of the $\hat{q}_A$ operator causes simultaneous transitions of both oscillators, the operator $\hat{q}_B$ has a quite different effect. The terms ${a_A^\dagger}^2$ and ${a_A}^2$ of equation (3.13) allow two-quantum transitions of the q_A oscillator $|00\rangle \leftrightarrow |20\rangle$, while the terms $a_A^\dagger a_A$ and $a_A a_A^\dagger$ enables zero-quantum transitions of oscillator A $|10\rangle \leftrightarrow |10\rangle$. Two-quantum transitions are scaled by W_3, which diverges at $w = 2$ (Fermi resonance), while zero-quantum transitions are enhanced at low w by the factor W_4.

Knowing the effects of electrical and mechanical couplings on the position operators, we can express dipole $\hat{\mu}$ and polarizability $\hat{\alpha}$ in the presence of both effects. If nonlinearities μ_{AB}, α_{AB} and couplings λ_{AAB}, λ_{ABB} are considered to be perturbations, we can ignore cross terms including more than one perturbation, and the operators are

$$\begin{aligned}\hat{\mu} =& \mu_A \hat{q}_A^H + \mu_B \hat{q}_B^H + \mu_{AB}\hat{q}_A^H \hat{q}_B^H \\ &+ \lambda_{AAB}\left(\mu_A \hat{q}_A^{AAB} + \mu_B \hat{q}_B^{AAB}\right) \\ &+ \lambda_{ABB}\left(\mu_A \hat{q}_A^{ABB} + \mu_B \hat{q}_B^{ABB}\right)\end{aligned} \tag{3.15}$$

$$\begin{aligned}\hat{\alpha} =& \alpha_A \hat{q}_A^H + \alpha_B \hat{q}_B^H + \alpha_{AB}\hat{q}_A^H \hat{q}_B^H \\ &+ \lambda_{AAB}\left(\alpha_A \hat{q}_A^{AAB} + \alpha_B \hat{q}_B^{AAB}\right) \\ &+ \lambda_{ABB}\left(\alpha_A \hat{q}_A^{ABB} + \alpha_B \hat{q}_B^{ABB}\right),\end{aligned} \tag{3.16}$$

where the definitions of the various position operators are given in equations (3.12) and (3.13). In the following sections, we will discuss the effects of electric couplings μ_{AB} and α_{AB}, as well as anharmonic couplings λ_{AAB} and λ_{ABB} on the 2D-Raman-THz response.

3.5 Responses

Having expressions for dipole and polarizability operators (eq. (3.15) and (3.16)), the 2D-Raman-THz responses can be derived based on time-dependent perturbation theory (Equations (1.2)) If the mechanical couplings are small enough such they do not affect the energy levels, the responses are temperature independent. It is therefore sufficient, to regard only pathways starting from the ground state $\rho_{\mathrm{eq}} = |00\rangle\langle 00|$. The harmonic contributions $\hat{q}_A^H$ and $\hat{q}_B^H$ cause $|00\rangle \leftrightarrow |10\rangle$ and $|00\rangle \leftrightarrow |01\rangle$ transitions, respectively. In additions, the couplings allow $|00\rangle \leftrightarrow |11\rangle$ and $|01\rangle \leftrightarrow |10\rangle$ transitions as well as two-quantum transitions of single oscillators. Since anharmonicities and nonlinearities are small, the relevant Feynman diagrams contain exactly one forbidden transition.

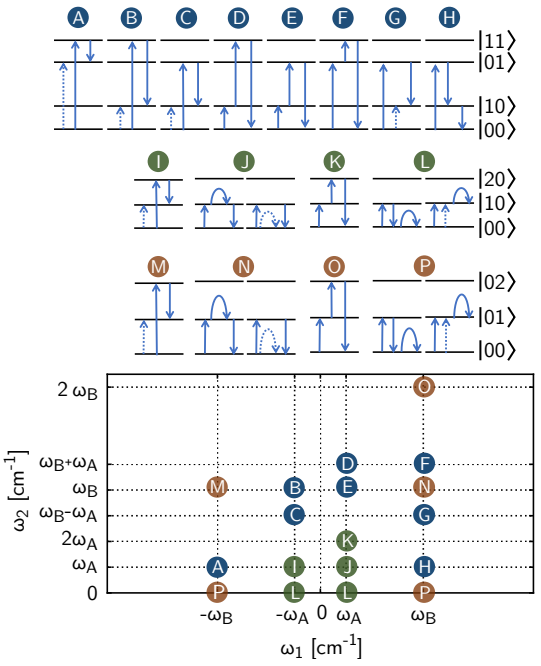

Figure 3.2: For each peak, the WMEL diagram is drawn above the spectrum, in which solid arrows indicate transitions caused by action on the ket side, while the dotted arrows stand for transitions from interactions on the bra side of the density matrix. Blue circles are cross peaks between oscillators A and B, green circles are diagonal peaks of A, and orange circles mark diagonal peaks of oscillator B.

All possible one-body peaks (pathways which include only one oscillator) and two-body peaks (pathways which include two oscillators) are illustrated in Figure 3.2, together with their corresponding energy level diagrams. The pathways starting with a two-quantum transition (in this case a coupling) cancel away in the nearly harmonic case. Therefore, only fundamental frequencies appear during t_1. A cross peak appears when the forbidden transition is a coupling (Figure 3.2, A-H). Since in this case, the forbidden transition modifies both oscillators, the remaining two interactions need to be $\hat{q}_A^H$ and $\hat{q}_B^H$. If the forbidden transition induces a two-quantum transition of a single oscillator, the other two transition need to be one-quantum transitions of the same oscillator. This gives rise to one-body peaks of oscillator A (I-L) and B (M-P). For the parameters discussed here, we get responses of the form

$$R_{\mathrm{RTT}} = \alpha_{AB} R_{\mathrm{RTT}}^{\alpha,AB} + \mu_{AB} R_{\mathrm{RTT}}^{\mu,AB} + \lambda_{AAB} R_{\mathrm{RTT}}^{\lambda,AAB} + \lambda_{ABB} R_{\mathrm{RTT}}^{\lambda,ABB} \tag{3.17}$$

$$R_{\mathrm{TRT}} = \alpha_{AB} R_{\mathrm{TRT}}^{\alpha,AB} + \mu_{AB} R_{\mathrm{TRT}}^{\mu,AB} + \lambda_{AAB} R_{\mathrm{TRT}}^{\lambda,AAB} + \lambda_{ABB} R_{\mathrm{TRT}}^{\lambda,ABB} \tag{3.18}$$

$$R_{\mathrm{TTR}} = \alpha_{AB} R_{\mathrm{TTR}}^{\alpha,AB} + \mu_{AB} R_{\mathrm{TTR}}^{\mu,AB} + \lambda_{AAB} R_{\mathrm{TTR}}^{\lambda,AAB} + \lambda_{ABB} R_{\mathrm{TTR}}^{\lambda,ABB}, \tag{3.19}$$

where responses $R^{\alpha,AB}$ gives the response to nonlinearity of polarizability, $R^{\mu,AB}$ is the response to nonlinear dipole moment and the contributions $R^{\lambda,AAB}$ and $R^{\lambda,ABB}$ are the responses due to anharmonic couplings.

In the following, the shape of the four different responses $R^{\alpha,AB}$, $R^{\mu,AB}$, $R^{\lambda,AAB}$, and $R^{\lambda,ABB}$ are derived based on time-dependent perturbation theory for the three pulse sequences RTT, TRT, and TTR. It will turn out, that the different responses show characteristic peak patterns depending on the nature of coupling. We will discuss these peak patterns on an example system with ω_A=200 cm^{-1} and ω_B=600 cm^{-1}. Analytic expressions for these responses are given in Appendix 3.8.

3.5.1 Cross Peaks from Electrical Couplings

Due to their simplicity, we will start with the discussion of responses $R^{\alpha,AB}$ and $R^{\mu,AB}$ which are caused by nonlinearity of polarizability and dipole surface. The peak intensities caused by electric couplings do not depend on oscillator frequencies. In the case of $R^{\alpha,AB}$, the Raman interaction induces $|00\rangle \leftrightarrow |11\rangle$ and $|10\rangle \leftrightarrow |01\rangle$ transitions via $\hat{q}_{AB}^H$. In the RTT sequence, the two-quantum transition can only occur at the first interaction and the signal vanishes as a consequence. On the other hand, the coupling occurs in the second interaction

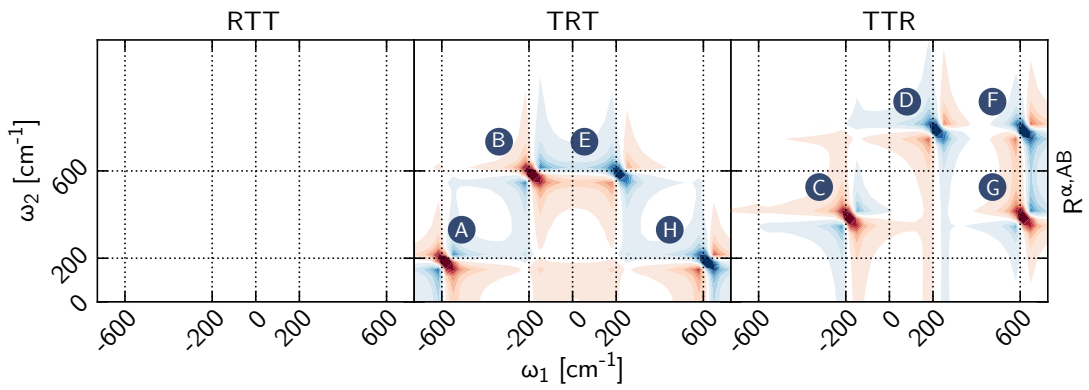

Figure 3.3: 2D Raman THz signal of the 2D oscillator generated by the nonlinearity α_{AB} ($R^{\alpha,AB}$)

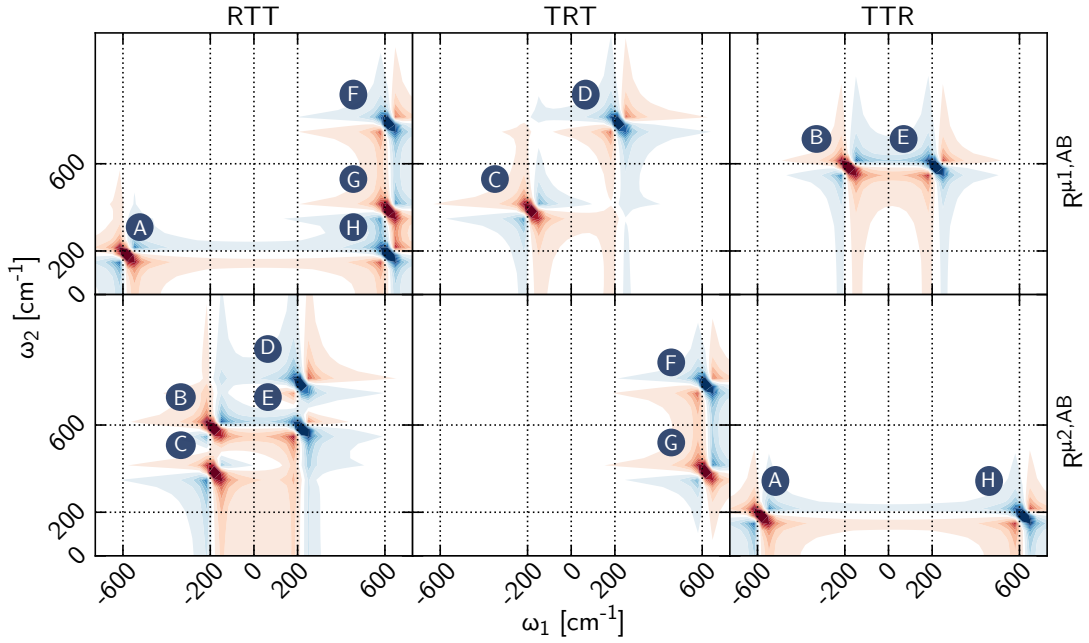

Figure 3.4: 2D Raman THz signal of the 2D oscillator generated by the nonlinearity μ_{AB}. *Upper row:* peaks which are scaled by $\mu_A\alpha_B$ ($R^{\mu 1,AB}$). and *lower row:* peaks scaled by $\mu_B\alpha_A$ ($R^{\mu 2,AB}$).

of the TRT sequence, and in the last interaction fo the TTR sequence. The relevant contributions to the $R^{\alpha,AB}$ responses are

$$R^{\alpha,AB}_{\mathrm{RTT}} = 0 \tag{3.20}$$

$$\begin{aligned} R^{\alpha,AB}_{\mathrm{TRT}} = & \\ \mu_A\mu_B\{ & \langle \hat{q}^H_A(t_1+t_2)[\hat{q}^H_{AB}(t_1),[\hat{q}^H_B(0),\rho_{eq}]]\rangle \\ & + \langle \hat{q}^H_B(t_1+t_2)[\hat{q}^H_{AB}(t_1),[\hat{q}^H_A(0),\rho_{eq}]]\rangle\} \end{aligned} \tag{3.21}$$

$$\begin{aligned} R^{\alpha,AB}_{\mathrm{TTR}} = & \\ \mu_A\mu_B\{ & \langle \hat{q}^H_{AB}(t_1+t_2)[\hat{q}^H_A(t_1),[\hat{q}^H_B(0),\rho_{eq}]]\rangle \\ & + \langle \hat{q}^H_{AB}(t_1+t_2)[\hat{q}^H_B(t_1),[\hat{q}^H_A(0),\rho_{eq}]]\rangle\}, \end{aligned} \tag{3.22}$$

and are illustrated in Figure 3.3. All the terms are scaled by $\mu_A\mu_B$, the product of transition dipoles of modes A and B. The response $R^{\alpha,AB}_{TRT}$ (Eq. (3.21)) has two contributions, one starting with single quantum transition of oscillator B (peaks A,H) and the other starting by excitation of oscillator A (peaks B, E). The response $R^{\alpha,AB}_{TTR}$ (Eq. (3.22)) can start with $\hat{q}_B$ (peaks F, G) or with transition $\hat{q}_A$ (peaks C, D). Each term in Eq. (3.21) and (3.22) produces a pair of peaks, which have same intensity but opposite sign. This ensures that integral over all peaks vanishes.

If it is the dipole surface which couples both oscillators via the nonlinearity μ_{AB}, the THz interactions can induce the transitions $|00\rangle \leftrightarrow |11\rangle$ and $|10\rangle \leftrightarrow |01\rangle$. Since there are two THz interactions, more complicated signals are to be expected. Depending if the Raman interaction excites oscillator A or B, the resulting peak will be scaled by $\mu_B\alpha_A$ or $\mu_A\alpha_B$. We can group the peaks with the same scaling into two basis responses $R^{\mu1,AB}$ and $R^{\mu2,AB}$ and write the response $R^{\mu,AB}$ as a linear combination thereof:

$$R^{\mu,AB}_{\mathrm{RTT}} = \mu_A\alpha_B R^{\mu1,AB}_{\mathrm{RTT}} + \mu_B\alpha_A R^{\mu2,AB}_{\mathrm{RTT}} \tag{3.23}$$

$$R^{\mu,AB}_{\mathrm{TRT}} = \mu_A\alpha_B R^{\mu1,AB}_{\mathrm{TRT}} + \mu_B\alpha_A R^{\mu2,AB}_{\mathrm{TRT}} \tag{3.24}$$

$$R^{\mu,AB}_{\mathrm{TTR}} = \mu_A\alpha_B R^{\mu1,AB}_{\mathrm{TTR}} + \mu_B\alpha_A R^{\mu2,AB}_{\mathrm{TTR}}, \tag{3.25}$$

with

$$\begin{aligned} R^{\mu1,AB}_{\mathrm{RTT}} = & \langle \hat{q}^H_{AB}(t_1+t_2)[\hat{q}^H_A(t_1),[\hat{q}^H_B(0),\rho_{eq}]]\rangle \\ & + \langle \hat{q}^H_A(t_1+t_2)[\hat{q}^H_{AB}(t_1),[\hat{q}^H_B(0),\rho_{eq}]]\rangle \end{aligned} \tag{3.26}$$

$$R^{\mu1,AB}_{\mathrm{TRT}} = \langle \hat{q}^H_{AB}(t_1+t_2)[\hat{q}^H_B(t_1),[\hat{q}^H_A(0),\rho_{eq}]]\rangle \tag{3.27}$$

$$R^{\mu1,AB}_{\mathrm{TTR}} = \langle \hat{q}^H_B(t_1+t_2)[\hat{q}^H_{AB}(t_1),[\hat{q}^H_A(0),\rho_{eq}]]\rangle \tag{3.28}$$

$$R^{\mu2,AB}_{\mathrm{RTT}} = \langle \hat{q}^H_{AB}(t_1+t_2)[\hat{q}^H_A(t_1),[\hat{q}^H_B(0),\rho_{eq}]]\rangle \tag{3.29}$$

$$R^{\mu2,AB}_{\mathrm{TRT}} = \langle \hat{q}^H_{AB}(t_1+t_2)[\hat{q}^H_A(t_1),[\hat{q}^H_B(0),\rho_{eq}]]\rangle \tag{3.30}$$

$$R^{\mu2,AB}_{\mathrm{TTR}} = \langle \hat{q}^H_A(t_1+t_2)[\hat{q}^H_{AB}(t_1),[\hat{q}^H_B(0),\rho_{eq}]]\rangle. \tag{3.31}$$

The peaks which are scaled by $\mu_A\alpha_B$ constitute $R^{\mu1,AB}$ (Figure 3.4, top row), whereas the peaks scaled by $\mu_B\alpha_A$ are contained in $R^{\mu2,AB}$ (Figure 3.4, bottom row). We can discuss both contributions separately.

For the $\mu_A\alpha_B$ contribution, $\hat{\alpha}$ acts via $\hat{q}^H_B$. The remaining dipole interactions must be $\hat{q}^H_A$ and $\hat{q}^H_{AB}$. In the RTT sequence, coupling can be in the second or third interaction (peaks B,C,D,E). The TRT sequence can couple only in the last interaction (peaks F,G), and the TTR sequence couples in the second interaction (peaks A, H). In the $\mu_B\alpha_A$ contributions the Raman interactions needs to act via $\hat{q}^H_A$. Also here, restrictions in the position of couplings also reduces the amount of peaks in the TRT and TTR sequences, and we are left with peaks (A,F,G,H) in the RTT sequence, (C,D) in TRT and (B,E) in TTR.

3.5.2 Cross Peaks from Mechanical Couplings

The signal generated from anharmonic couplings is complicated in two ways. Firstly, the relative peak intensities will depend on the relative oscillator frequencies $w = \omega_B/\omega_A$ via factors W_1 to W_4. Secondly, anharmonic couplings can not only produce two-body peaks (A-H) but also lead one-body peaks of either mode A (I-L) or mode B (M-P).

The signal contains two set of peaks, one scaled by $\mu_A^2\alpha_B$, and the other by $\mu_A\mu_B\alpha_A$. The response is then written as

$$R^{\lambda,AAB}_{RTT} = \mu_A^2\alpha_B R^{\lambda1,AAB}_{RTT} + \mu_A\mu_B\alpha_A R^{\lambda2,AAB}_{RTT} \tag{3.32}$$

$$R^{\lambda,AAB}_{TRT} = \mu_A^2\alpha_B R^{\lambda1,AAB}_{TRT} + \mu_A\mu_B\alpha_A R^{\lambda2,AAB}_{TRT} \tag{3.33}$$

$$R^{\lambda,AAB}_{TTR} = \mu_A^2\alpha_B R^{\lambda1,AAB}_{TTR} + \mu_A\mu_B\alpha_A R^{\lambda2,AAB}_{TTR} \tag{3.34}$$

where the two contributions $R^{\lambda1}$ and $R^{\lambda2}$ are given by the following terms:

$$\begin{aligned} R^{\lambda1,AAB}_{\mathrm{RTT}} = & \langle \hat{q}^{AAB}_A(t_1+t_2)[\hat{q}^H_A(t_1),[\hat{q}^H_B(0),\rho_{eq}]]\rangle \\ & + \langle \hat{q}^H_A(t_1+t_2)[\hat{q}^{AAB}_A(t_1),[\hat{q}^H_B(0),\rho_{eq}]]\rangle \end{aligned} \tag{3.35}$$

$$\begin{aligned} R^{\lambda1,AAB}_{\mathrm{TRT}} = & \langle \hat{q}^{AAB}_A(t_1+t_2)[\hat{q}^H_B(t_1),[\hat{q}^H_A(0),\rho_{eq}]]\rangle \\ & + \langle \hat{q}^H_A(t_1+t_2)[\hat{q}^{AAB}_B(t_1),[\hat{q}^H_A(0),\rho_{eq}]]\rangle \end{aligned} \tag{3.36}$$

$$\begin{aligned} R^{\lambda1,AAB}_{\mathrm{TTR}} = & \langle \hat{q}^H_B(t_1+t_2)[\hat{q}^{AAB}_A(t_1),[\hat{q}^H_A(0),\rho_{eq}]]\rangle \\ & + \langle \hat{q}^{AAB}_B(t_1+t_2)[\hat{q}^H_A(t_1),[\hat{q}^H_A(0),\rho_{eq}]]\rangle \end{aligned} \tag{3.37}$$

$$
\begin{aligned}
R^{\lambda 2,AAB}_{\mathrm{RTT}} = \quad & \langle \hat{q}_A^{AAB}(t_1+t_2)[\hat{q}_B^H(t_1),[\hat{q}_A^H(0),\rho_{eq}]]\rangle \\
& + \langle \hat{q}_B^H(t_1+t_2)[\hat{q}_A^{AAB}(t_1),[\hat{q}_A^H(0),\rho_{eq}]]\rangle \\
& + \langle \hat{q}_B^{AAB}(t_1+t_2)[\hat{q}_A^H(t_1),[\hat{q}_A^H(0),\rho_{eq}]]\rangle \\
& + \langle \hat{q}_A^H(t_1+t_2)[\hat{q}_B^{AAB}(t_1),[\hat{q}_A^H(0),\rho_{eq}]]\rangle \} \qquad (3.38)\\
R^{\lambda 2,AAB}_{\mathrm{TRT}} = \quad & \langle \hat{q}_A^{AAB}(t_1+t_2)[\hat{q}_A^H(t_1),[\hat{q}_B^H(0),\rho_{eq}]]\rangle \\
& + \langle \hat{q}_A^H(t_1+t_2)[\hat{q}_A^{AAB}(t_1),[\hat{q}_B^H(0),\rho_{eq}]]\rangle \\
& + \langle \hat{q}_B^H(t_1+t_2)[\hat{q}_A^{AAB}(t_1),[\hat{q}_A^H(0),\rho_{eq}]]\rangle \\
& + \langle \hat{q}_B^{AAB}(t_1+t_2)[\hat{q}_A^H(t_1),[\hat{q}_A^H(0)\rho_{eq}]]\rangle \qquad (3.39)\\
R^{\lambda 2,AAB}_{\mathrm{TTR}} = \quad & \langle \hat{q}_A^{AAB}(t_1+t_2)[\hat{q}_A^H(t_1),[\hat{q}_B^H(0),\rho_{eq}]]\rangle \\
& + \langle \hat{q}_A^H(t_1+t_2)[\hat{q}_A^{AAB}(t_1),[\hat{q}_B^H(0),\rho_{eq}]]\rangle \\
& + \langle \hat{q}_A^{AAB}(t_1+t_2)[\hat{q}_B^H(t_1),[\hat{q}_A^H(0),\rho_{eq}]]\rangle \\
& + \langle \hat{q}_A^H(t_1+t_2)[\hat{q}_B^{AAB}(t_1),[\hat{q}_A^H(0),\rho_{eq}]]\rangle. \qquad (3.40)
\end{aligned}
$$

In the case of λ_{AAB}, the coupling transitions $|00\rangle \leftrightarrow |11\rangle$ and $|10\rangle \leftrightarrow |01\rangle$ are caused by the $\hat{q}_A^{AAB}$ operator, either in the second or third interaction (since this contribution is present in both $\hat{\mu}$ and $\hat{\alpha}$ operators). In this case, the remaining two interactions need to induce single-quantum transitions of oscillators A and B via $\hat{q}_A^H$ and $\hat{q}_B^H$, respectively.

The λ_{AAB} coupling can furthermore enter via the $\hat{q}_B^{AAB}$ term, which induces two-quantum transitions of oscillator A ($|00\rangle \leftrightarrow |20\rangle$ and $|10\rangle \leftrightarrow |10\rangle$). In addition to the two-quantum transitions, reasonable pathways need two single-quantum transitions of mode A, caused by $\hat{q}_A^H$. If the Raman process induces two-quantum transitions, the pathways are scaled by $\mu_A^2\alpha_B$, otherwise they are scaled by $\mu_A\mu_B\alpha_A$.

On the example of a 2D-Oscillator with ω_A=200 cm^{-1} and ω_B=600 cm^{-1}, the contributions $R^{\lambda 1,AAB}$ (Figure 3.5, top row) and $R^{\lambda 2,AAB}$ (Figure 3.5, bottom row) are discussed. Since this system is close to Fermi resonance, the pathways are dominated by the $|10\rangle \leftrightarrow |01\rangle$ contributions (which appear in peaks C, E, G, H) and the $|00\rangle \leftrightarrow |20\rangle$ contributions (peaks I and K).

The λ_{ABB} couplings are furthermore illustrated on a the same 2D Oscillator with ω_A=200 cm^{-1} and ω_B=600 cm^{-1} (The resulting peak patterns are equivalent for λ_{AAB} of a 2D oscillator with inverted frequencies). The possible pathways are either scaled by $\lambda_{ABB}\mu_A\mu_B\alpha_B$ (Figure 3.6, top row) or by $\lambda_{ABB}\mu_B^2\alpha_A$ (Figure 3.6, bottom row). In this case, the three transitions $|00\rangle \leftrightarrow |11\rangle$, $|10\rangle \leftrightarrow |01\rangle$ (responsible for all cross peaks A-H), as well as $|10\rangle \leftrightarrow |10\rangle$ (giving diagonal peaks N and P) are enhanced.

3.6 Conclusion

The 2D oscillator model gives a sound foundation for qualitative discussion of possible cross peaks. In the nearly harmonic case, the system response can be expressed as a linear combination of "basis responses", which show specific peak patterns depending on the kind of anharmonicity that is responsible for the signal. Electrical anharmonicities μ_{AA} and α_{AA}, as well as mechanical anharmonicity σ_A cause a set of four "one-body peaks" of oscillator A (I-L). Anharmonicities μ_{BB}, α_{BB} and σ_B cause the diagonal peaks of oscillator B (M-P). These diagonal peaks have been discussed in detail in Chapter 2.

Coupling of the two modes present in the 2D oscillator, either by electrical coupling μ_{AB} and α_{AB}, or by anharmonic couplings λ_{AAB} and λ_{ABB} give further rise to a set of 8 "two-body peaks", which contain frequency information of both oscillators A and B simultaneously (peaks A-H). From two-body peak patterns observed in experiments, one can potentially distinguish contributions of electrical and anharmonic couplings to the signal. For example, the signals originating from nonlinear dipole moment μ_{AB} (Figure 3.4) and λ_{ABB} (Figure 3.6) show cross peaks at the same positions. However, they can be clearly distinguished by the relative signs of peaks. In addition, anharmonic couplings λ_{AAB} and λ_{ABB} can cause one-body peaks, and therefore can be a further cause for echoes. Fermi resonances can hereby strongly enhance the echo signal. The forbidden two-quantum transition can hereby be replaced by the allowed transition of the higher frequency oscillator.

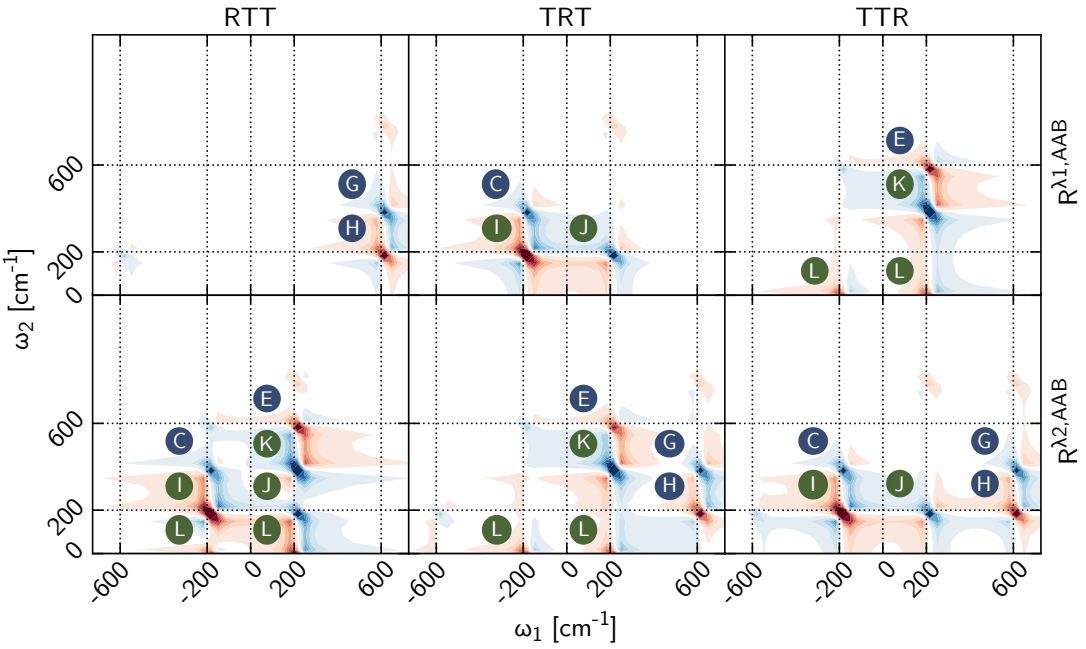

Figure 3.5: 2D Raman THz signal of the 2D oscillator, generated by the anharmonic coupling λ_{AAB} ($R^{\lambda 2,AAB}$). *Upper row:* Peaks, which are scaled by $\mu_A\mu_B\alpha_A$ and *lower row:* contributions with factor $\mu_A^2\alpha_B$ ($R^{\lambda 1,AAB}$) .

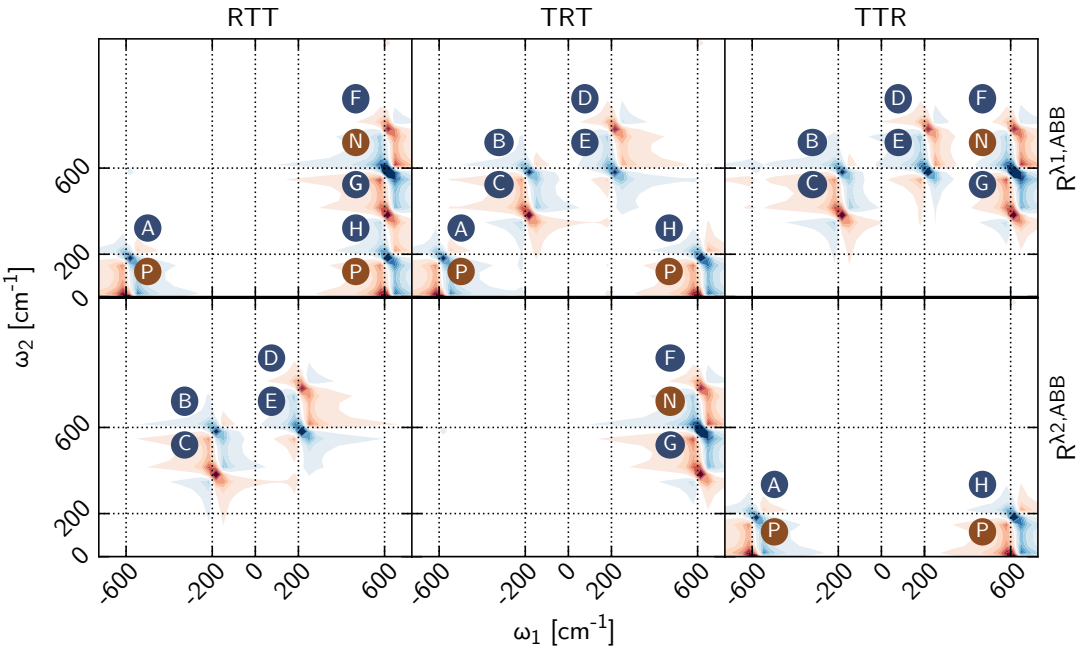

Figure 3.6: 2D Raman THz signal of the 2D oscillator, generated by the anharmonic coupling λ_{ABB}. *Upper row:* Peaks, which are scaled by $\mu_A\mu_B\alpha_B$ ($R^{\lambda 2,ABB}$) and *lower row:* contributions with factor $\mu_B^2\alpha_A$ ($R^{\lambda 1,ABB}$).

3.7 Appendix A: Derivation of Matrix Elements

The wave function up to first order in perturbation is given by

$$|\psi_{k,l}\rangle = |k,l\rangle + \sum_{i\neq k}\sum_{j\neq l}\frac{\langle i,j|\hat{H}^{(1)}|k,l\rangle}{E^0_{i,j}-E^0_{k,l}}|i,j\rangle + \cdots, \tag{3.41}$$

where the perturbed wave function $|\psi_{k,l}\rangle$ is expressed in terms $|k,l\rangle$, the eigenfunctions of the unperturbed system. For a perturbation $\hat{H}^{(1)} = \hbar\omega_A\hat{q}_A^2\hat{q}_B$, the only non-zero matrix elements $|m,n\rangle$ basis are

$$\begin{aligned}
\left\langle m+2,n+1|\hat{H}^{(1)}|m,n\right\rangle &\propto \sqrt{m+1}\sqrt{m+2}\sqrt{n+1}\\
\left\langle m+2,n-1|\hat{H}^{(1)}|m,n\right\rangle &\propto \sqrt{m+1}\sqrt{m+2}\sqrt{n}\\
\left\langle m,n+1|\hat{H}^{(1)}|m,n\right\rangle &\propto (2m+1)\sqrt{n+1}\\
\left\langle m,n-1|\hat{H}^{(1)}|m,n\right\rangle &\propto (2m+1)\sqrt{n}\\
\left\langle m-2,n+1|\hat{H}^{(1)}|m,n\right\rangle &\propto \sqrt{m}\sqrt{m-1}\sqrt{n+1}\\
\left\langle m-2,n-1|\hat{H}^{(1)}|m,n\right\rangle &\propto \sqrt{m}\sqrt{m-1}\sqrt{n}.
\end{aligned} \tag{3.42}$$

Therefore, the perturbed wave function according to equation (3.41) becomes

$$\begin{aligned}
|\psi_{m,n}\rangle = |m,n\rangle & \qquad (3.43)\\
+\hbar\omega_A\lambda_{AAB}\Bigg(& \frac{\sqrt{m+1}\sqrt{m+2}\sqrt{n+1}}{\hbar(2\omega_A+\omega_B)} \quad |m+2,n+1\rangle\\
& +\frac{\sqrt{m+1}\sqrt{m+2}\sqrt{n}}{\hbar(2\omega_A-\omega_B)} \quad |m+2,n-1\rangle\\
& +\frac{(2m+1)\sqrt{n+1}}{\hbar\omega_B} \quad |m,n+1\rangle\\
& -\frac{(2m+1)\sqrt{n}}{\hbar\omega_B} \quad |m,n-1\rangle\\
& -\frac{\sqrt{m}\sqrt{m-1}\sqrt{n+1}}{\hbar(2\omega_A-\omega_B)} \quad |m-2,n+1\rangle\\
& -\frac{\sqrt{m}\sqrt{m-1}\sqrt{n}}{\hbar(2\omega_A+\omega_B)} \quad |m-2,n-1\rangle\Bigg).
\end{aligned}$$

Expressing this equation in terms of ladder operators leads to a basis-less representation of the form

$$|\psi_{m,n}\rangle = \left(\hat{I}+\lambda_{ABB}\hat{O}\right)|m,n\rangle, \tag{3.44}$$

where $\hat{I}$ is the identity operator, and $\hat{O}$ causes the perturbation

$$\begin{aligned}
\hat{O} = & \frac{1}{2+w}\left({a_A^\dagger}^2 a_B^\dagger - a_A^2 a_B\right) \qquad (3.45)\\
& +\frac{1}{2-w}\left({a_A^\dagger}^2 a_B - a_A^2 a_B^\dagger\right)\\
& +\frac{1}{w}(a_A a_A^\dagger + a_A^\dagger a_A)\left(a_B^\dagger - a_B\right).
\end{aligned}$$

The pre-factor $\hbar\omega_A$ is thereby absorbed into the operator $\hat{O}$, which in turn only depends on the frequency ratio $w = \omega_B/\omega_A$.

An operator $\hat{A}$ can be expressed in the basis of perturbed wave functions $|\psi_{m,n}\rangle$. Since the operator $(\hat{I}+\lambda_{AAB}\hat{O})$ generates the perturbed wave function from the harmonic eigenstates, basis transform of the operator $\hat{A}$ is given by

$$\langle\psi_{i,j}|\hat{A}|\psi_{k,l}\rangle = \langle i,j|\underbrace{\left(\hat{I}+\lambda_{ABB}\hat{O}\right)^\dagger\hat{A}\left(\hat{I}+\lambda_{ABB}\hat{O}\right)}_{\hat{A}^{\mathrm{anh}}}|k,l\rangle. \tag{3.46}$$

Multiplying out the basis transform while ignoring the λ^2_{ABB} term, and making use of $\hat{O}^\dagger = -\hat{O}$ reduces the problem to the calculation of a commutator

$$\hat{A}^{\mathrm{anh}} = \hat{A}^H + \lambda_{ABB}\left[\hat{A}^H,\hat{O}\right]. \tag{3.47}$$

This expression is solved easily for $\hat{A} = \hat{q}_A \propto (a_A^\dagger + a_A)$ and $\hat{A} = \hat{q}_B \propto (a_B^\dagger + a_B)$. Making use of the commutators $[a_A^\dagger, a_A] = 1$ and $[a_A, a_B] = 0$ finally gives

$$\begin{aligned}
\left[\hat{q}_A,\hat{O}\right] = & 2W_1\left(a_A a_B + a_A^\dagger a_B^\dagger\right) \qquad (3.48)\\
& +2W_2\left(a_A^\dagger a_B + a_A a_B^\dagger\right)\\
\left[\hat{q}_B,\hat{O}\right] = & W_3\left({a_A^\dagger}^2 + {a_A}^2\right) \qquad (3.49)\\
& +2W_4\left(a_A^\dagger a_A + a_A a_A^\dagger\right).
\end{aligned}$$

with the frequency dependent scaling factors W_1 to W_4 (3.14).

3.8 Appendix B: Analytical Expressions of Basis Spectra

Analytic expressions of the two-body basis spectra are given here. Mechanical coupling λ_{AAB} can give two basis responses, $R^{\lambda 1,AAB}$ which is scaled by $\mu_A^2\alpha_B$, and $R^{\lambda 2,AAB}$ which is scaled by $\mu_A\mu_B\alpha_A$ and we have

$$R^{\lambda,AAB} = \mu_A^2\alpha_B R^{\lambda 1,AAB} + \mu_A\mu_B\alpha_A R^{\lambda 2,AAB}. \tag{3.50}$$

The possible peaks are scaled by frequency-dependent factors W_1 to W_4 (Equations (3.14))

The $\mu_A^2\alpha_B$ contributions are

$$\begin{aligned} R_{RTT}^{\lambda 1,AAB} =& + W_1\cos[-\omega_B t_1+\omega_A t_2] \\ & - W_1\cos[\omega_B t_1+(\omega_A+\omega_B)t_2] \\ & + W_2\cos(\omega_B t_1+(\omega_B-\omega_A)t_2) \\ & - W_2\cos(\omega_B t_1+\omega_A t_2) \end{aligned} \tag{3.51}$$

$$\begin{aligned} R_{TRT}^{\lambda 1,AAB} =& + W_1\cos(-\omega_A t_1+\omega_B t_2) \\ & + W_2\cos(-\omega_A t_1+(\omega_B-\omega_A)t_2) \\ & - W_1\cos(\omega_A t_1+(\omega_A+\omega_B)t_2) \\ & - W_2\cos(\omega_A t_1+\omega_B t_2) \\ & + W_3\cos(-\omega_A t_1+\omega_A t_2) \\ & - W_4\cos(\omega_A t_1+\omega_A t_2) \end{aligned} \tag{3.52}$$

$$\begin{aligned} R_{TTR}^{\lambda 1,AAB} =& + W_1\cos(-\omega_A t_1+\omega_B t_2) \\ & - W_2\cos(\omega_A t_1+\omega_B t_2) \\ & - W_3\cos(\omega_A t_1+2\omega_A t_2) \\ & + W_4\cos(\omega_A t_1) \end{aligned} \tag{3.53}$$

and the $\mu_A\mu_B\alpha_A$ contributions are expressed as

$$\begin{aligned} R_{RTT}^{\lambda 2,AAB} =& + W_1\cos[-\omega_A t_1+\omega_B t_2] \\ & + W_2\cos[-\omega_A t_1+(\omega_B-\omega_A)t_2] \\ & - W_1\cos[\omega_A t_1+(\omega_A+\omega_B)t_2] \\ & - W_2\cos[\omega_A t_1+\omega_B t_2] \\ & + W_3\cos[-\omega_A t_1+\omega_A t_2] \\ & - W_4\cos[\omega_A t_1+\omega_A t_2] \\ & - W_3\cos[\omega_A t_1+2\omega_A t_2] \\ & + W_4\cos[\omega_A t_1] \end{aligned} \tag{3.54}$$

$$\begin{aligned} R_{TRT}^{\lambda 2,AAB} =& + W_1\cos[-\omega_B t_1+\omega_A t_2] \\ & - W_1\cos[\omega_B t_1+(\omega_A+\omega_B)t_2] \\ & + W_2\cos[\omega_B t_1+(\omega_B-\omega_A)t_2] \\ & - W_2\cos[\omega_B t_1+\omega_A t_2] \\ & - W_3\cos[\omega_A t_1+2\omega_A t_2] \\ & + W_4\cos[\omega_A t_1] \end{aligned} \tag{3.55}$$

$$\begin{aligned} R_{TTR}^{\lambda 2,AAB} =& + W_1\cos[-\omega_B t_1+\omega_A t_2] \\ & + W_2\cos[-\omega_A t_1+(\omega_B-\omega_A)t_2] \\ & - W_1\cos[\omega_A t_1+(\omega_A+\omega_B)t_2] \\ & - W_1\cos[\omega_B t_1+(\omega_A+\omega_B)t_2] \\ & + W_2\cos[\omega_B t_1+(\omega_B-\omega_A)t_2] \\ & - W_2\cos[\omega_B t_1+\omega_A t_2] \\ & + W_3\cos[-\omega_A t_1+\omega_A t_2] \\ & - W_4\cos[\omega_A t_1+\omega_A t_2]. \end{aligned} \tag{3.56}$$

The λ_{ABB} analogues to the λ_{AAB} responses are received by interchange of indices A and B. Electrical coupling μ_{AB} also yields two different contributions. $R^{\mu 1}$ is scaled by $\mu_A\alpha_B$ and $R^{\mu 2}$ is scaled by $\mu_B\alpha_A$ and we have

$$R^{\mu,AB} = \mu_A\alpha_B R^{\mu 1,AB} + \mu_B\alpha_A R^{\mu 2,AB}. \tag{3.57}$$

The analytic form of these contributions are

$$\begin{aligned} R_{RTT}^{\mu 1,AB} =& + 1\cos[-\omega_B t_1+\omega_A t_2] \\ & - 1\cos[\omega_B t_1+(\omega_A+\omega_B)t_2] \\ & + 1\cos[\omega_B t_1+(\omega_B-\omega_A)t_2] \\ & - 1\cos[\omega_B t_1+\omega_A t_2] \end{aligned} \tag{3.58}$$

$$\begin{aligned} R_{TRT}^{\mu 1,AB} =& + 1\cos[-\omega_A t_1+(\omega_B-\omega_A)t_2] \\ & - 1\cos[\omega_A t_1+(\omega_A+\omega_B)t_2] \end{aligned} \tag{3.59}$$

$$\begin{aligned} R_{TTR}^{\mu 1,AB} =& + 1\cos[-\omega_A t_1+\omega_B t_2] \\ & - 1\cos[\omega_A t_1+\omega_B t_2] \end{aligned} \tag{3.60}$$

and

$$\begin{aligned} R_{RTT}^{\mu 2,AB} =& + 1\cos[-\omega_A t_1+\omega_B t_2] \\ & + 1\cos[-\omega_A t_1+(\omega_B-\omega_A)t_2] \\ & - 1\cos[\omega_A t_1+(\omega_A+\omega_B)t_2] \\ & - 1\cos[\omega_A t_1+\omega_B t_2] \end{aligned} \tag{3.61}$$

$$\begin{aligned} R_{TRT}^{\mu 2,AB} =& - 1\cos[\omega_B t_1+(\omega_A+\omega_B)t_2] \\ & + 1\cos[\omega_A t_1+(\omega_B-\omega_A)t_2] \end{aligned} \tag{3.62}$$

$$\begin{aligned} R_{TTR}^{\mu 2,AB} =& + 1\cos[-\omega_B t_1+\omega_A t_2] \\ & - 1\cos[\omega_B t_1+\omega_A t_2]. \end{aligned} \tag{3.63}$$

The electrical coupling α_{AB} gives responses in which all peaks are scaled by $\mu_A\mu_B$. The corresponding basis spectrum is

$$R_{RTT}^{\alpha,AB} = 0 \tag{3.64}$$

$$\begin{aligned} R_{TRT}^{\alpha,AB} =& + 1\cos[-\omega_B t_1+\omega_A t_2] \\ & + 1\cos[-\omega_A t_1+\omega_B t_2] \\ & - 1\cos[\omega_A t_1+\omega_B t_2] \\ & - 1\cos[\omega_B t_1+\omega_A t_2] \end{aligned} \tag{3.65}$$

$$\begin{aligned} R_{TTR}^{\alpha,AB} =& + 1\cos[-\omega_A t_1+(\omega_B-\omega_A)t_2] \\ & - 1\cos[\omega_A t_1+(\omega_A+\omega_B)t_2] \\ & - 1\cos[\omega_B t_1+(\omega_A+\omega_B)t_2] \\ & + 1\cos[\omega_B t_1+(\omega_B-\omega_A)t_2]. \end{aligned} \tag{3.66}$$

Chapter 4

Development of Water Force Fields

The content of this chapter has been published with the title "An Efficient Water Force Field Calibrated against Intermolecular THz and Raman Spectra" [D. Sidler, M. Meuwly and P. Hamm, *J. Chem. Phys.* **148**, 244504 (2018)]

4.1 Abstract

A polarizable water model is presented which has been calibrated against experimental THz and Raman spectra of bulk water. These low-frequency spectra directly probe the dynamics, and thereby intermolecular interactions, on time scales relevant to molecular motions. The model is based on the TL4P force field developed by Tavan and coworkers [J. Phys. Chem. B **117** , 9486 (2013)], which has been designed to be transferable between different environments; in particular, to correctly describe the electrostatic properties of both the isolated water molecule in the gas-phase and the liquid water at ambient conditions. Following this design philosophy, TL4P was amended with charge transfer across hydrogen-bonded dimers as well as an anisotropic polarizability in order to correctly reproduce the THz and Raman spectra. The thermodynamic and structural properties of the new model are of equal quality as those of TL4P, and at the same time, an almost quantitative agreement with the spectroscopic data could be achieved. Since TL4P is a rigid model with a single polarizable site, it is computationally very efficient, while the numerical overhead for the addition of charge transfer and the anisotropic polarizability is minor. Overall, the model is expected to be well suited for, e.g., large scale simulations of 2D-Raman-THz spectra or biomolecular simulations.

4.2 Introduction

Although being a fairly simple molecule, water exhibits very complex behavior in the condensed phase with many anomalies in its thermodynamic properties whose origin still are a matter of debate.[3,111] These anomalies play a crucial role for understanding solvation effects on various processes. Vibrational spectroscopy can be applied to gain information about its structure and dynamics. From mid-IR spectra measuring the intramolecular degrees of freedom of the water molecule, one can draw conclusions about the surroundings of individual water molecules from the lineshape function of the absorption peaks. 2D IR spectroscopy can be used to distinguish contributions of homogeneous and inhomogeneous broadening of the environment, and as such insights about the dynamics of the environment can be gained.[34–36,107,108,112–114]

By contrast, spectroscopy in the THz regime directly measures the inter-molecular dynamics of the hydrogen bonding network of water and can potentially resolve the structural heterogeneity within bulk water to a certain extent. The modes in the THz range are very delocalized,[23] and it is difficult to distinguish between an oscillator and its environment. Furthermore, the water molecules move in a very anharmonic potential, and the lifetime of hydrogen bonds was reported to be in the range of $\approx 1\,\mathrm{ps}$.[115] This inhomogeneous and very dynamic environment causes strong broadening of all spectral features. The THz absorption spectrum (Fig. 4.1b, black line) has three to a certain extent distinct bands,[21] which are interpreted by the modes illustrated in Fig. 4.1a. The maximum intensity band at $600\,\mathrm{cm}^{-1}$ arises from librational modes (hindered rotation), the weaker band at $200\,\mathrm{cm}^{-1}$ belongs to hydrogen bond vibrations, and a faint shoulder at $50\,\mathrm{cm}^{-1}$ originates from hydrogen bond bending modes. The Raman spectra show the same three bands, but with very different relative intensities (Fig. 4.1c, black line).[50] Higher order THz spectroscopy has the potential to bet-

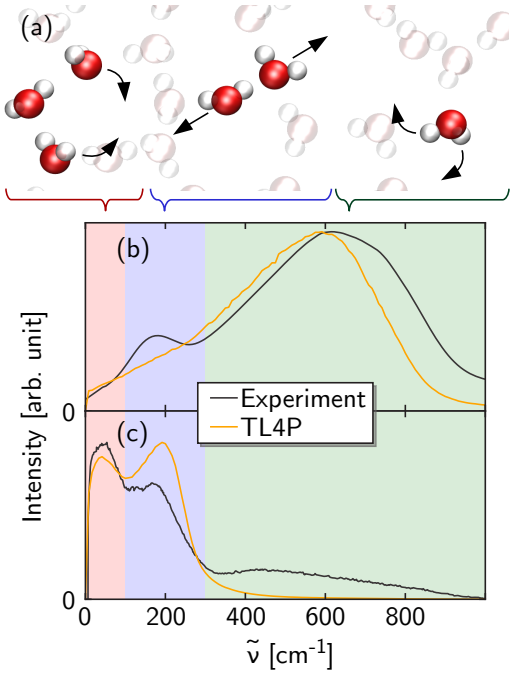

Figure 4.1: (a) Illustration of the vibrational modes associated for the three bands visible in the THz range (the vibrations might be more delocalized in reality). (b) Experimental THz absorption spectrum of water (multiplied with the experimental refractive index) at 25 °C (black),[21] compared to that calculated from the TL4P model (orange).[89] (c) The same for the anisotropic Raman spectrum measured by optical Kerr effect spectroscopy.[50]

ter resolve the spectral features and thereby refine these assignments.[41] Currently, 2D-Raman-THz is the only 2D method in this spectral range that has successfully been applied to water[98] and aqueous salt solutions,[79] but the interpretation of these nonlinear responses remains a challenge.

Computer simulations can contribute to a microscopic understanding of the THz and Raman responses. Due to the large anharmonicity of the intermolecular degrees of freedom of liquid water, a description based on harmonic normal modes is problematic.[70,116] However, the low frequency of the motions around k_BT make classical molecular dynamics (MD) a good tool to model these intermolecular vibrations, thereby capturing the full anharmonicity of the intermolecular potential. MD simulations directly follow the time-evolution of the system, and the calculation of various space and time correlation functions is straight forward in principle. It is desirable to use MD simulations to derive relationships between spectral features and molecular structure and motions on a microscopic scale.

The simulation of response functions in the THz range requires a water model with the following properties. Firstly, as is true for any water force field, it should accurately represent the intermolecular energies, from which realistic forces, structures and dynamics are generated. Furthermore, in order to simulate a Raman spectrum, which is related to the autocorrelation function of the polarizability, the water model needs to be polarizable. A multitude of polarizable water force fields have been developed, treating polarizability in many different ways, i.e., Drude oscillator models,[117–122] first principle water models,[123–125] models including three-body interactions explicitly,[126,127] fluctuating charge models,[128,129] and models with an inducible dipole moment[92,130–138] or higher electrostatic moments.[133,139,140] Beyond that –and that is no longer standard for most water models– the electrostatic properties need to be fine-tuned to reproduce accurate transition dipoles as well as transition polarizabilities so that the relative intensities in the THz and Raman spectra agree with experiment. Moreover, the simulation of higher order response functions requires very extensive sampling of phase space, for which simulation times of a few 100 μs are needed. Computational efficiency of the model thus is very important. The purpose of this work is to develop a water model that fulfills all these criteria.

In order to avoid the "polarization catastrophe", most polarizable water force fields use a polarizability that is smaller than the experimen-

tal value of 1.47 Å^3; for example SWM4-NDP uses 0.98 Å^3.[119] However, such a model can only poorly describe the interaction with the homogeneous electric field from a laser pulse needed for the Raman response. Applying a damping to the dipole-dipole interaction at short distances with a Thole-type interaction[141] can circumvent this problem. A Gaussian inducible dipole has the same effect,[142,143] which is the basis of a series of water models recently introduced by Tavan and co-workers.[95,138] As a cornerstone in the design of these models, the dipole moment and polarizability of an isolated water molecule was set to the experimental gas phase value. This design philosophy ensures that the models are transferable to different environments, and, as a side aspect, also correctly accounts for a Raman interaction with an external laser field. The models are furthermore rigid and thus computationally efficient. We, in turn, have argued that 2D-Raman-THz spectroscopy is particularly sensitive to the correct description of the polarizability of a force field, and have shown that amongst different off-the-shelf water models tested, the TL4P model[95] gave the best agreement with the experimental 2D-Raman-THz response.[89] We therefore think that TL4P is a good starting point for a "spectroscopic force field" that focuses on the inter-molecular degrees of freedom in the THz range.

Here, we aim at further improving TL4P as a spectroscopic force field. Fig. 4.1 (orange *versus* black lines) shows that TL4P does not even fully reproduce the (1D) THz absorption and Raman spectra, which certainly should be considered a minimum requirement for modelling 2D-Raman-THz spectroscopy. Two major differences catch the eye: First, the 600 cm^{-1} band in the Raman spectrum is completely missing in the TL4P simulations, since the polarizability in TL4P is assumed to be isotropic. The 600 cm^{-1} band is a librational mode, i.e., a hindered rotation of individual water molecules. In order that such a rotation changes the polarizability of a water molecule in the laboratory frame, and thereby renders that degree of freedom visible in the Raman spectrum, the polarizability needs to be anisotropic. Second, the simulated THz absorption spectrum severely underestimates the intensity of the 200 cm^{-1} band. It is well known that a point charge model (such as TIP4P/2005[144]) misses the hydrogen bond vibration completely since two fixed dipoles vibrating against each other will not change the overall dipole.[23] That is, while the corresponding mode exists in a MD simulations of a point charge model, it does not have any transition dipole. Polarizability introduces a transition dipole of that vibration; since the overall dipole is modulated with intermolecular distance, however, TL4P underestimates the intensity of this band severely.

The purpose of this paper is to amend the electrostatics of the TL4P model[95] in such a way that both bands obtain a realistic transition polarizability and transition dipole, respectively. For the Raman band at 600 cm^{-1}, we need to allow for an anisotropic polarizability. Experimentally, the polarizability of an isolated water molecule is nearly isotropic. While the polarizability is commonly assumed to be isotropic in water force fields, its anisotropy is a crucial aspect in the description of the Raman spectrum.

As for the intensity of the THz band at 200 cm^{-1}, we add charge transfer to the TL4P model. It is well established that hydrogen bonding causes a small amount of charge to flow from the hydrogen bond acceptor to the hydrogen bond donor.[122,145–151] It has been demonstrated by Torii that a very simple treatment of this effect, where the transferred charge is defined as a function of the hydrogen bond length, can capture the intensity of the hydrogen bond vibration band.[?] In these simulations, however, separate sets of charges were used for the force field and for the calculation of the THz spectrum. A similar approach was taken by Tanimura and co-workers, who concentrated on the effect of charge transfer on the Raman spectra.[92] However, it is desirable to have one and the same force field for the MD simulation as well as the calculation of the spectroscopy.[152] To that end, Rick and co-workers have developed a way to integrate charge flow into a force field in a self-consistent manner[153] and applied it to a Drude model.[122]

In this paper, a total of three new force fields are parametrized, verified with respect to their thermodynamic properties, and THz absorption and anistropic Raman spectra are calculated: The TL4P$^{\mathrm{i}}$-CT model, which adds charge flow across a hydrogen bond to the TL4P model in a self-consistent manner but still assumes an isotropic polarizability, TL4P^{a1}-CT, for which in addition the polarizability has been replaced by the experimental anisotropic polarizability tensor, and TL4P^{a2}-CT, which reduces the anisotropy of the polarizability in such a way that the intensity of the 600 cm^{-1} Raman band matches experiment. We will see that TL4P^{a2}-CT reveals almost perfect THz absorption and Raman spectra, setting the stage for an in-depth investigation of the various features observed in 2D-Raman-THz spectroscopy.[98]

4.3 Simulation Details

All MD simulations were performed with a home-written MD code. If not stated otherwise, the systems simulated were cubic boxes containing 256 water molecules under periodic boundary conditions. Long-range electrostatic interactions were treated by Ewald summation,[143] with the dielectric constant of the surrounding continuum set to the experimental value of $\epsilon_{\mathrm{RF}} = 78$. The van der Waals potentials were switched to zero between 8.55 Å and 9.5 Å, and a long-range correction term for energy and pressure of the van der Waals potential was applied.[154] The inducible dipole moments were calculated according to

$$\boldsymbol{\mu}_i = \boldsymbol{\alpha}_i \left(\boldsymbol{E}_{ext} + \sum_{j \neq i} \left(\boldsymbol{E}_j + \boldsymbol{T}_{ij} \boldsymbol{\mu}_j \right) \right) \qquad (4.1)$$

where $\boldsymbol{\mu}_i$ is the induced dipole of water i, $\boldsymbol{\alpha}_i$ its polarizability in the laboratory frame, $\boldsymbol{E}_j$ the electrical field the point charges of water j produce at the position of water i, $\boldsymbol{T}_{ij}$ the dipole-dipole interaction tensor, and $\boldsymbol{E}_{ext}$ an external field needed to calculate the Raman response (it was switched off during the force calculation in the MD simulation). Eq. 4.1 was solved iteratively for the $\boldsymbol{\mu}_i$ until the changes are less than 10^{-6} e Å, which took in average 6 iterations (the computational cost of that iteration is about 3 times that for the point charges and van der Waals potential). The equation of motion was integrated using a velocity Verlet algorithm[155] with a time step of 1 fs. The geometry of the water molecules was constrained using the M-SHAKE algorithm.[156] All simulations were carried out in the NVT ensemble at density $\rho = 0.9965$ g/cm^3 and temperature 300 K, where temperature was controlled with a velocity rescaling thermostat with a coupling time of 1 ps.[157] The instantaneous pressure was calculated using the virial expression.[158] Varying simulation lengths ranging from 500 ps to 50 ns have been used for the different tasks (which are specified below), depending on the desired accuracy of a particular property and how quickly it converges. Error bars have been determined by block averaging.

All density functional theory (DFT) calculations were performed with the Gaussian plane wave formalism implemented in the CP2K program.[159,160] As in Tavan's work,[95,138] the exchange- and correlation functional of Perdew, Burke and Ernzerhof (PBE) was used.[161] The electron density was expanded in augmented, quadruple zeta basis sets with three sets of polarization functions for both H and O atoms.[162] Only the electrons of the outermost shell were treated explicitly, while the core electrons were treated by Goedecker-Teter-Hutter pseudopotentials.[163,164] The considered water clusters were centered into a box with size 15 Å under non-periodic boundary conditions with a plane wave basis cutoff of 150 Ry.

4.4 Parametrization

4.4.1 TL4P Model

As all water models developed here start from TL4P,[95] we first introduce this model. TL4P is a rigid water model with the atoms fixed to the experimental liquid phase geometry ($r_{\mathrm{OH}} = 0.968$ Å, bond angle $\theta = 105.3\,^\circ$). The electrostatic interactions are arising from three point charges, two of which are located on the hydrogen atoms and one on a massless point M that is displaced from the oxygen atom (see Fig. 4.2). Furthermore, a Gaussian polarizable site is placed on the oxygen atom with an isotropic polarizability that matches the experimental value $\alpha_{\mathrm{iso}} = 1.47$ Å.[165] The charges q_{M} and q_{H} and distance l_{OM} of site M from the oxygen atom are constrained such that the molecule has no net charge, and that the dipole moment of an isolated water molecule agrees with the experimental gas phase value $\mu = 1.855$ D. The two remaining free parameters determining the electrostatics, l_{OM} and the width of the Gaussian σ, were fit such that the electrostatic moments of a water molecule in a realistic liquid phase environment agrees best with a DFT water molecule placed in the same environment.[95]

The Pauli repulsion and van der Waals interactions are modeled with a Buckingham potential acting between oxygen atoms,

$$V_{\mathrm{VdW}}(r) = A_1 \exp(-A_2 r) - B/r^6. \qquad (4.2)$$

The Buckingham parameters were empirically fit to match the following experimental quantities, all at density $\rho = 0.9965$ g/cm^3 and temperature 300 K: the position of the first peak in the O-O radial distribution function (RDF)($r_{\max} = 2.76$ Å), the pressure ($p = 1$ bar) and the average potential energy per water molecule ($\langle E_{\mathrm{pot}} \rangle = -9.92$ kcal/mol).[166]

4.4.2 Charge Transfer

The amount of overall charge δq transferred across a hydrogen bond is defined as a function of the

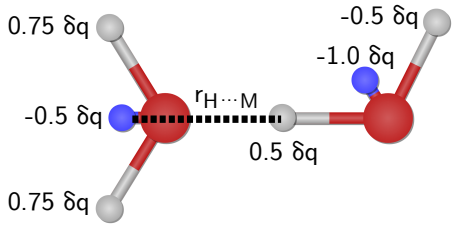

Figure 4.2: Redistribution of the charge $\delta q(r_{\mathrm{H}\cdots\mathrm{M}})$ (which is calculated from Eq. 4.3) among the atoms of the two waters of a hydrogen bonded dimer. The red spheres are oxygen atoms, the white spheres are hydrogen atoms, and the blue spheres represent the massless dummy particles M. In addition to this charge transfers, the hydrogen atom and the dummy particle carry the point charges q_H and q_M, respectively, reported in Tab. 4.1.

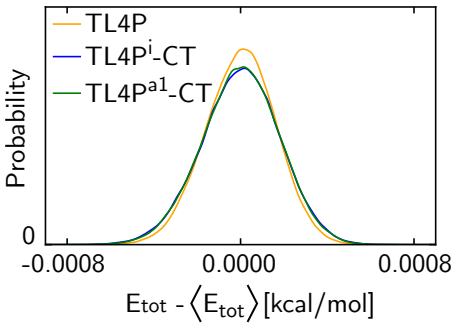

Figure 4.3: Distribution of total energy per water molecule from NVE simulations with tight convergence criteria.

hydrogen bond distance $r_{\mathrm{H}\cdots\mathrm{M}}$, for which we chose a single sided parabola:

$$\delta q(r_{\mathrm{H}\cdots\mathrm{M}}) = \begin{cases} \frac{1}{2} q_{\mathrm{CT}} \left(r_{\mathrm{H}\cdots\mathrm{M}} - r_{\mathrm{CT}}\right)^2 & \text{if } r_{\mathrm{H}\cdots\mathrm{M}} < r_{\mathrm{CT}} \\ 0, & \text{otherwise} \end{cases} . \tag{4.3}$$

Torii has shown that this functional form gives a electron population derivative that agrees well with QM calculations.[?] For each pair of water molecules, four intermolecular H$\cdots$M distances exist in principle along the lines of Eq. 4.3, yet, typically only one contributes in a pair of hydrogen-bonded waters, since the cut-off r_{CT} is very small (*vide infra*). Based on quantum-chemistry calculations,[?,147] it has been suggested to redistribute that charge transfer $\delta q(r_{\mathrm{H}\cdots\mathrm{M}})$ among the atoms of the two water molecules as illustrated in Fig. 4.2.

Expressions for energy and force contributions have been derived by Rick and co-workers.[153] Their numerical implementation is a bit tedious but straight-forward. We have verified the correctness of our implementation by testing the energy stability in an NVE run with very tight convergence criteria. For both TL4P and TL4P$^{\mathrm{i}}$-CT, the total energy of the simulation is Gaussian distributed with about the same width (Fig. 4.3, orange and blue), confirming that energy does not drift significantly during the course of the 300 ps simulation time. Furthermore, since the cutoff r_{CT} is small, the extra computational cost is minor ($\approx 5\%$) and scales linearly with the system size.

4.4.3 Anisotropic Polarizability

For the TL4P$^{\mathrm{a1}}$-CT model, the polarizability tensor is set to the experimental anisotropic gas phase polarizability with α_{xx} =1.468 Å^3, α_{yy} = 1.415 Å^3, and α_{zz} = 1.528 Å^3, where x is the direction of the dipole moment axis, y is the axis perpendicular to the plane, and z is the direction from one hydrogen atom to the other.[165] We can separate that polarizability into two contributions:

$$\boldsymbol{\alpha} = \alpha_{\mathrm{iso}} \mathbf{1} + \boldsymbol{\alpha}_{\mathrm{aniso}}, \tag{4.4}$$

the isotropic polarizability α_{iso} and the traceless anisotropy tensor $\boldsymbol{\alpha}_{\mathrm{aniso}}$. We will see that the experimental anisotropy over-estimates the intensity of the 600 cm^{-1} band in the Raman spectrum (see Fig. 4.8d). By linearly interpolating between the experimental anisotropic and isotropic polarizability $\alpha_{\mathrm{iso}}\mathbf{1}$ as to correctly describe the intensity of the 600 cm^{-1} band, we get the polarizability α_{xx} = 1.4692, α_{yy} = 1.4427, and α_{zz} = 1.4992 Å^3, which has been used in the construction of the TL4P$^{\mathrm{a2}}$-CT model.

Also the addition of an anisotropic polarizability is computationally inexpensive ($\approx$ 1.5 %) and scales linearly with the number of water molecules. For the calculation of the forces, one has to account for the fact that the induced dipole moments are no longer parallel to the electric field and thus produce an additional torque that acts on the water molecule as a whole. By solving a system of linear equations, that torque is redistributed into forces acting on the atoms, which are calculated in such a way that the force on the center of mass, as well as the forces along the bonds, vanish. As for the charge transfer, the correct implementation has been verified by testing the energy stability (Fig. 4.3, green).

4.4.4 Fitting Procedure

In re-parametrizing the modified force fields TL4P$^{\mathrm{i}}$-CT, TL4P$^{\mathrm{a1}}$-CT, and TL4P$^{\mathrm{a2}}$-CT with the polarizabilities reported in Sec. 4.4.3, we sticked as closely as possible to the design philosophy of

TL4P,[95] and tried to modify its parameters as little as possible. That is, we retained the molecular geometry from TL4P (r_{OH} = 0.968 Å and θ = 105.3 °) as well as the width of the Gaussian inducible dipoles (σ = 0.842 Å). Our initial intention has been to also keep the electrostatic parameters from TL4P (q_M=-1.1154 e, q_H=0.5577 e and l_{OM} = 0.2419 Å, see Table 4.1) in order to get a gas phase dipole moment of 1.855 D. However, the charge redistribution scheme of Fig. 4.2 enlarges the dipole moment of individual water molecules, and we found that it increases the electrostatic interactions too strongly. In order to compensate for the additional attracting forces, the static dipole moment had to be reduced by 2% (*vide infra*). We thus chose $q_M = -1.0963$ e and $q_H = 0.54815$ e for the charges, and decided to keep l_{OM} = 0.2419 Å. The static dipole moment then is μ^{stat} = 1.818 D.

After assigning q_M, q_H, l_{OM}, θ, $\boldsymbol{\alpha}$ and σ, the only free parameters determining the electrostatics of the model are the charge transfer parameters r_{CT} and q_{CT} from Eq. 4.3. Their values were optimized to give the best agreement of the dipole moment of small water clusters with dipole moments from DFT calculations, according to following procedure. Using the TL4P force field, a 500 ps long MD trajectory was produced with coordinates saved in steps of 1 ps. One water molecule was randomly selected from each of these snapshots. For this water molecule, all neighbors were selected with a O-O distance smaller than 3.5 Å. In this way, 500 water clusters consisting of 4 to 9 water molecules were generated.

The total dipole moments $\boldsymbol{M}_i^{QM}$ of all clusters i were calculated with the help of DFT calculations (see Sec. 4.3 for details). For the sake of calculating the corresponding dipole moments $\boldsymbol{M}_i^{MM}$ of the various molecular mechanics (MM) water models and comparing them to $\boldsymbol{M}_i^{QM}$, the charges and polarizabilities of the former had to be slightly modified in order to reflect the gas phase dipole moment and polarizability of DFT water. The values calculated are μ^{DFT} = 1.805 D for the dipole moment and α_{xx}^{DFT} = 1.542 Å^3, α_{yy}^{DFT} = 1.504 Å^3, and α_{zz}^{DFT} = 1.591 Å^3 for the polarizability. The root mean square deviation (RMSD) between $\boldsymbol{M}_i^{QM}$ and $\boldsymbol{M}_i^{MM}(q_{CT}, r_{CT})$, averaged over all clusters, has then been calculated as a function of charge transfer parameters. Minimizing the RMSD reveals q_{CT} = 0.0529 e and r_{CT} = 2.813 Å for TL4P^i-CT, see Fig. 4.4a. We chose to use that set of parameters for all water models, isotropic and anisotropic.

Modifying the electrostatic parameters changes the interactions between water molecules, which requires to re-parametrize the van der Waals parameters A_1, A_2, and B (Eq. 4.2). As done for TL4P,,[95] we fitted them to the position of the first peak in the O-O radial distribution function, the pressure (p = 1 bar) and the average potential energy per water molecule ($\langle E_{pot} \rangle$ = −9.92 kcal/mol). The target of position of the first peak in the O-O radial distribution function has been a little larger (r_{max} = 2.8 Å) than for TL4P, as this is the best accepted experimental value.[167] The slight adjustment of the static charges q_M and q_H, reducing the static dipole by 2% relative to that of TL4P, has been necessary to find a set of van der Waals parameters that reproduce all target values r_{max}, E_{pot}, and p at the same time. All parameters are summarized in Table 4.1, where they are also compared to TL4P.

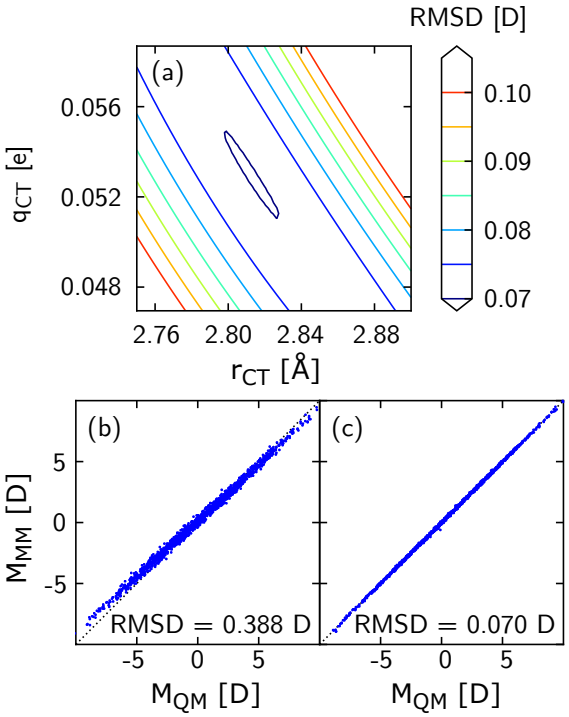

Figure 4.4: (a) RMSD of TL4P^a-CT *versus* DFT as a function of r_{CT} and q_{CT}. Correlation of the dipole moment of the 500 test clusters calculated (b) for TL4P and (c) for TL4P^a-CT *versus* DFT, plotting the x, y and z components of the dipole moments individually.

4.5 Model Verification

4.5.1 Electrostatics

The dipole moments calculated from the fitted models are in excellent agreement with DFT dipole moments with an RMSD of only 0.070 D, which is 5.5 times smaller than the RMSD calculated for

Table 4.1: Force field parameters of the TL4P model and the newly developed charge transfer models

Parameter	TL4P[95]	TL4P^{i}-CT	TL4P^{a1}-CT	TL4P^{a2}-CT
l_{OM} [Å]	0.2419	0.2419	0.2419	0.2419
θ [°]	105.3	105.3	105.3	105.3
σ [Å]	0.842	0.842	0.842	0.842
α_{xx} [Å^3]	1.47	1.47	1.468	1.4692
α_{yy} [Å^3]	1.47	1.47	1.415	1.4427
α_{zz} [Å^3]	1.47	1.47	1.528	1.4992
q_M [e]	-1.1154	-1.0963	-1.0963	-1.0963
q_H [e]	0.5577	0.54815	0.54815	0.4815
q_{CT} [e]	-	0.0529	0.0529	0.0529
r_{CT} [Å]	-	2.813	2.813	2.813
A_1 [kcal/mol]	84120	191600	196150	192300
A_2 [Å^{-1}]	3.55	3.8016	3.8101	2.8032
B [Å^6 kcal mol^{-1}]	992	1000.7	1000.7	1000.7

TL4P (Fig. 4.4b and c). Adding charge transfer not only improves the correlation for small dipole moments, but also for high dipole moments around -10 D or 10 D (see Fig. 4.4c). Although more data points exist from smaller clusters with smaller dipole moments, the model has good quality also for higher values of the dipole moments arising from the bigger clusters. This observation supports the conclusion that including charge transfer across hydrogen bonds improves the dipole moment surface for the right physical reason.

For a hydrogen bonded water dimer with H $\cdots$ M distance of 1.85 Å, the amount of charge transferred is 0.025 e, which is consistent with values reported from various QM calculations at different levels of theory ranging from HF to MP2.[145–148,150] A Water molecule in a liquid water box, on the other hand, is neutral in average, but its charge fluctuates with a standard deviation of 0.013 e (Fig. 4.5a). The average dipole increases from 2.48 D to 2.52 D when going from TL4P to TL4P^{i}-CT (Figure 4.5b), despite the fact that the dipole of the corresponding gas-phase monomers had been reduced from 1.855 D to 1.818 D. Furthermore, the fluctuation amplitude of the dipole moment slightly increases from 0.136 D to 0.150 D.

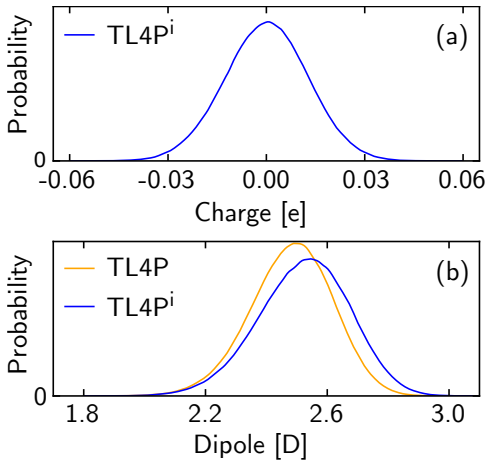

Figure 4.5: (a) Molecular charge distribution of a TL4P^{i}-CT water molecule in liquid water and (b) molecular dipole moment distribution of TL4P and TL4P^{i}-CT. Since the water molecules are charged in the case of TL4P^{i}-CT, the dipole moment depends on the choice of a reference point. We chose the geometrical midpoint of the charged sites (i.e., H and M sites) as reference point, which is equivalent to subtracting the net charge evenly from these sites.

4.5.2 Thermodynamic and Structural Properties

In the following, various experimental observables were calculated for the new water models, based on similar techniques as those used to characterize the original TL4P model.[95] We start with the

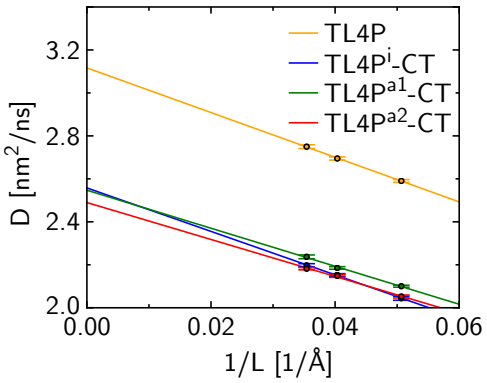

Figure 4.6: Box-size dependent diffusion constant plotted against $1/L$, where L is the box size, together with linear fits used to extract the size-corrected diffusion constant D_0 and the viscosity η.

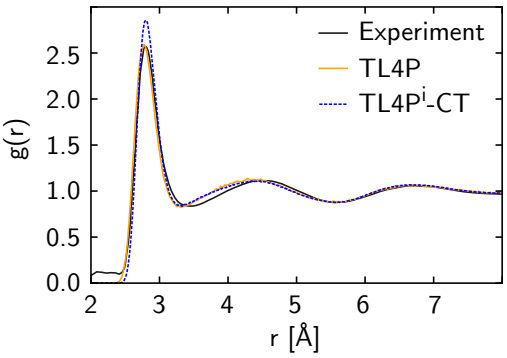

Figure 4.7: RDF of TL4P and TL4P^{i}-CT compared to the experimental RDF.[167] The RDFs of TL4P^{a1}-CT and TL4P^{a2}-CT are virtually the same as that of TL4P^{i}-CT and are not shown.

dielectric constant:[168]

$$\epsilon_{\mathrm{rel}} = \frac{1 + \frac{\langle \boldsymbol{M}^2\rangle - \langle \boldsymbol{M}\rangle^2}{3\epsilon_0 V k_B T} \frac{2\epsilon_{\mathrm{RF}}}{2\epsilon_{\mathrm{RF}}+1}}{1 - \frac{\langle \boldsymbol{M}^2\rangle - \langle \boldsymbol{M}\rangle^2}{3\epsilon_0 V k_B T} \frac{1}{2\epsilon_{\mathrm{RF}}+1}}. \tag{4.5}$$

Here, the standard deviation of the total dipole moment has been averaged during ∼45 ns, initially in an environment with the experimental dielectric constant $\epsilon_{\mathrm{RF}} = 78$. The dielectric constant has then been iterated self-consistently until $\epsilon_{\mathrm{rel}} \approx \epsilon_{\mathrm{RF}}$ within the uncertainty of the calculation.

The isothermal compressibility κ_T,[169] the thermal expansion coefficient α_p[170] and the heat capacity c_p, all at T =300 K and experimental density $\rho = 0.9965$, were derived from numerical differentiation by varying ρ by ± 0.0015 g/cm^3 and T by ±5 K:

$$\kappa_T = \left.\frac{\partial \ln \rho}{\partial p}\right|_T \tag{4.6}$$

$$\alpha_p = -\left.\frac{\partial \ln \rho}{\partial T}\right|_p \tag{4.7}$$

$$c_p = \left.\frac{\partial E_{\mathrm{tot}}}{\partial T}\right|_p + \Delta C_{\mathrm{QM}}, \tag{4.8}$$

where $\Delta C_{\mathrm{QM}} = -2.22\,\mathrm{cal\,mol^{-1}\,K^{-1}}$ is a correction for quantum mechanical contributions (from internal degrees of freedom, as well as quantum mechanical character of the librations) to theheat capacity.

The diffusion constant was calculated from:

$$D = \frac{1}{6}\left.\frac{dc(t)}{dt}\right|_{t=t_0}. \tag{4.9}$$

at $t_0 = 90$ ps by numeric differentiation. The autocorrelation function $c(t) = \left\langle (\boldsymbol{r}(t) - \boldsymbol{r}(0))^2 \right\rangle$ was averaged over a simulation time of 27 ns. Size-dependent diffusion constants were calculated in that way for boxes containing 256, 507, and 750 water molecules. From these results, the size-corrected diffusion constant D_0 and viscosity η were extracted by utilizing the relationship:[171,172]

$$D = D_0 - \frac{k_B T \zeta}{6\pi\eta V^{1/3}} \tag{4.10}$$

where V is the volume of the simulation box and $\zeta \approx 2.837$ is a constant originating from the Ewald summation in a cubic periodic box. A linear fit of the size-dependent diffusion constant as a function of $1/L = 1/V^{1/3}$ reveals D_0 from the intercept and the viscosity η from the slope (Fig. 4.6). The results of all these calculations are summarized in Table 4.2. Finally, Fig. 4.7 shows the O-O radial distribution functions.

Generally speaking, the adding anisotropic polarizability does barely affect the thermodynamic and structural properties of the force field, which is why we restrict the discussion to a comparison of TL4P with TL4P^{i}-CT. The O-O RDF (Figure 4.7) of the fitted models have a first peak at 2.80 Å (by construct) with a height of 2.82, which is higher than that of TL4P (2.59), and also higher than the experimental value (2.57).[167] At distances larger than 3.5 Å, the RDF from TL4P and TL4P^{i}-CT are almost identical. The similar long-range structuring is attributed to the same long-range electrostatic interactions, when charge transfer no longer plays any significant role. Compared to the experimental RDF, however, the second peak is shifted to shorter distances (4.29 Å versus 4.45 Å, respectively), indicating that both models underestimate the tetrahedrality of the second solvation layer. On the other hand, the height of minima and maxima after the first peak agree well with experiment.

The calculated values for the pressure and potential energy for TL4P are $p = -168$, bar and $E_{\mathrm{pot}} = -9.958$ kcal/mol, lower than the values re-

Table 4.2: All observables calculated for the new water models, compared to experiment and values obtained from TL4P, at 300 K and a density of 0.9965 g cm^{-3}. In case of TL4P, the results reported in Ref. 95 are given (6th column) together with those calculated with exactly the same procedures as for the new models (5th column) for better comparison (both sets of numbers differ slightly, since the electrostatic interactions were calculated differently in Ref. 95, and since we applied a long-range correction for the van der Waals potential.)

	TL4P^{i}-CT	TL4P^{a1}-CT	TL4P^{a2}-CT	TL4P	TL4P^{95}	exp
r_{max} [Å]	2.80 ± 0.01	2.80	2.80 ± 0.01	2.77 ± 0.01	2.76	2.80[167]
E_{pot} [kcal/mol]	-9.9199 ± 0.0007	-9.923 ± 0.001	-9.9230 ± 0.0001	-9.9580 ± 0.0005	-9.92	-9.92[166]
p [bar]	-14 ± 3	-26±2	-25 ± 2	-168 ± 2	1	1 [173]
ϵ_{rel}	86 ± 2	84 ± 3	85 ± 3	69 ± 3	77	78 [174]
D_0 [nm^2/ns]	2.49±0.02	2.56±0.02	2.55±0.02	3.12±0.01	3.0	2.4 [175]
η [mPa s]	0.64±0.03	0.70±0.04	0.73±0.05	0.60±0.01	0.80	0.81 [176]
α_p [10^{-4}/K]	6.4 ± 0.2	6.4 ± 0.2	6.4 ± 0.2	6.1± 0.1	5.9	2.8 [177]
κ_T [10^{-6}/atm]	35 ± 2	42 ± 2	37 ± 2	39 ± 2	37.4	45.6 [177]
c_p [cal/(mol K)]	20.5 ± 0.1	20.3 ± 0.1	20.4 ± 0.1	18.9 ± 0.1	18.7	18.0

ported by Tavan and co-workers.[95] This reflects the different treatment of electrostatic long-range interactions, as well as the long-range correction to the van der Waals potential that we applied here. Since it has been a fitting target, the corresponding numbers agree well with experiment for all models TL4P^{i}-CT, TL4P^{a1}-CT, and TL4P^{a2}-CT. The thermal expansion coefficient α_p increases slightly from $6.1 \cdot 10^{-4}$ to $6.4 \cdot 10^{-4}$ K^{-1} upon addition of charge transfer. This is more than double the experimental value of $2.8 \cdot 10^{-4}$ K^{-1}.[177] This discrepancy reflects the failure of TL4P, as well as of all our new models, to correctly describe the density maximum of water at 4°C and is considered to be a major drawback of all these models. The isothermal compressibility stays the same within the uncertainty of the calculation. The heat capacity increases from 18.9 to 20.5 cal mol^{-1} K^{-1}, while the dielectric constant increases from 69 to 86.

Concerning dynamical properties, we observe that the diffusion constant D_0 decreases from 3.1 to 2.5 nm^2/ns, while viscosity increases from 0.60±0.01 to 0.64±0.03 mPa s in TL4P^{i}-CT, and further to 0.73±0.05 mPa s in TL4P^{a2}-CT.

4.6 Spectra

4.6.1 Vibrational density of states

To obtain a basis for discussing differences between water models in the THz and Raman spectra, we first consider the vibrational density of states (VDOS), which is related to the dynamics only and thus can be used to disentangle effects of dynamics from the electronic contributions to the spectra, i.e., the transition dipoles and transition polarizabilities. The VDOS has been calculated from the velocity autocorrelation function of either the oxygen or the hydrogen atoms,

$$\mathrm{VDOS_{O,H}}(\omega) = \mathrm{Re} \int_0^\infty dt\ e^{i\omega t} \langle \boldsymbol{v}_{\mathrm{O,H}}(0) \cdot \boldsymbol{v}_{\mathrm{O,H}}(t) \rangle, \tag{4.11}$$

where the velocity autocorrelation has been apodized at 4 ps and $\langle \cdots \rangle$ denotes an ensemble average as well as time average, the latter over a 1.5 ns long trajectory. In VDOS of the hydrogen atoms ($\mathrm{VDOS_H}$, see Figure 4.8b) the three bands corresponding to hydrogen bond binding, hydrogen bond vibration, and libration are present. By contrast, the 600 cm^{-1} band is absent in $\mathrm{VDOS_O}$ (Figure 4.8a), which shows that librations are dominated by motions of the hydrogen atoms (Figure 4.1a). Upon addition of charge transfer, the 200 cm^{-1} and the 600 cm^{-1} bands are shifted slightly toward higher frequencies, indicating a somewhat stronger hydrogen bonding, while the amplitude of the hydrogen-bond vibration at 200 cm^{-1} is reduced somewhat (Figure 4.8a, orange *versus* blue line). For both the oxygen and the hydrogen VDOS, addition of anisotropic polarizability has no visible effect (see the red dashed line in Figs. 4.8a and 4.8b; the result for TL4P^{a1}-CT is virtually identical and is not shown).

4.6.2 THz absorption spectrum

The THz absorption spectrum (Figure 4.8c) has been calculated from the dipole-dipole autocorrelation function,[178]

$$I_{\mathrm{THz}}(\omega) n(\omega) \propto \tanh\left(\frac{\beta\hbar\omega}{2}\right) \mathrm{Im} \int_0^\infty dt\, e^{i\omega t}\, \langle \boldsymbol{\mu}(t) \cdot \dot{\boldsymbol{\mu}}(0) \rangle\,, \tag{4.12}$$

where the dipole autocorrelation function has been apodized at 4 ps, $\langle \cdots \rangle$ denotes a time average over a 7 ns long trajectory, $n(\omega)$ is the experimental refractive index, and $\tanh(\beta\hbar\omega/2)$ a quantum correction factor.[179] The dipole moment $\boldsymbol{\mu}(t)$ of the

simulation box as a whole has contributions from the static charges q_i, the induced dipole moments due to polarizability $\boldsymbol{\mu}_i$, and from charge transfer δq_i. The latter renders the water-molecules non-neutral, which calls for care when calculating the dipole moment in connection with the periodic boundary conditions; one cannot simply sum over all charges including the charge transfers $\boldsymbol{\mu} = \sum_i \boldsymbol{\mu}_i + \boldsymbol{r}_i(q_i + \delta q_i)$. In order to circumvent that problem, we calculated the contribution of charge transfer to the overall dipole independent from the other two contributions (which are not problematic). If two waters in a hydrogen-bonded dimer are in different image boxes, the minimum image convention is used for the calculation of the dipole that originates from the charge transfer across that dimer.

The THz absorption spectrum of TL4P almost completely lacks the band at $200\,\mathrm{cm}^{-1}$ (Figure 4.8c, orange line). As anticipated by the work of Torii,[151] that band appears by adding charge transfer (Figure 4.8c, blue line). Comparison with the VDOS (Figure 4.8a) emphasizes that this effect is not due to modified nuclear dynamics; rather it reflects the fact that charge transfer gives that vibration a transition dipole. Its intensity, measured relative to that of the $600\,\mathrm{cm}^{-1}$ band, agrees reasonably with experiment. The intensity and position of the $600\,\mathrm{cm}^{-1}$ band, on the other hand, are not affected by charge transfer. Going from isotropic to anisotropic polarizability has no effect on the absorption spectrum; the absorption spectra of TL4P$^{\mathrm{i}}$-CT, TL4P$^{\mathrm{a1}}$-CT, and TL4P$^{\mathrm{a2}}$-CT are virtually the same. The librational band of all water models (including TL4P) is at slightly lower frequency than in the experimental spectrum ($590\,\mathrm{cm}^{-1}$ *versus* $620\,\mathrm{cm}^{-1}$). A similarly shifted frequency is commonly observed for various rigid four point water models[89,104] and might originate from underestimating the orientational confinement due to the simplicity of the electrostatics of these four point models or due the use of only one van der Waals site on the oxygen. Conversely, the hydrogen bond stretching mode around the $200\,\mathrm{cm}^{-1}$ is at slightly too high frequency in all water models using charge transfer, an effect that is also seen in the VDOS. This indicates that the force fields somewhat overestimate the hydrogen-bond strength, probably for the same reason as the too large amplitude of the first peak in the RDF (Figure 4.7). A Gaussian distribution for the point charges (and not only the induced dipoles) might also be a way to further improve the model.

4.6.3 Anisotropic Raman spectrum

The anisotropic Raman spectrum (Figure 4.8d) was calculated from the polarizability-polarizability autocorrelation function:[178]

$$I^{ani}_{\mathrm{Raman}}(\omega) \propto \mathrm{Im} \int_0^\infty dt e^{i\omega t} \left\langle \mathrm{tr}\left[\boldsymbol{\Pi}^{ani}(t) \cdot \dot{\boldsymbol{\Pi}}^{ani}(0)\right]\right\rangle \tag{4.13}$$

with

$$\boldsymbol{\Pi}^{ani} = \boldsymbol{\Pi} - 3\mathrm{tr}\left[\boldsymbol{\Pi}\right]\mathbf{1}. \tag{4.14}$$

Here, the instantaneous polarizability $\boldsymbol{\Pi}(t)$ of the simulation box as a whole is:

$$\boldsymbol{\Pi}(t) = \frac{\partial \boldsymbol{\mu}(t)}{\partial \boldsymbol{E}_{ext}}, \tag{4.15}$$

which is calculated by numerical differentiation with respect to an external field $\boldsymbol{E}_{ext}$, varying it by $\pm 0.003\, e/\mathrm{Å}^2$.

Adding charge transfer to TL4P with isotropic polarizability (i.e., TL4P$^{\mathrm{i}}$-CT) slightly increases the frequency of the 200 cm^{-1} band (Figure 4.8 d), as already seen in the VDOS (Figures 4.8a and 4.8b). At the same time, the intensities of both the 50 cm^{-1} and 200 cm^{-1} bands are reduced (Fig. 4.8 c blue *versus* orange line), with the effect being more pronounced for the 200 cm^{-1} band. Since the effect of inter-molecular fields and an external field is additive, the addition of charge transfer in the form of Eq. (4.3) does not affect the polarizability of the simulation box as a whole if the geometry would be the same. That is, if one takes the derivative Eq. 4.15 of Eq. 4.1:

$$\boldsymbol{\Pi}(t) = \sum_{i \neq j} \boldsymbol{\alpha}_i \left(\mathbf{1} + \boldsymbol{T}_{ij}\boldsymbol{\alpha}_j\right), \tag{4.16}$$

the result is a complicated function of structure (via $\boldsymbol{T}_{ij}$ and the fact that the $\boldsymbol{\alpha}_i$ need to be rotated into the laboratory frame), but the contribution of $\boldsymbol{E}_j$ disappears, which is where charge transfer enters. As such, the change in the Raman spectrum originates from structural or dynamical differences between the TL4P and the TL4P^{i}-CT models. The reduction of the intensity is however more than one would expect from the decreased VDOS is decreased at 200 cm^{-1} (Figure 4.8 d).

Again as anticipated, including anisotropic polarizability in in TL4P$^{\mathrm{a1}}$-CT and TL4P$^{\mathrm{a2}}$-CT, the librational mode around $600\,\mathrm{cm}^{-1}$ (Fig. 4.8c red and green line) obtains transition polarizability. When using the experimental anisotropic polarizability tensor[165] in TL4P$^{\mathrm{a1}}$-CT, its intensity is overestimated (Fig. 4.8c, green line), which is why we linearly interpolated in TL4P$^{\mathrm{a2}}$-CT between

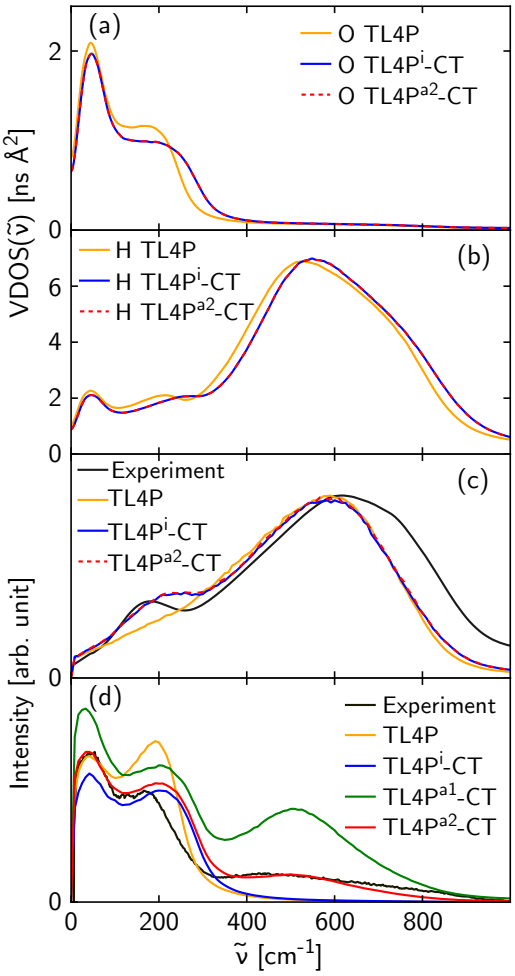

Figure 4.8: (a) Vibrational density of states of the O-atoms and (b) the H-atoms. (c) THz absorption spectra, and (d) anisotropic Raman spectra. Experimental data are shown in black (panels (c) and (d)),[21,62] while the simulation results for TL4P are shown in orange, TL4P^{i}-CT in blue, TL4P^{a1}-CT in green, and TL4P^{a2}-CT in red. In some cases (panels (a)-(c)), the models with anisotropic polarizability are virtually indistinguishable from TL4P^{i}-CT, in which case TL4P^{a1}-CT is not shown and TL4P^{a2}-CT is shown as the red dashed line (panel (a)-(c)). While the experimental spectrum has been scaled to the simulated ones with an arbitrary factor in panels (c) and (d), the scaling of the spectra of the various water models among each other is absolute and the intensities of the various peaks can be compared directly.

the experimental anisotropic polarizability and an isotropic polarizability as to match the relative intensities of the 600 cm^{-1} and 200 cm^{-1} bands (Fig. 4.8c, red line). We find that the intensity of the 600 cm^{-1} band scales roughly quadratically with the anisotropy of the polarizability tensor $\boldsymbol{\alpha}_{\text{aniso}}$ (defined by equation 4.4). Interestingly, addition of an anisotropic polarizability regains intensity for the 50 cm^{-1} band, despite the fact that the VDOS is practically identical (Figs 4.8 a and 4.8 b, red *versus* blue line) . In contrast to the hydrogen bond stretch vibration, the hydrogen bond bending modes include a rotation of water molecules, giving that mode additional transition polarizability; hence the intensity of the 50 cm^{-1} band is affected more by including anisotropic polarizability than the 200 cm^{-1} band.

4.7 Conclusion and Outlook

In conclusion, we have amended the TL4P model of Tavan and co-workers[95] with charge transfer and an anisotropic polarizability, using a mixed quantum-chemical/empirical approach. The goal has been to correctly describe both the THz absorption and the Raman spectrum in a frequency range 0-1000 cm^{-1}, where the intermolecular modes of water are found. While the addition of charge transfer required a re-parametrization of the van der Waals parameters, despite the fact that the average amount of charge is small (0.025), the small anisotropic correction of the polarizability did not further affect the thermodynamic properties of the model. In parameterizing the models, we tried to only minimally change the parameters of the original TL4P model, and we were furthermore guided by the design philosophy of TL4P,[95] namely that the dipole moment and polarizability of a water monomer should reflect the experimental gas phase value. We had to compromise at two points, i.e., reduce the dipole moment by 2% relative to the experimental value and fit the anisotropy of the polarizability as to match the experimental intensity of the librational mode. Considering the simplicity of the charge transfer model, the improvement of the dipole moment of small water clusters upon the addition of charge transfer is quite remarkable (Fig. 4.4).

The thermodynamic properties are of equal quality as those of TL4P with an overall good agreement with experiment (see Tab. 4.2; the thermal compressibility and consequently also the density maximum are an exception to that statement). On the other hand, the diffusion constant and viscosity decreases/increases to a value much closer to

experiment. The water force fields developed using the design principle of TL4P generally tend to overestimate the diffusion constant, and charge transfer seems to be a good way to slow down the motions without greatly affecting the thermodynamics. This observation probably reflects the fact that charge transfer strengthens the directional hydrogen bonds on the expense of the isotropic van der Waals interactions.

Concerning the inter-molecular THz absorption and Raman spectra, the final result of TL4P^{a2}-CT reveals an almost perfect agreement with experiment, in particular with regard to the relative intensities of the various contributions (Figs. 4.8c and 4.8d, red *versus* black line). We use one set of electrostatic parameters for the calculation of both the forces in the MD simulation and the dipole moments for the calculation of the THz and Raman spectra; hence both are calculated in a self-consistent way. One might argue that the potential energy surface and dipole moment surface might be better described by independently optimized functions. For example, point charge models tend to use "effective charges", which are designed to mimic the intermolecular forces but do not necessarily reflect the real charge distribution of the system, the latter of which determines the spectroscopy. If a force field has only few degrees of freedom, trying to fit potential energy surface and dipole moment surface simultaneously will decrease the quality of the force field because compromises will have to be made. On the other hand, once one is using an *ab initio* derived electrostatic function together with polarizability and in addition adjusting it to THz absorption and Raman spectra, which measure the dynamics of those charges very directly; one should be able to represent the real charge distribution quite realistically. In this regard, one should also keep in mind that Coulomb interactions are long-ranged. As such charge transfer effects, which manifest themselves in the THz absorption spectrum, must have consequences on the structure of water even on larger distances. The changes in the VDOS and Raman spectra emphasize that this is indeed the case. We are convinced that the mixed quantum chemical/empirical approach for fitting the TL4P models together with their physically motivated cornerstones can lead to very transferrable water force fields.

The present work also illustrates that force field refinement by fitting to reference spectroscopic data is a powerful way to improve empirical energy functions. This is because the experimentally determined spectroscopic features directly probe the dynamics, and thereby intermolecular interactions, on time scales relevant to molecular motions. Approaches similar in spirit to the present work have been applied for example to improve energy functions for understanding the proton transfer dynamics in small molecules.[180,181]

Our primary motivation for developing these water models is the modelling of 2D-Raman-THz spectroscopy.[89] An obvious prerequisite for that purpose is a model that correctly describes the (1D) THz absorption and Raman spectra, which we now have at our hands with TL4P^{a2}-CT. But the series of models, TL4P, TL4P^{i}-CT and TL4P^{a2}-CT offers an additional avenue via the possibility to switch on and off the $200\,\mathrm{cm}^{-1}$ (THz) and the $600\,\mathrm{cm}^{-1}$ bands (Raman) at wish. Assigning spectroscopic features in 2D-Raman-THz spectra is a cumbersome task, since they strongly overlap and since a calculation based on a full-atom MD simulation is largely black-box. Being able to switch on and off certain bands will greatly facilitate the assignment of diagonal and in particular cross peaks in the 2D-Raman-THz spectrum of water. Work in this direction is currently ongoing.

But more generally speaking, we think of 2D-Raman-THz spectroscopy as a spectroscopic method that is extremely sensitive to the accuracy with which one describes the polarizability of a water model.[89] While a point charge model such as TIP4P/2005 with its average polarisation probably describes the structure of bulk water quite well,[182] it must fail at least to a certain extent once water comes into contact with e.g. a hydrophobic surface of a protein since its polarisation and hence Coulombic interactions will be different. Only a polarizable force field can describe that situation correctly, and the information about polarizability is encoded in 1D THz and Raman spectra, and even more so in 2D-Raman-THz spectra. At the same time, a polarizable water force field needs to be computationally inexpensive in order to be competitive for biomolecular simulations. This calls for a rigid water model, in which case one can then take advantage of a longer integration time step of typically 2 fs. The additional computational cost for charge transfer and anisotropic polarizability is minor. We wish to advocate TL4P^{a2}-CT a computationally very efficient force field with a very good polarizability function.

Chapter 5

2D Raman THz Spectra from Molecular Dynamics Simulations

5.1 Introduction

The experimental 2D-Raman-THz signal of liquid water has several features protruding from the instrument response (Figure 1.10 *b*), the center of attention being the echo signal, which is extending along the $t_1 = t_2$ diagonal. The echo lifetime indicates the duration during which information is retained in the system, and is therefore a good measure for the inhomogeneity of the hydrogen bonding network. Unlike for the echo, there is no simple physical picture for the additional features appearing in the signal. It is unclear, what additional information about the system can be gained from 2D-Raman-THz spectroscopy. Further theoretical investigation of the 2D-Raman-THz signal is necessary to elucidate the mechanisms, which are responsible for these additional features.

Simple model systems based on perturbed harmonic oscillators have ben examined in Chapters 2 and 3. The resulting responses have been shown to take a variety of different shapes, depending on the details of the model system. The simple, closed form of the resulting responses makes apparent the connection between spectral features and their underlying physical properties. Of course, the simplicity of these systems comes with drawbacks. The conceptual framework does not intrinsically consider relaxation processes. As a consequence, spectral line shapes have to be treated in a rather *ad hoc* manner, either by assuming a functional form of the frequency autocorrelation, or by explicitly coupling the system to bath modes.[69,91]

Due to the low frequency of intermolecular vibrations, they can be described by classical equations of motions. This enables the derivation of nonlinear responses from MD trajectories. In MD simulation, the system moves on the full (anharmonic) potential energy surface represented by the force field. In this way, spectral line shapes are directly gained from realistic system motion. On the downside, the mapping of the complete phase space onto a two-dimensional spectrum is a rather convoluted process, behind which the physical reasons for spectral features are hidden.

For a correct description of 2D-Raman-THz spectra, accurate representations of dipole and polarizability surfaces are required. As a minimum requirement, the force fields should hence reproduce 1D THz and Raman spectra. The set of force fields developed in Chapter 4 attempts to meet these reqiurements by improving dipole and polarizability of the TL4P force field in a controlled manner. Addition of charge transfer (going from TL4P to TL4P^i-CT) corrects the intensity of the hydrogen bond stretching band in the THz spectrum. Furthermore, introducing anisotropic polarizability (from TL4P^i-CT to TL4P^a-CT) gives transition polarizability to molecular rotations, thereby turning on the libration band in the Raman spectrum.

By switching between the force fields TL4P, TL4P^i-CT, and TL4P^a-CT, one can selectively modify the hydrogen bond stretching mode or the libration mode in the 1D spectra. In the light of 2D-Raman-THz spectroscopy, this set of force fields can be used as a tool to examine contributions from these two modes individually, and thereby help the assignment of different features.

In Section 5.3, this set of force fields is applied to calculate spectra from room temperature water. The results are compared to experiment, and effects of charge transfer and anisotropic polarizability on the 2D spectra are discussed. Finally, 2D-Raman-THz spectrum of amorphous ice is calculated using the same set of force fields. Amorphous ice is structurally similar to liquid water, but follows a simplified dynamics. Due to the slow dynamics in amorphous ice, the lifetime of the echo

will be increased, and echoes can be assigned with more certainty. Moreover, the simplified dynamics will allow more detailed analysis of the spectra, which will be the focus of Chapter 6.

5.2 Calculation of Spectra from Molecular Dynamics

In order to derive 2D-Raman-THz responses from MD simulations, the hybrid equilibrium-nonequilibrium approach developed by Y. Tanimura and coworkers is used.[76] Here, we will briefly introduce the concepts behind the hybrid approach. After discussing both non-equilibrium and equilibrium approaches for the determination of 1D spectra, the hybrid approach for 2D spectra is introduced.

5.2.1 Non-Equilibrium Approach

In the non-equilibrium approach, the responses are determined by explicitly perturbing the system with external electrical fields, with the intent to mimic the experiment.

We start with the system in equilibrium. Although the different system properties (such as dipole moment μ and polarizability α) undergo fluctuations on a microscopic scale, their values become constant in bulk phase. Upon the action of an external electrical field (at $t = 0$), the system will follow non-equilibrium dynamics, until it once again reaches equilibrium. While the system is away from equilibrium, the observables become time-dependent even on a macroscopic scale. Time-dependent dipole moment $\mu(t)$ and polarizability $\alpha(t)$ are directly related to the observed 1D THz and Raman spectra.

In MD, the interaction with an electric field leads to forces determined by

$$\delta F_{\mathrm{THz}} = \left(\frac{\partial F}{\partial E_x}\right) \delta E_x, \tag{5.1}$$

while forces due to non-resonant Raman are calculated according to

$$\delta F_{\mathrm{Raman}} = \left(\frac{\partial^2 F}{\partial E_x^2}\right) \delta E_x^2. \tag{5.2}$$

The derivatives $\frac{\partial F}{\partial E_x}$ and $\frac{\partial^2 F}{\partial E_x^2}$ can be calculated numerically, by evaluating the forces in the presence of external fields. In order to determine the 1D THz spectrum, the equilibrated system is perturbed by the forces arising from the finite field δE_x (5.1). For numerical stability, the system is perturbed once by $+\delta F_{\mathrm{THz}}$, producing the non-equilibrium trajectory $r_+(t)$, and once by the negative forces $-\delta F_{\mathrm{THz}}$ giving rise to the trajectory $r_-(t)$. During the non-equilibrium trajectories, the dipole moments $\mu_+(t)$ and $\mu_-(t)$ are evaluated. Finally, the THz signal is calculated by

$$S_{\mathrm{THz}}(t) \propto \langle \mu_+(t) - \mu_-(t) \rangle \tag{5.3}$$

where $\langle \cdots \rangle$ denotes the average over multiple non-equilibrium trajectories. In the same way the 1D Raman signal can be determined from non-equilibrium trajectories resulting from the perturbations $+\delta F_{\mathrm{Raman}}$ and $-\delta F_{\mathrm{Raman}}$ (Equation (5.2)). The Raman signal is then given as

$$S_{\mathrm{Raman}}(t) \propto \langle \alpha_+(t) - \alpha_-(t) \rangle. \tag{5.4}$$

5.2.2 Equilibrium Approach

On the other hand, the equilibrium approach determines the same response functions without explicitly perturbing the system, simply by observing fluctuations of system properties.

The equations which relate equilibrium dynamics to spectra can be derived from quantum mechanical response functions

$$S_{\mathrm{THz}}(t) \propto \mathrm{Tr}\big(\hat{\mu}(t)\,[\hat{\mu}(0), \rho_{\mathrm{eq}}]\big) \tag{5.5}$$

$$S_{\mathrm{Raman}}(t) \propto \mathrm{Tr}\big(\hat{\alpha}(t)\,[\hat{\alpha}(0), \rho_{\mathrm{eq}}]\big). \tag{5.6}$$

In the classical limit a commutator $[\hat{a}, \hat{b}]$ is replaced by the poisson bracket

$$\{a, b\}_{\mathrm{PB}} = \frac{\partial a}{\partial q}\frac{\partial b}{\partial p} - \frac{\partial a}{\partial p}\frac{\partial b}{\partial q}, \tag{5.7}$$

which gives the expression

$$S_{\mathrm{THz}}(t) \propto \mathrm{Tr}\big(\mu(t)\{\mu(0), \rho_{\mathrm{eq}}\}_{\mathrm{PB}}\big) \tag{5.8}$$

$$S_{\mathrm{Raman}}(t) \propto \mathrm{Tr}\big(\alpha(t)\{\alpha(0), \rho_{\mathrm{eq}}\}_{\mathrm{PB}}\big). \tag{5.9}$$

Using the fact, that the density operator $\rho_{\mathrm{eq}}(q, p)$ is proportional to the Boltzmann factor $\exp[H(q, p)/k_B T]$ and by applying Hamiltons equation $\frac{\partial H}{\partial p} = \dot{q}$ we can simplify Poisson brackets in equations (5.8) to (5.9) as follows:

$$\{\mu, \rho_{\mathrm{eq}}\}_{\mathrm{PB}} \propto \dot{\mu}\rho_{\mathrm{eq}} \tag{5.10}$$

$$\{\alpha, \rho_{\mathrm{eq}}\}_{\mathrm{PB}} \propto \dot{\alpha}\rho_{\mathrm{eq}}. \tag{5.11}$$

Finally, tracing over all possible states q and p, while weighting with the probability, given by density $\rho_{\mathrm{eq}}(q, p)$ is the same as taking the ensemble average, and we receive following expressions for THz and Raman signals

$$S_{\mathrm{THz}}(t) \propto \big\langle \mu(t)\dot{\mu}(0) \big\rangle \tag{5.12}$$

$$S_{\mathrm{Raman}}(t) \propto \big\langle \alpha(t)\dot{\alpha}(0) \big\rangle, \tag{5.13}$$

where $\langle \cdots \rangle$ denotes the ensemble average. In this way, one has to record the properties μ and $\dot{\mu}$ during an equilibrium MD simulation, where the time derivative $\dot{\mu}$ can be calculated by finite differences.

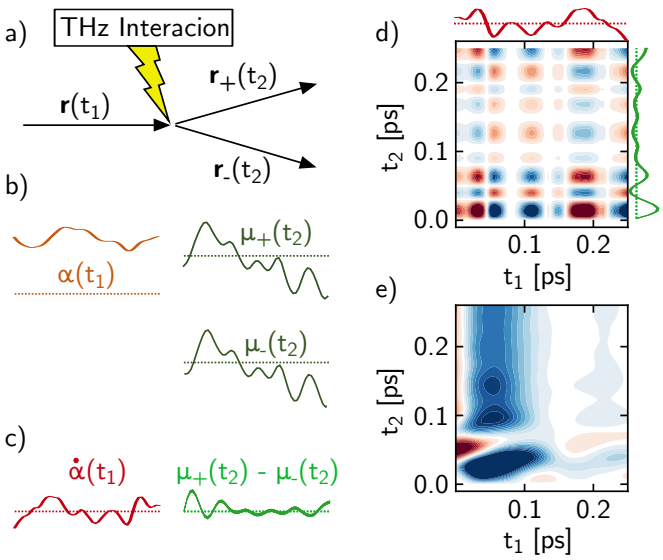

Figure 5.1: Workflow for gaining RTT response, using hybrid equilibrium-non-equilibrium approach on the TL4P force field. *a*) An equilibrium trajectory $r(t_1)$ is generated during t_1. The system is then perturbed by positive and negative THz interaction (5.1) to gain non-equilibrium trajectories $r_+(t_2)$ and $r_-(t_2)$, respectively. *b*) Polarizability $\alpha(t_1)$ is saved during t_1, as well as dipole moments μ_+ and μ_- of the non-equilibrium trajectories. *c*) Of these quantities, the derivative $\dot{\alpha}(t_1)$ is calculated by finite differences from $\alpha(t_1)$. Furthermore, the difference signal $\mu_+(t_2) - \mu_-(t_2)$ is calculated. *d*) The RTT signal is then gained from $(\mu_+(t_2) - \mu_-(t_2))\,\dot{\alpha}(-t_1)$. *e*) Averaging in the order of 10^7 samples finally gives the response R_{RTT}.

5.2.3 Hybrid Approach for Second Order Perturbation

Similarly, the classical limit of the 2D Raman THz signals can be derived from the quantum mechanical response functions

$$\begin{aligned} R_{RTT} &\propto \mathrm{Tr}\big(\hat{\mu}(t_1+t_2)\,[\hat{\mu}(t_1),[\hat{\alpha}(0),\rho_{\mathrm{eq}}]]\,\big) \\ R_{TRT} &\propto \mathrm{Tr}\big(\hat{\mu}(t_1+t_2)\,[\hat{\alpha}(t_1),[\hat{\mu}(0),\rho_{\mathrm{eq}}]]\,\big) \\ R_{TTR} &\propto \mathrm{Tr}\big(\hat{\alpha}(t_1+t_2)\,[\hat{\mu}(t_1),[\hat{\mu}(0),\rho_{\mathrm{eq}}]]\,\big). \end{aligned} \tag{5.14}$$

For second order responses, the nested commutators can be reordered to a product of commutators

$$\begin{aligned} R_{RTT} &\propto \mathrm{Tr}\big(\,[\hat{\mu}(t_1+t_2),\hat{\mu}(t_1)]\,[\hat{\alpha}(0),\rho_{\mathrm{eq}}]\,\big) \\ R_{TRT} &\propto \mathrm{Tr}\big(\,[\hat{\mu}(t_1+t_2),\hat{\alpha}(t_1)]\,[\hat{\mu}(0),\rho_{\mathrm{eq}}]\,\big) \\ R_{TTR} &\propto \mathrm{Tr}\big(\,[\hat{\alpha}(t_1+t_2),\hat{\mu}(t_1)]\,[\hat{\mu}(0),\rho_{\mathrm{eq}}]\,\big). \end{aligned} \tag{5.15}$$

Replacing commutators by Poisson brackets, and applying equations (5.10) and (5.11) gives

$$\begin{aligned} R_{RTT} &\propto \big\langle\, \{\mu(t_1+t_2),\mu(t_1)\}_{\mathrm{PB}}\,\dot{\alpha}(0)\big\rangle \\ R_{TRT} &\propto \big\langle\, \{\mu(t_1+t_2),\alpha(t_1)\}_{\mathrm{PB}}\,\dot{\mu}(0)\big\rangle \\ R_{TTR} &\propto \big\langle\, \{\alpha(t_1+t_2),\mu(t_1)\}_{\mathrm{PB}}\,\dot{\mu}(0)\big\rangle. \end{aligned} \tag{5.16}$$

Evaluation of the remaining poisson bracket (stability matrix) is an expensive procedure. The poisson bracket can be instead replaced by a non-equilibrium approach, where the second interaction explicitly perturbs the trajectory. Shifting times, such that the second interaction is at $t = 0$ $(0 \to -t_1;\ t_1 + t_2 \to t_2)$, gives responses in the form

$$\begin{aligned} R_{RTT} &\propto -\big\langle(\mu_+(t_2) - \mu_-(t_2))\,\dot{\alpha}(-t_1)\big\rangle \\ R_{TRT} &\propto -\big\langle(\mu_+(t_2) - \mu_-(t_2))\,\dot{\mu}(-t_1)\big\rangle \\ R_{TTR} &\propto -\big\langle(\alpha_+(t_2) - \alpha_-(t_2))\,\dot{\mu}(-t_1)\big\rangle\,. \end{aligned} \tag{5.17}$$

This is the hybrid equilibrium non-equilibrium approach of developed by Y. Tanimura and coworkers.[76] The workflow for gaining second order responses (5.17) from MD simulations is illustrated in Figure 6.7 on the example of RTT pulse sequence.

After generating an equilibrium trajectory $r(t_1)$ during a predefined time period t_1, the system is perturbed at $t = 0$ with a THz interaction for R_{RTT} and R_{TTR}, or a Raman interaction for R_{TRT} (By adding forces (5.1) and (5.2) at $t = 0$). Perturbed trajectories for both positive $r_+(t_2)$ and negative perturbations $r_-(t_2)$ are generated (Figure 6.7 *a*). For these three trajectories, relevant dipole moment $\mu(t_1), \mu_+(t_2), \mu_-(t_2)$ and polarizability $\alpha(t_1), \alpha_+(t_2), \alpha_-(t_2)$ are saved (Figure 6.7 *b*). From the dipole and polarizability trajectories, the relevant properties can be calculated. For RTT sequence, this is polarizability derivative $\dot{\alpha}(-t_1)$, and difference of non-equilibrium dipole trajectories $(\mu_+(t_2) - \mu_-(t_2))$ (Figure 6.7 *c*). The response of a single structure is gained as a product thereof (Figure 6.7 *d*). Averaging over approximately 10^7 samples finally yields the response R_{RTT} (Figure 6.7 *e*).

5.3 Room Temperature Water

For the calculation of room temperature spectra, cubic boxes containing 64 water molecules at a density of $0.9965\,\mathrm{g\,cm^{-3}}$ are used with periodic boundary conditions. After equilibrating for

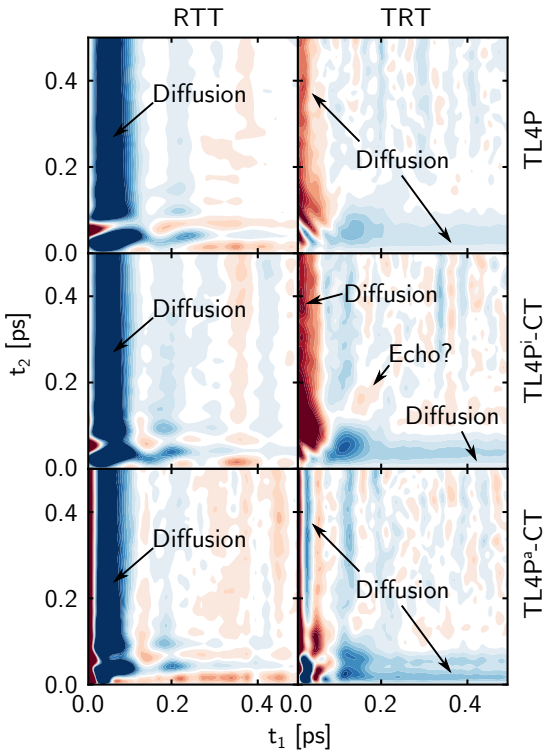

Figure 5.2: Time domain RTT (*left column*) and TRT (*right column*) signals of liquid water at 300 K, calculated from the three force fields TL4P (*top row*), TL4P^{i}-CT (*middle row*), and TL4P^{a2}-CT (*bottom row*).

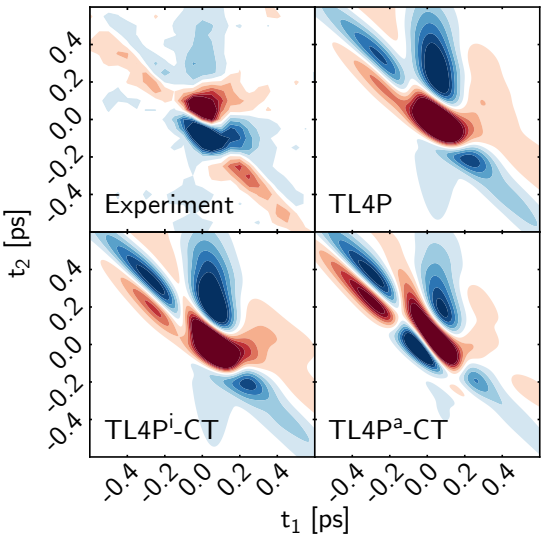

Figure 5.3: Convoluted 2D-Raman-THz signals calculated for four different force fields, TL4P, after addition of charge transfer, and two degrees of anisotropic polarizabilities

7.5 ns, the spectra are calculated using Equation (5.17). Averaging the spectra of approximately 10^7 non-equilibrium trajectories leads to the responses shown in Figure 5.2. Both RTT and TRT responses are combined and convoluted with the instrument response according to Section 2.4. This yields signals, which can be directly compared to the experimental signal (Figure 5.3).

In the same way as for the 1D spectra (Chapter 4), we would expect stepwise improvement of 2D-Raman-THz spectrum when going form TL4P to TL4P^{i}-CT, and finally to the TL4P^{a}-CT force field. Addition of charge transfer (from TL4P to TL4P^{i}-CT) is a rather large incision in the original force field, we expect it to affect the 2D responses accordingly. Since mostly the 200 cm^{-1} band is affected by this change (which lies on the edge of the experimental bandwidth) the resulting changes should also be visible in the convoluted signal. On the other hand, anisotropic polarizability (from TL4P^{i}-CT to TL4P^{a}-CT) is only a small correction. Mostly the 600 cm^{-1} libration mode is affected by this change, which lies well outside the experimental bandwidth. Therefore, no effect on the convoluted signal is expected.

The convoluted signals (Figure 5.3) do not at all follow the expected trends. While addition of charge transfer leaves the general shape of the signal unaffected, anisotropic polarizability completely changes the shape, even introducing an additional node to the central feature. On first glance it looks as if this node originates from an additional, high frequency component contributing to

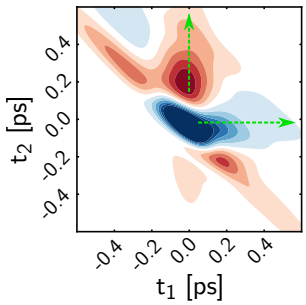

Figure 5.4: Difference spectrum between TL4P^a-CT and TL4P^i-CT illustrates the effect of anisotropic polarizability on the 2D-Raman-THz signal. The signal extends mainly along the t_1 and t_2 axis (green arrows).

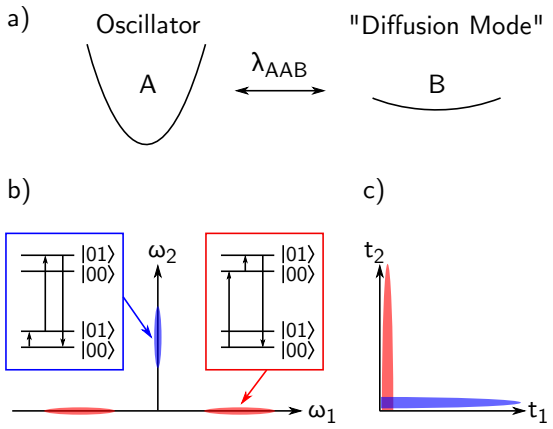

Figure 5.5: *a*) Oscillator A is coupling to low frequency diffusion mode B. *b*) For a distribution of oscillators A, this leads to features along frequency axes. If the diffusion mode is excited first, the signal is on the ω_2 axis (blue feature). If the oscillator A is first excited, the signal spreads along the ω_1 axis (red feature). *c*) In time domain, this translates to elongated features along t_1 and t_2 axis (using same color coding as in frequency domain).

the signal. Inspecting the difference signal (Figure 5.4) shows, that the additional anisotropic contribution is slowly oscillating. The additional node in the TL4P^a-CT spectrum therefore originates from two slowly oscillating contributions which partially cancel. We further note, that the anisotropic contribution (Figure 5.4) has similar features as the purely isotropic signal of TL4P^i-CT, but with inverted sign.

A possible explanation for this unexpected behaviour can be found when considering diffusion and relaxation processes. These are the processes, which set apart liquids from solids. In the vibrational density of states, they appear at very low frequencies ($\omega \to 0$). We have seen in Chapter 3, that low frequency oscillators can couple very effectively to high frequency oscillators (Figure 3.1, $w \to 0$). This hypothetical mechanism (Figure 5.5 *a* and *b*) causes features in time-domain, which are elongated along t_1 and t_2 axis (Figure 5.5 *c*). A strong signal of this kind actually dominates the MD responses of liquid water (Figure 5.2).

Due to the relatively slow oscillations of the convoluted responses we argue, that also the convoluted signal is dominated by diffusion. In this way, the big change which is caused by anisotropic polarizability (from TL4P^i-CT to TL4P^a-CT) has a simple explanation. Anisotropic polarizability not only makes libration modes Raman-active, but has the same effect on rotational diffusion. Therefore, the coupling of oscillations to rotational diffusion becomes visible in the shape of Figure 5.4. The results from amorphous ice simulations will add further confirmation to this hypothesis.

5.4 Amorphous Ice

Structural motifs in amorphous ice are very similar to its liquid counterpart. On the other hand, the dynamic behaviour is in the inhomogeneous limit with a clear separation between slow timescales (diffusion) and fast time scales (randomization of high-frequency modes due to couplings amongst each other). The lack of complicated dynamics in amorphous ice renders it a perfect model system for the study of oscillations in liquid water.

5.4.1 Generation of Amorphous Ice Structures

As in the calculations of liquid water, a cubic box containing 64 water molecules subject to periodic boundary conditions defines our system. The simulation box is first expanded to a density of 0.94 g/cm^3, which is the typical density of low density amorphous ice.[183] Because the amorphous ice structures remain stable for a long time, sampling of the complete phase space requires a variety of starting structures. A collection of 2000 reference structures is generated by randomizing initial velocities of the starting structure, followed by 40 ps of randomization at 500 K. The structures are then equilibrated at 300 K for 40 ps, using a tight thermostat with a coupling constant of 1 ps. Finally, the structures are cooled down to 70 K during 400 ps, using a coupling constant of 20 ps for the thermostat. The whole procedure is illustrated by showing how the temperature of a single box evolves during the equilibration protocol (Figure 5.6 *a*).

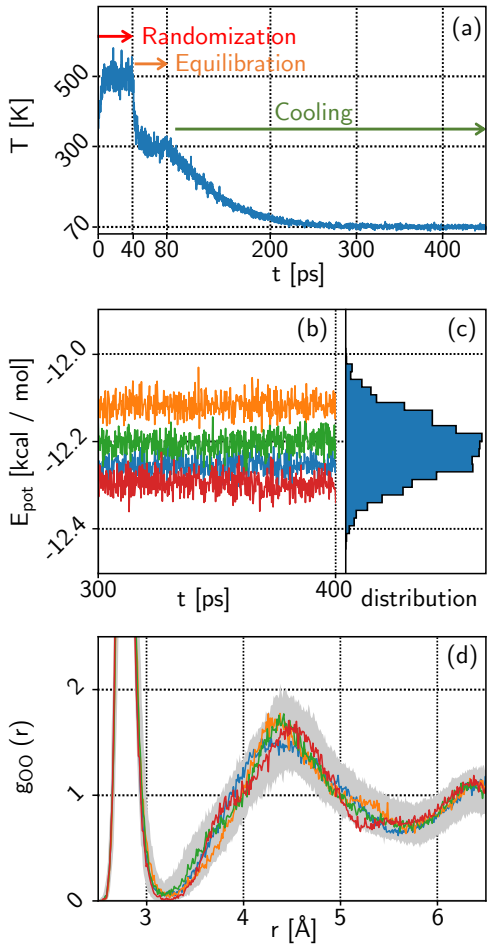

Figure 5.6: (*a*) Simulation protocol for generation of amorphous ice structures, illustrated by the time-dependence of temperature during the generation of one of the structures. (*b*) Potential energy during the last 100 ps of the cooling simulation, shown for four different structures. (*c*) Distribution of average potential energies for the 2000 equilibrated amorphous ice structures. (*d*) Oxygen-oxygen RDF of three selected structures (colored lines). The filled grey area gives the range of values explored by all 2000 structures.

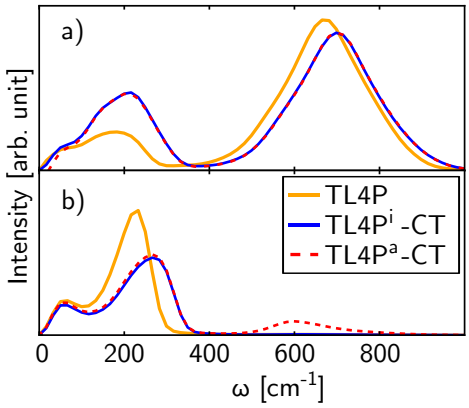

Figure 5.7: *a*) THz and *b*) xx component of Raman spectra, calculated for the three force fields of interest. Signals are calculated directly as the imaginary part of the Fourier transform, without addition of any quantum correction factor.

5.4.2 Structural Properties

After about 300 ps of cooling, the potential energy fluctuates about an average without undergoing further energy drifts (Figure 5.6 *b*). The average potential energy significantly differs in-between different structures, while it stays approximately constant over time. This indicates, that the system is indeed frozen after 300 ps, and that the resulting structures vary significantly. The average energy of all 2000 boxes is distributed approximately like a Gaussian with average E_{pot} being -12.02 kcal/mol and a standard deviation of 0.07 kcal/mol (Figure 5.6 *c*). This suggests, that 2000 structures are adequate in order to describe the complete ensemble. The strong structural differences between different simulation boxes are more directly visible in the $g_{OO}(r)$ (Figure 5.6 *d*). The $g_{OO}(r)$ of single structures deviate from the ensemble average, indicating the local structure of a single box.

5.4.3 Amorphous Ice Spectra

One-dimensional THz (Figure 5.7 *a*) and Raman spectra (Figure 5.7 *b*) have been calculated for from the three force fields. At 70 K, the libration band is clearly separated from the lower frequency signal. Upon variation of force fields, the same trends can be observed as for room temperature spectra. Addition of charge transfer leads to an increased intensity of the hydrogen bond stretching band in the THz spectrum (Figure 5.7 *a*, blue *versus* orange line), while anisotropy turns on the libration band in the Raman spectrum (Figure 5.7 *b*, red *versus* blue line).

Furthermore, the 2D-Raman-THz responses

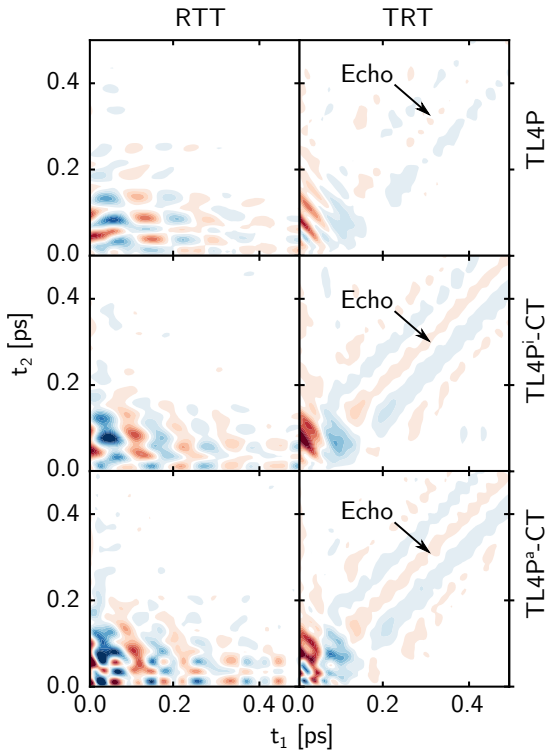

Figure 5.8: The responses RTT and TRT of amorphous ice at 70 K, calculated from TL4P (*top row*), TL4P^i-CT (*middle row*) and TL4P^a-CT (*bottom row*).

have been calculated for the three force fields (Figure 5.8). In amorphous ice, coherence lifetimes are strongly increased, such that the signal expands well past 0.5 ps. While the diffusion signal completely disappears in the solid, the echo signal becomes much more pronounced. By convolution with pulse shapes, the responses are reduced to experimentally accessible bandwidth (Figure 5.9). The corresponding experiment is currently ongoing in our group, and comparison of simulated spectra to experimental amorphous ice spectra will provide further insight into the quality of the different force fields.

Generally, the amorphous ice signal has much lower intensity than the signal originating from liquid water. The convoluted signals plotted in Figure 5.9 are enhanced by a factor of 12 in order to give comparable intensities. A long-lived echo signal appears in the TRT sequence. For amorphous ice, addition of charge transfer and anisotropic polarizability does barely affect the convoluted 2D spectra (Figure 5.9). In contrast to liquid water, the signals from TL4P^i-CT and TL4P^a-CT are almost identical. This supports the hypothesis, that diffusion process are responsible for the big changes at room temperature. For amorphous ice, diffusion becomes negligible, which also causes the diffusion signal to disappear (both in Figure 5.8 and Figure 5.9)

It is surprising, that amorphous ice signals (Figure 5.9) look completely different from the room temperature signals (Figure 5.3). After all, the same oscillations (hydrogen bond bending, stretching, and librations) should be responsible for the signal. One difference between room temperature and amorphous ice is the appearance of the central feature. While in amorphous ice, it consists of a positive and a negative part (much alike the instrument function) the central feature is blurred out at room temperature. This indicates that even the TL4P and TL4P^i-CT signals are dominated by diffusion processes at room temperature.

5.5 Conclusion

Although the changes introduced from the TL4P to the TL4P^a-CT force field strongly improves the description of 1D THz and 1D Raman spectra, the same is not observed in the 2D-Raman-THz spectrum (Figure 5.3). While the changes introduced to the force field selectively modify transition dipoles and transition polarizabilities of diffent modes, they did not consider the finer details (such as mechanical and electrical anharmonicities), which determine the shape of the 2D-Raman-THz signal.

The 2D-Raman-THz spectrum of liquid water is strongly affected by anisotropic polarizability (Figure 5.3, TL4P^i-CT *versus* TL4P^a-CT). This unexpected behaviour can be explained by following hypothesis: Diffusion processes can couple to oscillations. In this way, a 2D-Raman-THz signal can be produced, which extends along t_1 and t_2 axis (Figure 5.5). When anisotropic polarizability is introduced, it gives transition polarizability to rotational diffusion, leading to an additional signal (Figure 5.4). In amorphous ice, on the other hand, diffusion processes are turned off. As a consequence, anisotropic polarizability does not affect the 2D-Raman-THz spectrum (Figure 5.9, TL4P^i-CT *versus* TL4P^a-CT).

For amorphous ice, the central feature in Figure 5.9 consists of a positive and a negative feature (similarly to the instrument response in Figure 1.10 *a*). For room temperature MD water (Figure 5.3), on the other hand, this central feature blurred out and broader than the instrument response function. If this blurred out central feature is a direct consequence of diffusion, we can argue, that even the isotropic signal (Figure 5.3, TL4P^i-CT) is dominated by this diffusion signal. In this aspect, the experimental room temperature

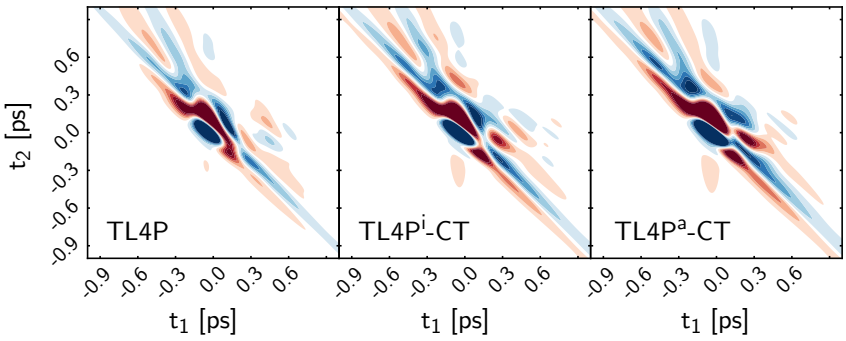

Figure 5.9: Convoluted 2D-Raman-THz responses of amorphous ice at 70 K, calculated with TL4P, TL4P^{i}-CT and TL4P^{a}-CT. Compared to the room temperature spectra (Figure 5.3), the signals are scaled up by a factor of 12.

signal (Figure 5.3, experimental) resembles more the amorphous ice spectra than the room temperature spectra derived from MD. We conclude, that MD simulations strongly overestimate the contribution of diffusion to the 2D-Raman-THz spectra.

As a last remark, the MD simulations suggest the echo to appear in the TRT pulse sequence, whereas experiment observe the echo in the RTT quadrant. In order to discuss this discrepancy, we first need to understand the source of the echo in the MD simulations. The analysis performed in Chapter 6 will assign physical processes to the different spectral features appearing in the amorphous ice response, and therefore simplify discussions of this kind.

Chapter 6

Interpretation of Amorphous Ice Response by 2D Oscillators

6.1 Introduction

Amorphous ice is structurally similar to liquid water but follows much simpler dynamics. At low temperature, diffusion is suppressed and the system motion can be approximated by a set of normal modes. Therefore, it is an ideal system for distinguishing key contributions to the 2D-Raman-THz signal. The responses calculated for amorphous ice show long-lived oscillations (Figure 5.8). In frequency domain (Figure 6.1) this manifests in well-separated peaks; sufficiently narrow to assign specific Feynman pathways to them. The responses we have at hand are derived from molecular dynamics simulation, in which anharmonicities and couplings are captured to full extent.

It is in the very nature of 2D-Raman-THz spectroscopy, that even the most simple systems can cause very complicated peak patterns. Model systems based on harmonic oscillators (Chapters 2 and 3) teach us, that an anharmonicity of a single mode can produce up to four peaks, and a coupling between two modes can cause up to 12 peaks in each pulse sequence. It would be desirable to trace back these complicated peak patterns to the underlying anharmonicity or coupling. Here, this is attempted by fitting the responses to an adequate model system.

The long lived echo signal observed in the TRT sequence shows as a narrow line along the anti-diagonal in frequency domain (arrow in Figure 6.1). This sharp echo line lies on top of a broader spectrum. These broad features can be explained by coupling between distributions of modes which leads to a smeared-out cross peak pattern. Since most of the observed signal seems to originate from cross peaks, an adequate model system needs to take into account pairwise interaction of modes.

Here, we will model the system by a set of oscillators, which can be mechanically and electrically anharmonic. Furthermore, the oscillators can pairwise interact *via* mechanical and electrical couplings. The 2D oscillator model described in Chapter 3 is the minimal example of such a system. Based on the results derived in Chapters 2 and 3, a framework is developed for efficient fitting of condensed phase responses. We will show that this fitting procedure effectively gives a transformation from the response space into a simplified parameter space, where local features describe the relevant mode interactions. This allows us to speculate a bit more profoundly about the origin of different features appearing in the responses.

The model system will be fit to the amorphous ice response of TL4P^a-CT. This force field will be used as an illustration, since all modes are THz- and Raman-active, and can produce most peaks.

6.2 Model System and its Responses

6.2.1 Model System

The motion of a perfectly harmonic system can be described as the sum of independent vibrations on normal mode coordinates $\hat{q}_A$ with Hamiltonians

$$\hat{H}_A^{(0)} = \tfrac{1}{2}\hbar\omega_A \left(\hat{p}_A^2 + \hat{q}_A^2\right). \tag{6.1}$$

In order to describe light-matter interactions, dipole and polarizability operators are needed and are usually expanded in powers of position operators. For most applications, the linear terms

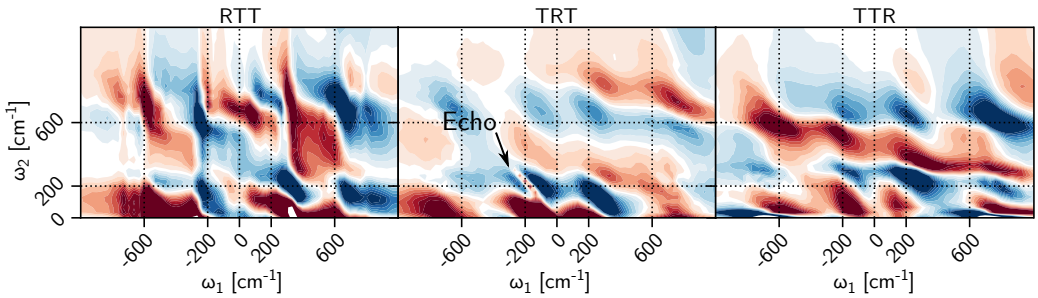

Figure 6.1: Amorphous ice spectra derived from the TL4P^a-CT force field.

$$\hat{\mu}_A^{(0)} = \mu_A \hat{q}_A \tag{6.2}$$

$$\hat{\alpha}_A^{(0)} = \alpha_A \hat{q}_A \tag{6.3}$$

are sufficient. We have seen in Chapters 2 and 3 that the fully harmonic system does not generate any 2D-Raman-THz signal as it allows only single-quantum transitions. The lowest order deviations from the harmonic case are treated as perturbations to the Hamiltonian (mechanical anharmonicity) or corrections to dipole and polarizability operators (electrical anharmonicity) . We consider one-body perturbations

$$\hat{H}_A^{(1)} = \tfrac{1}{2}\hbar\omega_A\sigma_A\hat{q}_A^3 \tag{6.4}$$

$$\hat{\mu}_A^{(1)} = \mu_{AA}\hat{q}_A^2 \tag{6.5}$$

$$\hat{\alpha}_A^{(1)} = \alpha_{AA}\hat{q}_A^2 \tag{6.6}$$

which cause "one-body peaks" (Chapter 2) in the 2D-Raman-THz response. Furthermore, two-body perturbations to the Hamiltonian (mechanical coupling) and polarizability surface (electrical coupling)

$$\hat{H}_{AB}^{(1)} = \tfrac{1}{2}\hbar\omega_A\lambda_{AAB}\hat{q}_A^2\hat{q}_B + \tfrac{1}{2}\hbar\omega_B\lambda_{ABB}\hat{q}_A\hat{q}_B^2 \tag{6.7}$$

$$\hat{\mu}_{AB}^{(1)} = \mu_{AB}\hat{q}_A\hat{q}_B \tag{6.8}$$

$$\hat{\alpha}_{AB}^{(1)} = \alpha_{AB}\hat{q}_A\hat{q}_B \tag{6.9}$$

are responsible for "two-body peaks" in the signal (Chapter 3). The full condensed phase system contains a large collection of modes which can pairwise interact via two-body terms. The total system is then given by sum over all one-body terms, and a sum of pairs of two-body terms ($A < B$ in order to avoid double counting)

$$\hat{H} = \sum_A \left(\hat{H}_A^{(0)} + \hat{H}_A^{(1)}\right) + \sum_{A<B} \hat{H}_{AB}^{(1)} \tag{6.10}$$

$$\hat{\mu} = \sum_A \left(\hat{\mu}_A^{(0)} + \hat{\mu}_A^{(1)}\right) + \sum_{A<B} \hat{\mu}_{AB}^{(1)} \tag{6.11}$$

$$\hat{\alpha} = \sum_A \left(\hat{\alpha}_A^{(0)} + \hat{\alpha}_A^{(1)}\right) + \sum_{A<B} \hat{\alpha}_{AB}^{(1)}. \tag{6.12}$$

6.2.2 Basis Responses

In total, we consider the three one-body perturbations (σ_A, μ_{AA}, α_{AA}) and four two-body perturbations (λ_{AAB}, λ_{ABB}, μ_{AB}, α_{AB}), each of which produces a 2D-Raman-THz response with a characteristic peak pattern. The responses scale linearly with the perturbation, and can as such be interpreted as "basis responses". In the following, we will use the notation, in which a perturbation C gives rise to responses R^C_{RTT}, R^C_{TRT}, and R^C_{TTR}. If we want to refer to the peak patterns of all three pulse sequences, we will use the notation R^C without the subscript.

The one-body perturbation σ_A produces response $R^{\sigma,A}$ (Figure 2.3), μ_{AA} produces $R^{\mu,AA}$ (Figure 2.2), and α_{AA} causes $R^{\alpha,AA}$ (Figure 2.1). For two-body perturbations, the shape of the responses depend furthermore on the relative transition dipoles and polarizabilities of both oscillators in a non-linear way. It turns out, that these responses contain at most two sets of peaks which are scaled by different factors (Figures 3.4, 3.5, and 3.6). These sets of peaks can be viewed as individual basis responses, such that the problem remains linear. Anharmonic coupling λ_{AAB} leads to two basis responses, $R^{\lambda 1,AAB}$ which is scaled by $\mu_A^2\alpha_B$, and $R^{\lambda 2,AAB}$ which is scaled by $\mu_A\mu_B\alpha_A$ (Equations (3.32) to (3.40), illustrated in Figure 3.5). The complementary coupling λ_{ABB} has two basis functions $R^{\lambda 1,ABB}$ which is scaled by $\mu_B^2\alpha_A$ and $R^{\lambda 2,ABB}$ which contains all peaks scaled by $\mu_A\mu_B\alpha_B$ (Figure 3.6). The dipole nonlinearity

μ_{AB} gives rise to basis responses $R^{\mu 1,AB}$ which contains the peaks scaled by $\mu_A\alpha_B$ and $R^{\mu 2,AB}$ which is scaled by $\mu_B\alpha_A$ (quations (3.23) to (3.31), illustrated in Figure 3.4). Lastly, in the response generated by the nonlinearity α_{AB} all peaks are scaled by the factor $\mu_A\mu_B$ and it can be interpreted as a single basis response $R^{\alpha,AB}$ (Equations (3.20) to (3.22), illustrated in Figure 3.3). In total, we count three one-body basis responses, and 7 two-body responses.

In the same way that the system is the sum of all one-body responses for all oscillators, and sum of all two-body responses over all pairs of oscillators, the total response is:

$$\begin{aligned} R = \sum_A \Big(& \sigma_A\mu_A^2\alpha_A R^{\lambda,AAA} + \mu_{AA}\mu_A\alpha_A R^{\mu,AA} \\ & + \alpha_{AA}\mu_A^2 R^{\alpha,AA}\Big) \\ + \sum_{A<B} \Big(& \lambda_{AAB}\mu_A^2\alpha_B R^{\lambda 1,AAB} + \lambda_{AAB}\mu_A\mu_B\alpha_A R^{\lambda 2,AAB} \\ & + \lambda_{ABB}\mu_B^2\alpha_A R^{\lambda 1,ABB} + \lambda_{ABB}\mu_A\mu_B\alpha_B R^{\lambda 2,ABB} \\ & + \mu_{AB}\mu_A\alpha_B R^{\mu 1,AB} + \mu_{AB}\mu_B\alpha_A R^{\mu 2,AB} \\ & + \alpha_{AB}\mu_A\mu_B R^{\alpha,AB}\Big). \end{aligned} \tag{6.13}$$

The complete response is given as an expansion of many basis responses. The expansion coefficients are combinations of the perturbations with transition dipoles and polarizabilities. Fitting of the model response (6.13) to a realistic system response will yield information about these expansion coefficients.

6.2.3 Continuum of States

The number of modes present in condensed phase is so enormous that they are usually not counted individually, but rather described by a continuous density of states $D(\omega)$. The variable ω acts thereby as a collective variable which groups all modes of the same frequency. In this description, one-body properties ($c_A \in \{\sigma_A, \mu_{AA}, \alpha_{AA}\}$) become functions of a single frequency variable $c_A \rightarrow c_A(\omega_A)$ and are scaled by the number of oscillators $D(\omega_A)$. Two-body properties ($c_{AB} \in \{\lambda_{AAB}, \lambda_{ABB}, \mu_{AB}, \alpha_{AB}\}$) will become functions of two frequencies $c_{AB} \rightarrow c_{AB}(\omega_A, \omega_B)$ and are scaled by the number of oscillator pairs $D(\omega_A)D(\omega_B)$. Since the collective variable ω_A represents a collection of oscillators, a parameter c_A can take a distribution of values. The parameter $c_A(\omega_A)$ is then understood as the average value of this distribution.

The model system (6.10) to (6.12) can be translated into the continuum picture, by applying the transformation $c_A \rightarrow D(\omega_A)c_A(\omega_A)$ to one-body properties, and $c_{AB} \rightarrow D(\omega_A)D(\omega_B)c_{AB}(\omega_A, \omega_B)$ to two-body properties, and replacing sums by integrals. Equations (6.10) to (6.12) then become:

$$\begin{aligned} \hat{H} = & \int_0^\infty d\omega_A\ D(\omega_A)\left\{\hat{H}_A^{(0)}(\omega_A) + \hat{H}_A^{(1)}(\omega_A)\right\} \\ & + \int_0^\infty d\omega_A \int_0^{\omega_A} d\omega_B\ D(\omega_A)D(\omega_B)\hat{H}_{AB}^{(1)}(\omega_A, \omega_B) \end{aligned} \tag{6.14}$$

$$\begin{aligned} \hat{\mu} = & \int_0^\infty d\omega_A\ D(\omega_A)\left\{\hat{\mu}_A^{(0)}(\omega_A) + \hat{\mu}_A^{(1)}(\omega_A)\right\} \\ & + \int_0^\infty d\omega_A \int_0^{\omega_A} d\omega_B\ D(\omega_A)D(\omega_B)\hat{\mu}_{AB}^{(1)}(\omega_A, \omega_B) \end{aligned} \tag{6.15}$$

$$\begin{aligned} \hat{\alpha} = & \int_0^\infty d\omega_A\ D(\omega_A)\left\{\hat{\alpha}_A^{(0)}(\omega_A) + \hat{\alpha}_A^{(1)}(\omega_A)\right\} \\ & + \int_0^\infty d\omega_A \int_0^{\omega_A} d\omega_B\ D(\omega_A)D(\omega_B)\hat{\alpha}_{AB}^{(1)}(\omega_A, \omega_B). \end{aligned} \tag{6.16}$$

The resulting responses will undergo the same transitions from Equation 6.13. Before we will write down the full equations for responses in the continuum picture, the parameter space will be simplified in the following Section.

6.2.4 Reduction of Parameter Space

In order to describe the complete system, one would have to keep track of 10 parameters (3 one-body parameters and 7 two-body parameters) which is quite cumbersome. By recognizing relations between different parameters, the problem can be reduced to a set of 4 parameters.

In a first step we will demonstrate that the one-body responses are linearly dependent to corresponding two-body responses and can therefore be omitted. The system Hamiltonian can be perturbed either by the one-body term

$$\sigma_A \propto \frac{\partial^3 V}{\partial q_A^3}, \tag{6.17}$$

leading to the $\mu_A^2\alpha_A R^{\sigma,A}$ response, or by the two-body term

$$\lambda_{AAB} \propto \frac{\partial^3 V}{\partial q_A^2 \partial q_B}, \tag{6.18}$$

which produces the two terms $\mu_A^2\alpha_B R^{\lambda 1,AAB}$ and $\mu_A\mu_B\alpha_A R^{\lambda 2,AAB}$. If the coordinate q_A is identical to q_B, the two perturbations σ_A and λ_{AAB} cannot be distinguished and therefore yield identical responses. Moreover, equal coordinates q_A and q_B gives the two factors $\mu_A^2\alpha_B$ and $\mu_A\mu_B\alpha_A$ equal magnitude. We can therefore write

$$R^{\sigma,A} \propto \left(R^{\lambda 1,AAB} + R^{\lambda 2,AAB}\right)_{\omega_A=\omega_B}. \tag{6.19}$$

The same argument can be applied to the perturbations of the dipole moment and polarizability

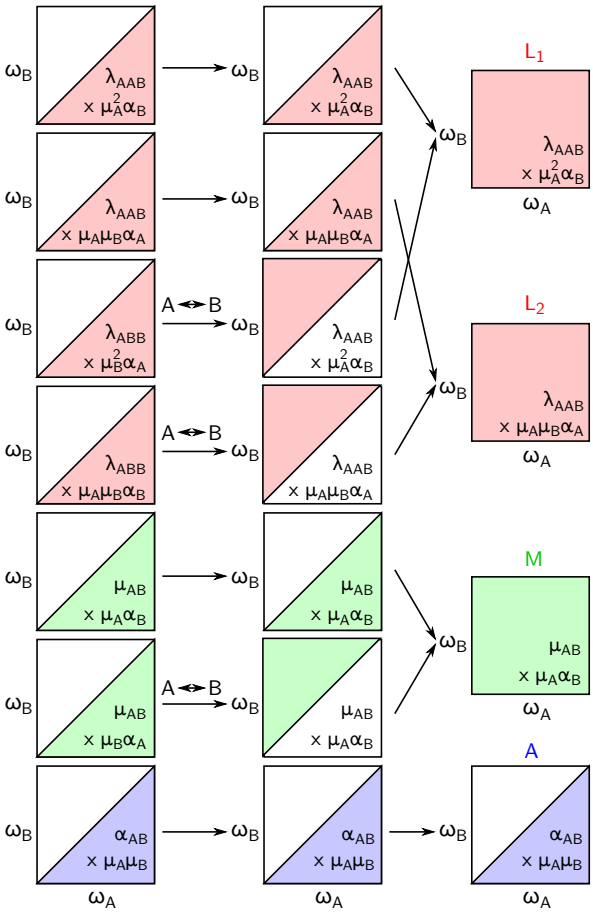

Figure 6.2: Process for the reduction of parameter space of the two-body perturbations. *Left column*: the 7 expansion coefficients of the two-body responses in equation (6.13) are only defined for the range $\omega_B < \omega_A$ in order to avoid double-counting. In this way, they all contain independent information. *Middle column*: by interchange of indices A and B, the meaning of the parameter changes, and the parameter is defined in complementary frequency range $\omega_B > \omega_A$. *Right column*: combining the parameters with the same meaning but different range reduces the complete parameter space to the four parameters L_1, L_2, M and A.

operators which leads to

$$R^{\mu,AA} \propto \left(R^{\mu 1,AB} + R^{\mu 2,AB}\right)_{\omega_A=\omega_B} \tag{6.20}$$

$$R^{\alpha,AA} \propto \left(R^{\alpha,AB}\right)_{\omega_A=\omega_B}. \tag{6.21}$$

In other words, a one-body response can be emulated by a two-body response of two identical oscillators at $\omega_A = \omega_B$. Since the one-body parameters are redundant they can be absorbed into the two-body parameters, leaving us with the 7 two-body responses ($R^{\lambda 2,AAB}$, $R^{\lambda 2,AAB}$, $R^{\lambda 1,ABB}$, $R^{\lambda 2,ABB}$, $R^{\mu 1,AB}$, $R^{\mu 2,AB}$, and $R^{\alpha,AB}$) whose expansion coefficients are all functions of ω_A and ω_B, defined in the range $\omega_B < \omega_A$ (Figure 6.2, left column).

We furthermore recognize that certain parameters are related by interchange of indices A and B. Interchange of indices has two effects: firstly, the meaning of parameters change in the following way

$$\begin{aligned} \mu_A &\leftrightarrow \mu_B & \alpha_A &\leftrightarrow \alpha_B \\ \mu_{AB} &\leftrightarrow \mu_{AB} & \alpha_{AB} &\leftrightarrow \alpha_{AB} \\ \lambda_{AAB} &\leftrightarrow \lambda_{ABB} \end{aligned}$$

where we used $\mu_{BA} = \mu_{AB}$, $\alpha_{BA} = \alpha_{AB}$, and $\lambda_{BBA} = \lambda_{ABB}$, stating that the order of differentiation does not matter. Secondly, the parameters are now defined in the domain $\omega_B > \omega_A$ instead of $\omega_A > \omega_B$. By interchanging indices, the parameter $\lambda_{ABB}\mu_B^2\alpha_A$ is transformed to $\lambda_{AAB}\mu_A^2\alpha_B$, parameter $\lambda_{ABB}\mu_A\mu_B\alpha_B$ changes to $\lambda_{AAB}\mu_A\mu_B\alpha_A$, and $\mu_{AB}\mu_B\alpha_A$ gives $\mu_{AB}\mu_A\alpha_B$ (defined in the frequency range $\omega_B > \omega_A$). The modified parameters are illustrated in Figure 6.2 (middle column).

In the last step, we combine the parameters with the same meaning but different definition ranges to a single parameter, which is then defined in the complete range ω_A and ω_B (Figure 6.2, right column). In this way, the system is reduced to 4 parameters (L_1, L_2, M, and A). While the parameter L_1 reports on the $\mu_A^2\alpha_B$ component, the parameter L_2 describes the $\mu_A\mu_B\alpha_A$ component of the anharmonic coupling λ_{AAB}. Both parameters L_1 and L_2 contain additional contributions of the anharmonicity σ_A along the diagonal. Dipole nonlinearities are described by the parameter M, which reports on the quantity $\mu_{AB}\mu_A\alpha_B$ and has a $\mu_{AA}\mu_A\alpha_A$ diagonal contribution. Nonlinear polarizability is described by the parameter A, which consists of the parameters $\alpha_{AB}\mu_A\mu_B$, and has additional $\alpha_{AA}\mu_A^2$ diagonal contributions. In summary, the four parameters can be written as:

$$L_1(\omega_A,\omega_B) = D(\omega_A)D(\omega_B)\langle\lambda_{AAB}\mu_A^2\alpha_B\rangle(\omega_A,\omega_B) + \delta(\omega_A-\omega_B)D(\omega_A)\langle\sigma_A\mu_A^2\alpha_A\rangle(\omega_A) \tag{6.22}$$

$$L_2(\omega_A,\omega_B) = D(\omega_A)D(\omega_B)\langle\lambda_{AAB}\mu_A\mu_B\alpha_A\rangle(\omega_A,\omega_B) + \delta(\omega_A-\omega_B)D(\omega_A)\langle\sigma_A\mu_A^2\alpha_A\rangle(\omega_A) \tag{6.23}$$

$$M(\omega_A,\omega_B) = D(\omega_A)D(\omega_B)\langle\mu_{AB}\mu_A\alpha_B\rangle(\omega_A,\omega_B) + \delta(\omega_A-\omega_B)D(\omega_A)\langle\mu_{AA}\mu_A\alpha_A\rangle(\omega_A) \tag{6.24}$$

$$A(\omega_A,\omega_B) = D(\omega_A)D(\omega_B)\langle\alpha_{AB}\mu_A\mu_B\rangle(\omega_A,\omega_B) + \delta(\omega_A-\omega_B)D(\omega_A)\langle\alpha_{AA}\mu_A^2\rangle(\omega_A) \tag{6.25}$$

where $\langle\cdots\rangle$ is denotes the expectation value, and δ is the Dirac delta function. Having the values of the parameters, the complete response can then be be written as linear expansion of only four basis responses

$$\begin{aligned} R = &\int_0^\infty d\omega_A \int_0^\infty d\omega_B\ L_1(\omega_A,\omega_B)R^{L1}(t_1,t_2;\omega_A,\omega_B) \\ &+\int_0^\infty d\omega_A \int_0^\infty d\omega_B\ L_2(\omega_A,\omega_B)R^{L2}(t_1,t_2;\omega_A,\omega_B) \\ &+\int_0^\infty d\omega_A \int_0^\infty d\omega_B\ M(\omega_A,\omega_B)R^{M}(t_1,t_2;\omega_A,\omega_B) \\ &+\int_0^\infty d\omega_A \int_0^{\omega_A} d\omega_B\ A(\omega_A,\omega_B)R^{A}(t_1,t_2;\omega_A,\omega_B). \end{aligned} \tag{6.26}$$

The peak patterns of the four basis responses can be extracted from the results of the 2D oscillator (Appendix 3.8, responses $R^{\lambda 1,AAB} \to R^{L1}$, $R^{\lambda 2,AAB} \to R^{L2}$, $R^{\mu 1,AB} \to R^{M}$, and $R^{\alpha,AB} \to R^{A}$). Analytic expressions of the basis responses, including reasonable lineshape functions, are given in Appendix 6.6, Equations (6.35) to (6.46).

6.3 Fitting Strategy

The fact that the model response is as linear combination of basis responses allows us to use efficient fitting algorithms, such as linear regression. In expression (6.26) the parameters L_1, L_2, M, and A are all functions of two frequencies – generally we will write parameter $C(\omega_A,\omega_B)$, acting as expansion coefficient for basis response $R^C(t_1,t_2;\omega_A,\omega_B)$. Since ω_A and ω_B are continuous variables, the responses $R^C(t_1,t_2;\omega_A,\omega_B)$ constitute an infinite basis set.

In order to express the model response (6.26) in a more useful, finite basis set, we start by expanding the parameter $C(\omega_A,\omega_B)$ in terms of local Gaussian basis functions

$$\phi_{ij}(\omega_A,\omega_B) = \exp\left[-\tfrac{1}{2}\left(\tfrac{\omega_A-\omega_i}{\Delta}\right)^2 - \tfrac{1}{2}\left(\tfrac{\omega_B-\omega_j}{\Delta}\right)^2\right], \tag{6.27}$$

where ω_i and ω_j take values on a grid from 0 to $900\,\mathrm{cm}^{-1}$ with $30\,\mathrm{cm}^{-1}$ spacing. For all basis functions, the Gaussian width is set to $\Delta = 20\,\mathrm{cm}^{-1}$. In this basis, the parameter is approximated as

$$C(\omega_A,\omega_B) = \sum_{ij} c_{ij}\phi_{ij}(\omega_A,\omega_B). \tag{6.28}$$

The parameter $C(\omega_A,\omega_B)$ is transformed to the response space by convolving it with the corresponding basis response $R^C(t_1,t_2;\omega_A,\omega_B)$. By using definition (6.28), we receive

$$\begin{aligned} R^C(t_1,t_2) &= \int d\omega_A \int d\omega_B\ C(\omega_A,\omega_B)R^C(t_1,t_2;\omega_A,\omega_B) \\ &= \sum_{ij} c_{ij} \int d\omega_A \int d\omega_B \\ &\qquad \times \phi_{ij}(\omega_A,\omega_B)R^C(t_1,t_2;\omega_A,\omega_B) \\ &\coloneqq \sum_{ij} c_{ij} R^C_{ij}(t_1,t_2). \end{aligned} \tag{6.29}$$

In the last step, the response is expanded in a finite basis set $R^C_{ij}(t_1,t_2)$, which is exactly what we set out to achieve. The basis functions R^C_{ij} are defined as the convolution of the basis response $R^C(t_1,t_2;\omega_A,\omega_B)$ with the Gaussian basis function $\phi_{ij}(\omega_A,\omega_B)$

$$\begin{aligned} R^C_{ij}(t_1,t_2) \coloneqq &\int d\omega_A \int d\omega_B \\ &\times \phi_{ij}(\omega_A,\omega_B)R^C(t_1,t_2;\omega_A,\omega_B) \end{aligned} \tag{6.30}$$

and are computed by numeric convolution on a grid.

The responses we are interested in are functions of two time-variables $R(t_1,t_2)$. For the sake of fitting, they are represented as a one-dimensional array, in which each element maps to a point in response space. For the global fit, the vector R_k will contain data of all three pulse sequences.

$$\begin{aligned} R_{\mathrm{ref}}(t_1,t_2) &\to R_{\mathrm{ref},k} \\ R^C_{ij}(t_1,t_2) &\to R^C_{ij,k}. \end{aligned}$$

Finally, the response (6.29) is fitted to the reference response R_{ref} by ridge regression, in which the loss function

$$\begin{aligned} &\sum_k (R_k - R_{\mathrm{ref},k})^2 + \lambda \sum_{ij} c_{ij}^2 \\ =&\sum_{ij}\left(\sum_k \left(c_{ij}R^C_{ij,k} - R_{\mathrm{ref},k}\right)^2 + \lambda c_{ij}^2\right) \end{aligned} \tag{6.31}$$

is minimized. The term $\lambda\sum_{ij} c_{ij}^2$ thereby restrains the fitting parameters c_{ij} to small values.

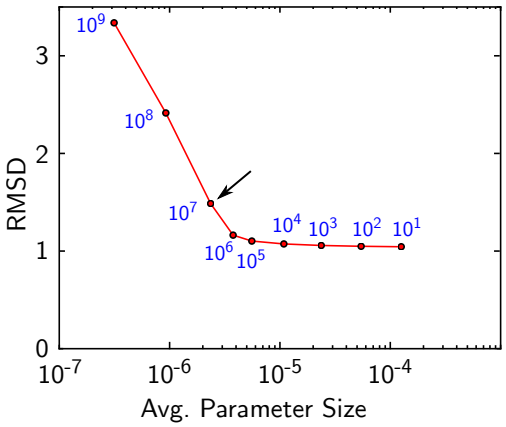

Figure 6.3: RMSD of the fit *versus* the average magnitude of the fit parameters for different values of the regularization parameter λ (blue labels). For higher values of λ, the average parameter size is reduced and RMSD is increased. The chosen value λ is denoted by the arrow.

From the fitted parameters c_{ij}, the smooth function $C(\omega_A, \omega_B)$ is then generated by equation (6.28). In the case of the polarizability parameter A, the complete frequency range is plotted by first symmetrizing the matrix $A_{ij} = A_{ji}$ and then applying equation (6.28). In summary, the fit is performed in following steps:

1. Convolve basis response with Gaussian basis functions in order to receive $R^C_{ij}(t_1, t_2)$ according to Equation (6.30).
2. Transform basis responses $R^C_{ij}(t_1, t_2)$ and reference responses $R_{\mathrm{ref}}(t_1, t_2)$ into one-dimensional arrays $R^C_{ij,k}$ and $R_{\mathrm{ref},k}$ by evaluating at same points in response space.
3. Minimize loss function (6.31) by solving linear system of equations for a fixed value λ yield parameters c_{ij}.

By increasing the magnitude of the regularization parameter λ, the average size of expansion coefficients is reduced (Figure 6.3). This leads to simpler descriptions of the parameter space. Up to a certain point, the simplification of parameter space is achieved without a noteworthy decrease of fit quality. Above a certain value of λ, the parameters are further reduced at the expense of fit accuracy and eventually, all parameters vanish. The regularization parmaeter λ is scanned in powers of ten from 10^1 to 10^9. A value of $\lambda = 10^7$ is chosen, where regularization just starts to affect the fit accuracy (arrows in Figure 6.3).

6.4 Results and Discussion

The amorphous ice responses calculated by MD from the TL4P^a-CT force field is fitted using the model response (6.26). The model response is able to reproduce the signal almost perfectly (Figure 6.8). For the regularization $\lambda = 10^7$, the parameters show a set of localized features (Figure 6.4).

6.4.1 Features in Parameter Space

In parameter space (Figure 6.4), there are local features, peaking mainly at $200\,\mathrm{cm}^{-1}$ and $700\,\mathrm{cm}^{-1}$. The peak positions agree well with vibrational densities of states of amorphous ice (Figure 6.4, 1D plots). Given the fact that no information from 1D spectra entered the fitting procedure this confirms that we received reasonable fit results. Beside diagonal features of hydrogen bond stretching modes and libration modes there are also cross peaks between those bands.

Most of the fitted parameters lie within the regions predicted by vibrational density of states. However, the parameters show some richer structures within these regions. One peculiar substructure is the nodal line, which is observed along the diagonal in the L_1 and L_2 parameters (green arrows in Figure 6.4). Likely, this effect is a direct manifestation of avoided crossing. The MD simulations consider the full extent of mechanical couplings. Therefore, if two oscillators A and B are coupled they may not have the same energy ($\omega_A \neq \omega_B$). Since our model system is based only on first order perturbations, shifts of energy levels are neglected. The energy shifts which occur in realistic systems can partly be imitated by choosing an alternative pair of oscillators with shifted fundamental frequencies. (Figure 6.5).

The presence of diagonal nodes does also suggest, that one-body contributions are not required for the description of the MD signal (These signals would be emulated on the diagonals in parameter space.) It is likely that the contributions from diagonal peaks are negligible due to statistical reasons. We are comparing a quantity $\sigma_A \propto \frac{\partial^3 V}{\partial q_A^3}$ not only with one single term $\lambda_{AAB} \propto \frac{\partial^3 V}{\partial q_A^2 \partial q_B}$, but rather with the sum of contributions

$$\sum_{B \neq A} \frac{\partial^3 V}{\partial q_A^2 \partial q_B}. \tag{6.32}$$

Since the intermolecular low-frequency modes are very delocalized, each mode can couple to a large collection of modes, and the sum (6.32) becomes the dominating contribution.

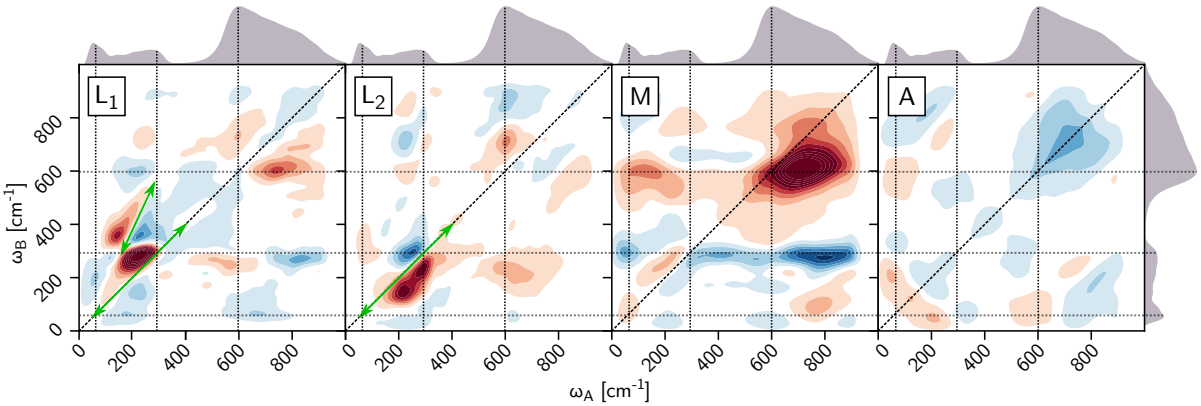

Figure 6.4: Functional dependence of the parameters L_1, L_2, M, and A on the frequencies ω_A and ω_B. The best fit parameters are plotted for the TL4P^a-CT model. Vibrational density of states of TL4P^a-CT are plotted outside of the 2D plots, and peak maxima thereof are indicated by dotted lines. Diagonal nodes in parameters L_1 and L_2 are indicated by green arrows.

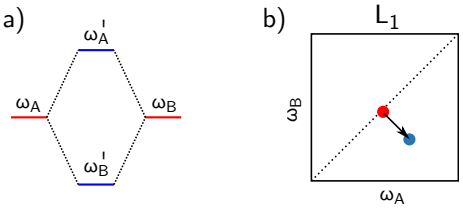

Figure 6.5: (a) The energy levels of two oscillators with fundamental frequencies ω_A and ω_B (red levels) shift upon coupling (to give blue blue levels). The lower energy level is thereby reduced, while the higher level is further increased. (b) In parameter space, this moves ω_A to higher frequency, and ω_B to lower frequency. As a result, the feature is shifted away from the diagonal along the anti-diagonal.

6.4.2 Decomposition of Response

If we want to understand how different parameter space features contribute to the response, it can be instructive to transform single features back to the response space. In order to do so, we separate the frequency axis into two regions; hydrogen bond bending and stretching at frequency $0\,\mathrm{cm}^{-1} < \omega < 500\,\mathrm{cm}^{-1}$, and librations in the frequency range $500\,\mathrm{cm}^{-1} < \omega < 1000\,\mathrm{cm}^{-1}$. In this way, our model parameters, which are functions of two frequencies, are split into four regions each. For the parameters L_1, L_2, and M, there are four independent regions, whereas there are only three independent regions for parameter A. A single feature of the parameter $C \in \{L_1, L_2, M, A\}$ is transformed to the response space by convolution with the basis response R^C over a restricted region

$$\int_{\text{region}} d\omega_A d\omega_B \; C(\omega_A, \omega_B) R^C(t_1, t_2; \omega_A, \omega_B). \quad (6.33)$$

In this way, the spectra are separated into 15 contributions. For the TL4P^a-CT force field the seven main contributions are shown in Figure 6.6. We see that the majority of the signal can be explained by anharmonic couplings (features a to d). On the other hand, libration-libration couplings are dominated by nonlinearities of dipole M (feature f) and polarizability A (feature g).

6.4.3 Source of the Echo

Water force fields seem to predominantly produce an echo signal in the TRT pulse sequence.[92,102] This stands in contrast to experiment, where an echo is observed in the RTT sequence.[79] Due to the wealth of information accessible in the amorphous ice response derived by MD simulations, it has been possible to fit the model response (6.26) to the MD response. In this way, the various spectral features are related to underlying physical properties, which are described by the parameters L_1, L_2, M, and A (Figure 6.4). This also allows us to pinpoint the origin of the echo signal in the MD response.

The fit of the model response suggests that the echo is caused by anharmonic couplings in-between hydrogen bond stretching modes, described by the L_1 parameter (Figure 6.6, feature a). This scenario is very likely with the following reasoning: Much of the response below $400\,\mathrm{cm}^{-1}$ can only be described by anharmonic couplings λ_{AAB} (A fit with only parameters M and A gives very bad results). Anharmonic coupling allows transitions $|00\rangle \leftrightarrow |11\rangle$ and $|01\rangle \leftrightarrow |10\rangle$, which are responsible for the broad cross peaks. In addition, the two-quantum transition $|00\rangle \leftrightarrow |02\rangle$ is allowed. Therefore, an echo signal will naturally appear as by-product of the broader cross peaks. The strength of the echo contribution is determined by the relative frequency ω_B/ω_A, with maximum enhancement of the echo at $\omega_B = 2\omega_A$ due to Fermi resonance.

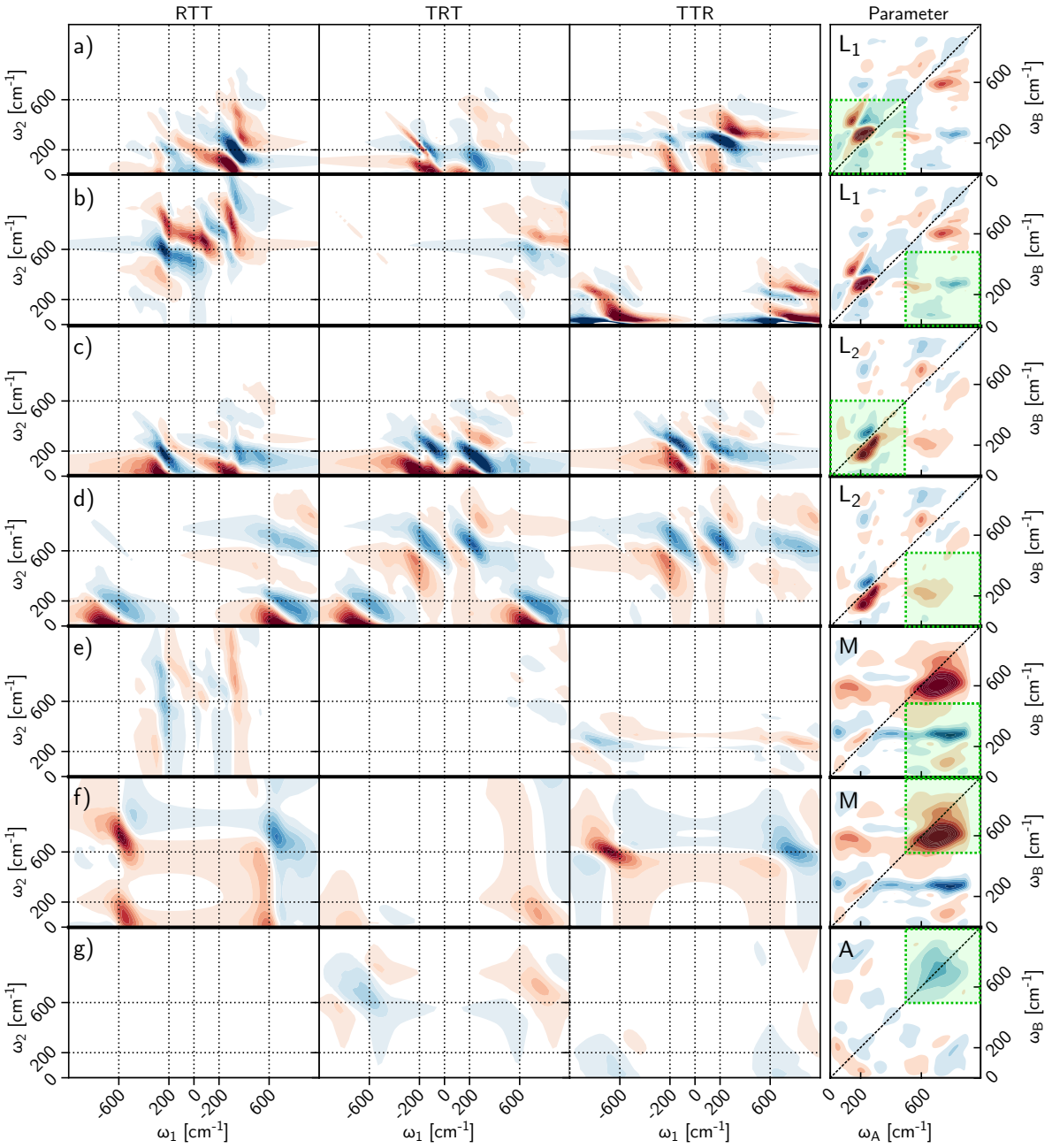

Figure 6.6: Decomposition of the TL4P^a-CT amorphous ice spectra into their main contributions. Each row represents a separate contribution to the total response (The corresponding region in parameter space is highlighted with green color). The first three columns correspond to the three pulse sequences RTT, TRT and TTR, respectively. The last column indicates the feature in parameter space by a black circle.

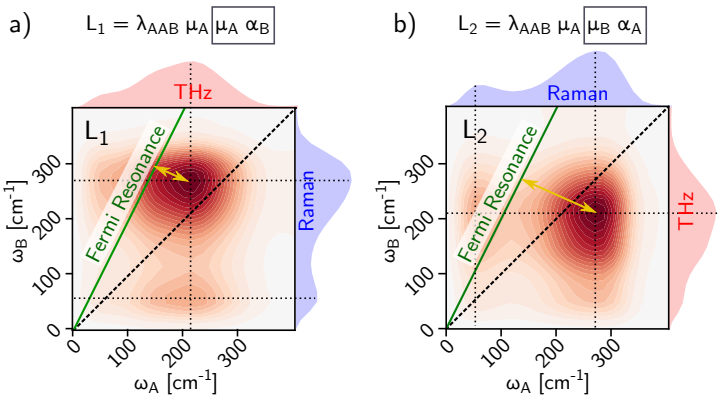

Figure 6.7: Scaling of transition dipoles and polarizabilities in the parameters L_1 and L_2. The green line denotes enhancement by Fermi resonance at $\omega_B = 2\omega_A$. In the case of L_1, the dipole and polarizability contribution is shifted above the diagonal (yellow arrow) and is therefore affected more strongly by Fermi resonances.

The response R^{L2} can only produce an echo in the TRT pulse sequence (Equations (6.35) to (6.37)), whereas R^{L2} has an echo in RTT and TTR quadrants (Equations (6.38) to (6.40)). The reason for the predominance of the echo in TRT quadrant can be explained by considering the differences between 1D Raman and THz spectra. The factor $\lambda_{AAB}\mu_A$ contributes equally to both parameters L_1 and L_2. The main differences between L_1 and L_2 stems from different scaling by transition dipoles and polarizabilies. Roughly speaking, since L_1 is scaled by $\mu_A\alpha_B$, ω_A can be considered the THz axis, and ω_B is considered Raman axis. The L_2 parameter is scaled by $\mu_B\alpha_A$. We can interpret ω_A as Raman axis and ω_B as THz axis. The different contributions can be predicted from 1D THz and Raman spectra (Figure 6.7). The Raman spectrum peaks at a higher frequency than the THz spectrum. Therefore, the contributions to L_1 and L_2 are shifted away from the diagonal. For L_1 (Figure 6.7 a), the contribution is shifted above the diagonal, and the L_2 contribution (Figure 6.7 b) is shifted below. In this case, the L_1 feature is strongly enhanced by Fermi resonance compared to L_2 (Figure 6.7, green line). This leads to enhanced echo signal in the TRT quadrant. The parameters fitted to the TL4P^a-CT response indeed follow this trend, where L_1 is above the diagonal, and L_2 below (Figure 6.4).

6.5 Conclusion

Amorphous ice is structurally similar to liquid water, but shows a simplified dynamics. 2D Raman THz spectra of amorphous ice show a vast amount of spectral features, where contributions of hydrogen bond bending, hydrogen bond stretching, and libration modes can be distinguished, and it is possible to assign Feynman pathways for all features. The 2D spectra are rather congested. This fact can be understood in terms of a 2D oscillator model. In this model, a single anharmonicity gives rise to four peaks, and a pair of coupling oscillators can give a total of 16 peaks. The rather complicated responses with many different peaks have been successfully transformed into the parameter space L_1, L_2, M, and A, where only few contributions are necessary to describe the complete amorphous ice spectra.

The origin of the amorphous ice signals have been identified to be anharmonic couplings λ_{AAB} from hydrogen bond stretching modes to other hydrogen bond stretching modes and librations. Due to the intrinsic nonlinearity of libration motion, libration-libration cross peaks are rather dominated by electrical couplings μ_{AB} and α_{AB}. We have furthermore found, that the echo is caused by mechanical coupling λ_{AAB} in-between hydrogen bond stretching modes. The echo signal thereby appears preferentially in the TRT quadrant. The reason for this might be related to the fact that the hydrogen bond stretching mode appears at higher frequency in the Raman spectrum than in the THz spectrum. The Raman interaction can excite two-quantum transitions of low-frequency hydrogen-bond stretching modes (around $150\,\mathrm{cm}^{-1}$) very effectively, since the resonating modes (around $300\,\mathrm{cm}^{-1}$) are strongly Raman-active.

The fitting procedure used here (Section 6.3) can be readily extended in order to fit experimental data. In order to do so, the basis responses need to be individually convoluted by the instrument response before application of ridge regression.

6.6 Appendix A: Analytical expression of basis responses

Here, the response functions of the reduced parameter space are explicitly written down (Equations (6.35) to (6.46)). As an overview, the intensities of all possible peaks are listed in Table 6.1. The cross-peaks caused by the anharmonicity λ_{AAB} are scaled by frequency-dependent scaling factors

$$\begin{aligned} W_1 &= \frac{1}{2+w} - \frac{1}{w} \\ W_2 &= \frac{1}{2-w} + \frac{1}{w} \\ W_3 &= \frac{1}{2+w} - \frac{1}{2-w} \\ W_4 &= \frac{1}{w}. \end{aligned} \tag{6.34}$$

where $w = \omega_B/\omega_A$. The group of peaks, which is scaled by $\lambda_{AAB}\mu_A^2\alpha_B$ are collected in the R^{L1} responses

$$\begin{aligned} R^{L1}_{RTT} = &+ W_1\Gamma_A \cos\big[-\omega_B t_1 + \omega_A t_2\big] \\ &- W_1\Gamma_F \cos\big[\omega_B t_1 + (\omega_A+\omega_B)t_2\big] \\ &+ W_2\Gamma_G \cos\big[\omega_B t_1 + (\omega_B-\omega_A)t_2\big] \\ &- W_2\Gamma_H \cos\big[\omega_B t_1 + \omega_A t_2\big] \end{aligned} \tag{6.35}$$

$$\begin{aligned} R^{L1}_{TRT} = &+ W_2\Gamma_C \cos\big[-\omega_A + (\omega_B-\omega_A)t_2\big] \\ &- W_1\Gamma_D \cos\big[\omega_A t_1 + (\omega_A+\omega_B)t_2\big] \\ &+ W_3\Gamma_I \cos\big[-\omega_A t_1 + \omega_A t_2\big] \\ &- W_4\Gamma_J \cos\big[\omega_A t_1 + \omega_A t_2\big] \end{aligned} \tag{6.36}$$

$$\begin{aligned} R^{L1}_{TTR} = &+ W_1\Gamma_B \cos\big[-\omega_A t_1 + \omega_B t_2\big] \\ &- W_2\Gamma_E \cos\big[\omega_A t_1 + \omega_B t_2\big] \\ &- W_3\Gamma_K \cos\big[\omega_A t_1 + 2\omega_A t_2\big] \\ &+ W_4\Gamma_L \cos\big[\omega_A t_1\big]. \end{aligned} \tag{6.37}$$

The group of peaks scaled by $\lambda_{AAB}\mu_A\mu_B\alpha_A$ appear in the responses

$$\begin{aligned} R^{L2}_{RTT} = &+ W_1\Gamma_B \cos\big[-\omega_A t_1 + \omega_B t_2\big] \\ &+ W_2\Gamma_C \cos\big[-\omega_A t_1 + (\omega_B-\omega_A)t_2\big] \\ &- W_1\Gamma_D \cos\big[\omega_A t_1 + (\omega_A+\omega_B)t_2\big] \\ &- W_2\Gamma_E \cos\big[\omega_A t_1 + \omega_B t_2\big] \\ &+ W_3\Gamma_I \cos\big[-\omega_A t_1 + \omega_B t_2\big] \\ &- W_4\Gamma_J \cos\big[\omega_A t_1 + \omega_A t_2\big] \\ &- W_3\Gamma_K \cos\big[\omega_A t_1 + 2\omega_A t_2\big] \\ &+ W_4\Gamma_L \cos\big[\omega_A t_1\big] \end{aligned} \tag{6.38}$$

$$\begin{aligned} R^{L2}_{TRT} = &+ W_1\Gamma_A \cos\big[-\omega_B t_1 + \omega_A t_2\big] \\ &- W_1\Gamma_F \cos\big[\omega_B t_1 + (\omega_A+\omega_B)t_2\big] \\ &+ W_2\Gamma_G \cos\big[\omega_B t_1 + (\omega_B-\omega_A)t_2\big] \\ &- W_2\Gamma_H \cos\big[\omega_B t_1 + \omega_A t_2\big] \\ &- W_3\Gamma_K \cos\big[\omega_A t_1 + 2\omega_A t_2\big] \\ &+ W_4\Gamma_L \cos\big[\omega_A t_1\big] \end{aligned} \tag{6.39}$$

$$\begin{aligned} R^{L2}_{TTR} = &+ W_1\Gamma_A \cos\big[-\omega_B t_1 + \omega_A t_2\big] \\ &+ W_2\Gamma_C \cos\big[-\omega_A t_1 + (\omega_B-\omega_A)t_2\big] \\ &- W_1\Gamma_D \cos\big[\omega_A t_1 + (\omega_A+\omega_B)t_2\big] \\ &- W_1\Gamma_F \cos\big[\omega_B t_1 + (\omega_A+\omega_B)t_2\big] \\ &+ W_2\Gamma_G \cos\big[\omega_B t_1 + (\omega_B-\omega_A)t_2\big] \\ &- W_2\Gamma_H \cos\big[\omega_B t_1 + \omega_A t_2\big] \\ &+ W_3\Gamma_I \cos\big[-\omega_A t_1 + \omega_A t_2\big] \\ &- W_4\Gamma_J \cos\big[\omega_A t_1 + \omega_A t_2\big]. \end{aligned} \tag{6.40}$$

The basis responses R^M is caused by electrical anharmonicity μ_{AB} and contains the subset of peaks scaled by $\mu_{AB}\mu_A\alpha_B$

$$\begin{aligned} R^{M}_{RTT} = &+ \Gamma_A \cos\big[-\omega_B t_1 + \omega_A t_2\big] \\ &- \Gamma_F \cos\big[\omega_B t_1 + (\omega_A+\omega_B)t_2\big] \\ &+ \Gamma_G \cos\big[\omega_B t_1 + (\omega_B-\omega_A)t_2\big] \\ &- \Gamma_H \cos\big[\omega_B t_1 + \omega_A t_2\big] \end{aligned} \tag{6.41}$$

$$\begin{aligned} R^{M}_{TRT} = &+ \Gamma_C \cos\big[-\omega_A t_1 + (\omega_B-\omega_A)t_2\big] \\ &- \Gamma_D \cos\big[\omega_A t_1 + (\omega_A+\omega_B)t_2\big] \end{aligned} \tag{6.42}$$

$$\begin{aligned} R^{M}_{TTR} = &+ \Gamma_B \cos\big[-\omega_A t_1 + \omega_B t_2\big] \\ &- \Gamma_E \cos\big[\omega_A t_1 + \omega_B t_2\big]. \end{aligned} \tag{6.43}$$

If nonlinear polarizability couples oscillator A and B, all peaks are scaled by $\alpha_{AB}\mu_A\mu_B$.

Table 6.1: Relative Peak intensity of the four basis functions $\lambda_{1,AB}$, $\lambda_{2,AB}$, μ_{AB}, and α_{AB} for the three pulse sequences of 2D-Raman-THz spectroscopy. The frequency dependent scaling factors $W_1 - W_4$ are defined in equation (3.14).

			RTT				TRT				TTR			
Peak	ω_1	ω_2	R^{L1}_{RTT}	R^{L2}_{RTT}	R^{M}_{RTT}	R^{A}_{RTT}	R^{L1}_{TRT}	R^{L2}_{TRT}	R^{M}_{TRT}	R^{A}_{TRT}	R^{L1}_{TTR}	R^{L2}_{TTR}	R^{M}_{TTR}	R^{A}_{TTR}
A	$-\omega_B$	ω_A	$+W_1$	0	+1	0	0	$+W_1$	0	+ 1	0	$+W_1$	0	0
B	$-\omega_A$	ω_B	0	$+W_1$	0	0	$+W_1$	0	0	+1	$+W_1$	0	+1	0
C	$-\omega_A$	$\omega_B - \omega_A$	0	$+W_2$	0	0	$+W_2$	0	+1	0	0	$+W_2$	0	+1
D	ω_A	$\omega_A + \omega_B$	0	$-W_1$	0	0	$-W_1$	0	-1	0	0	$-W_1$	0	-1
E	ω_A	ω_B	0	$-W_2$	0	0	$-W_2$	0	0	-1	$-W_2$	0	-1	0
F	ω_B	$\omega_A + \omega_B$	$-W_1$	0	-1	0	0	$-W_1$	0	0	0	$-W_1$	0	-1
G	ω_B	$\omega_B - \omega_A$	$+W_2$	0	+1	0	0	$+W_2$	0	0	0	$+W_2$	0	+1
H	ω_B	ω_A	$-W_2$	0	-1	0	0	$-W_2$	0	-1	0	$-W_2$	0	0
I	$-\omega_A$	ω_A	0	$+W_3$	0	0	$+W_3$	0	0	0	0	$+W_3$	0	0
J	ω_A	ω_A	0	$-W_4$	0	0	$-W_4$	0	0	0	0	$-W_4$	0	0
K	ω_A	$2\omega_A$	0	$-W_3$	0	0	0	$-W_3$	0	0	$-W_3$	0	0	0
L	ω_A	0	0	$+W_4$	0	0	0	$+W_4$	0	0	$+W_4$	0	0	0

6.7 Appendix B: Fitted Spectra

The fitted spectrum (with regularization $\lambda = 10^7$) is shown in Figure 6.8 a. By calculating the difference to the reference spectrum (Figure 6.8 c) we can see, that the errors are small compared to the signal intensity.

$$R^A_{RTT} = \; 0 \tag{6.44}$$

$$\begin{aligned} R^A_{TRT} = &+ \Gamma_A \cos\big[-\omega_B t_1 + \omega_A t_2\big] \\ &+ \Gamma_B \cos\big[-\omega_A t_1 + \omega_B t_2\big] \\ &- \Gamma_E \cos\big[\omega_A t_1 + \omega_B t_2\big] \\ &- \Gamma_H \cos\big[\omega_B t_1 + \omega_A t_2\big] \end{aligned} \tag{6.45}$$

$$\begin{aligned} R^A_{TTR} = &+ \Gamma_C \cos\big[-\omega_A t_1 + (\omega_B - \omega_A) t_2\big] \\ &- \Gamma_D \cos\big[\omega_A t_1 + (\omega_A + \omega_B) t_2\big] \\ &- \Gamma_F \cos\big[\omega_B t_1 + (\omega_A + \omega_B) t_2\big] \\ &+ \Gamma_G \cos\big[\omega_B t_1 + (\omega_B - \omega_A) t_2\big] \end{aligned} \tag{6.46}$$

Homogeneous broadening as well as population relaxation of all coherences are described by the Brownian oscillator model [Ref. 74], which gives decay times based on relaxation constants γ_A and γ_B. For all fits to amorphous ice spectra, values $\gamma_A = \gamma_B = 1\,\text{ps}$ were chosen.

$$\begin{aligned} \Gamma_A &= \exp\left[-\tfrac{\gamma_B}{2} t_1 - \tfrac{\gamma_A}{2} t_2\right] \\ \Gamma_B &= \exp\left[-\tfrac{\gamma_A}{2} t_1 - \tfrac{\gamma_A}{2} t_2\right] \\ \Gamma_C &= \exp\left[-\tfrac{\gamma_A}{2} t_1 - \left(\tfrac{\gamma_A}{2} + \tfrac{\gamma_B}{2}\right) t_2\right] \\ \Gamma_D &= \exp\left[-\tfrac{\gamma_A}{2} t_1 - \left(\tfrac{\gamma_A}{2} + \tfrac{\gamma_B}{2}\right) t_2\right] \\ \Gamma_E &= \exp\left[-\tfrac{\gamma_A}{2} t_1 - \tfrac{\gamma_B}{2} t_2\right] \\ \Gamma_F &= \exp\left[-\tfrac{\gamma_B}{2} t_1 - \left(\tfrac{\gamma_A}{2} + \tfrac{\gamma_B}{2}\right) t_2\right] \\ \Gamma_G &= \exp\left[-\tfrac{\gamma_B}{2} t_1 - \left(\tfrac{\gamma_A}{2} + \tfrac{\gamma_B}{2}\right) t_2\right] \\ \Gamma_H &= \exp\left[-\tfrac{\gamma_B}{2} t_1 - \tfrac{\gamma_A}{2} t_2\right] \\ \Gamma_I &= \exp\left[-\tfrac{\gamma_A}{2} (t_1 + t_2)\right] \\ \Gamma_J &= \exp\left[-\tfrac{\gamma_A}{2} (t_1 + t_2)\right] \\ \Gamma_K &= \exp\left[-\tfrac{\gamma_A}{2} (t_1 + 2t_2)\right] \\ \Gamma_L &= \exp\left[-\tfrac{\gamma_A}{2} (t_1 + t_2)\right]. \end{aligned} \tag{6.47}$$

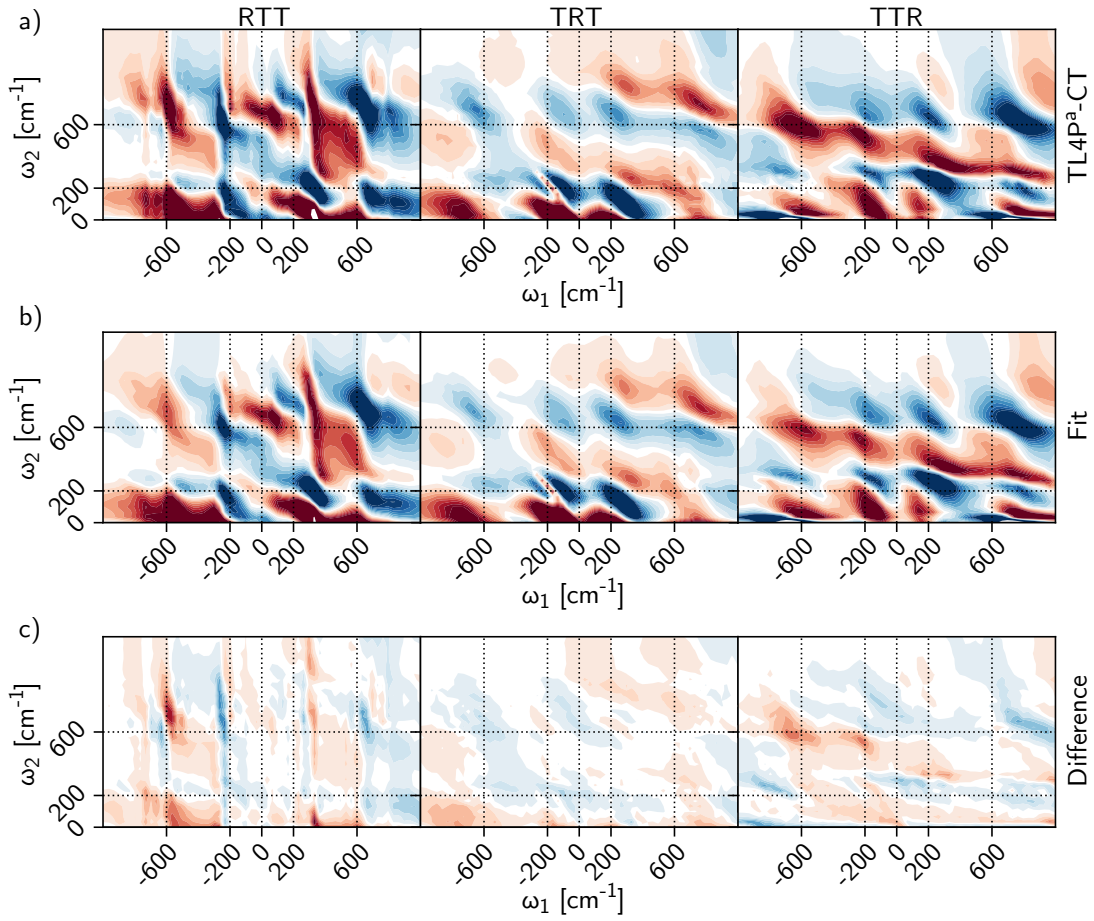

Figure 6.8: *a*) The 2D-Raman-THz response calculated from TL4P^a-CT amorphous ice structures is the fitting target. *b*) The fit result agrees very well with the target response. *c*) The difference spectrum (TL4P^a-CT - fit) gives more quantitative insight into fit quality.

Chapter 7

Conclusion

Our journey started with the goal to develop a forcefield, which can quantitatively reproduce the experimental 2D-Raman-THz spectrum of liquid water. From such a force field, one could potentially understand the signal to full extent by detailed analysis of molecular dynamics trajectories. The starting point was TL4P – a polarizable force field, which was developed on the basis of mixed quantum-mechanical and empirical methods. Among a collection of polarizable force fields, the TL4P model showed best agreement with experiment (Figure 5.3, a *versus* b).[89]

Under the goal to improve the agreement with the experimental 2D-Raman-THz signal, several flaws of the TL4P model have been addressed. TL4P cannot quantitatively reproduce 1D THz absorption and Raman spectra. This would be a basic requirement for a force field that it can correctly predict more complicated spectra such as the 2D-Raman-THz signal. Firstly, the TL4P force field has been shown to severely underestimate the intensity of the $200\,\mathrm{cm}^{-1}$ hydrogen bond stretching mode in the THz absorption spectrum (Figure 4.8 *c*, orange *versus* black line). Secondly, the $600\,\mathrm{cm}^{-1}$ libration band is completely absent in the anisotropic Raman spectrum (Figure 4.8 *d*, orange *versus* black line).

These flaws have been addressed by systematically improving the electrostatic properties of the force field (Chapter 4). Namely, addition of intermolecular charge transfer (in the TL4P^i-CT model) could improve the intensity of the hydrogen bond stretching mode by causing an additional dipole, which depends on the hydrogen bond length. Furthermore, the absence of the libration mode in the Raman spectrum was attributed to the isotropic polarizability used for the TL4P model, meaning the polarizability is orientation independent. The system polarizability is therefore constant during librational motion, and the Raman signal of this band disappears. Making the molecular polarizability slightly anisotropic (in the TL4P^{a2}-CT model) further increased the spectral accuracy by introducing the libration band to the Raman spectrum.

The such obtained series of force fields give a good basis for investigating the effects of charge transfer and anisotropic polarizability on the 2D-Raman-THz spectrum of water. Addition of intermolecular charge transfer corrected the intensity of the hydrogen bond stretching mode in the THz absorption spectrum. We hypothesized that this correction should also improve the 2D-Raman-THz signal. It was however found that the shape of the signal was barely affected by this addition of charge transfer (Figure 5.3, TL4P^i-CT *versus* TL4P). On the other hand, anisotropic polarizability affected the room-temperature signal in a very non-intuitive way, giving rise to an additional node of the main feature (Figure 5.3, TL4P^a-CT *versus* TL4P^i-CT). This is rather unexpected, since anisotropic polarizability mainly affects the libration band, which lies well outside the experimental bandwidth. The strong effect can be interpreted in the way, that anisotropic polarizability can switch on modes, which originate from couplings of intermolecular vibrations to rotational diffusions (Figure 5.5).

Cooling down liquid water in order to induce a glass transition significantly slows down the dynamics. The resulting amorphous ice structures can act as a model system for water (with similar interactions) but with simplified dynamics (Section 5.4). Molecular dynamics studies of amorphous ice have resulted 2D-Raman-THz spectra with a vast amount of well resolved peaks (Figure 6.1). As a consequence, the variety of peaks can be assigned to individual Feynman pathways, giving a detailed interpretation of the signal.

This motivated the interpretation of 2D-Raman-THz spectroscopy from a completely different direction, namely by using simple model systems based on 1D or 2D harmonic oscillators (Chapters 2 and 3). The simplicity of such model systems makes visible the important properties of a sys-

tem, and in what ways these properties influence the 2D-Raman-THz signals. This comes at the expense of having only a very abstract system, where we have no information how the molecules move in space (this allows only for very simple descriptions of spectral line shapes).

Simple oscillator systems have already been thoroughly investigated in the concept of 2D-Raman spectroscopy. It has been shown, that all possible Feynman pathways include at least one two-quantum transition, which is forbidden for the harmonic oscillator. Electrical and mechanical anharmonicity are therefore crucial for describing 2D-Raman-THz spectroscopy, as they lift the selection rules of the harmonic oscillator. If the anharmonicities are treated in the form of small perturbations to the harmonic system, the resulting signal can be expressed as linear combinations of basis responses, which show peak patterns typical for the responsible anharmonicity. In this way, one can disentangle the contributions of electrical and mechanical anharmonicities to the observed signal.

After amending the 1D oscillator responses by spectral line shapes based on exponential decay of the frequency autocorrelation function, this model system can be applied to describe the response of liquid water. Using oscillators around $165\,\mathrm{cm}^{-1}$ (representing hydrogen bond stretching modes) allowed us to reproduce the experimental response almost quantitatively (Figure 2.11a *versus* 2.11b). This fit gives 370 fs for the decay time of the frequency autocorrelation function, suggesting that water is strongly inhomogeneous. Furthermore, partial deconvolution of the water signal has been achieved (Figure 2.11).

In the case of a 2D oscillator (Chapter 3), electrical and mechanical coupling of two modes can do the same job of lifting the selection rules as anharmonicities do in the 1D case. This gives rise to a variety possible cross peaks. It was found, that anharmonic coupling can be an additional cause for the echo signal. In the anharmonic coupling of two modes with $\omega_B = 2\omega_A$, the echo signal is furthermore enhanced by a Fermi resonance. By treating couplings in a perturbative manner the shape of basis responses are also determined for the 2D oscillator model.

Having simple solutions for the 2D oscillator allowed for fitting of the simulated amorphous ice signals (Chapter 6), in which quantitative agreement has been achieved (Figure 6.8). A large part of the signal can be described by mechanical couplings of hydrogen bond stretching amongst each other (Figure 6.4). This process seems to be the leading cause of the echo signal in the simulated spectra. On the other hand, librations interact preferentially via electrical couplings μ_{AB} and α_{AB}. This is not surprising, given the dipole surface of librations is made nonlinear by the nature of rotations.

Having identified the most relevant contributions to the simulated 2D-Raman-THz response of amorphous ice could help us to further improve force fields. For example, we know that the echo signal in the TRT sequence is mainly produced by anharmonic couplings between hydrogen bond stretching modes. By varying the nature of these anharmonic couplings, the echo signal can potentially be shifted into the RTT quadrant (which would better agree with experimental findings). It could prove helpful to further investigate the coupling of vibrations to diffusion modes, as it seems to be an important contribution to the room-temperature spectrum. Variation of box sizes in MD can be potentially used to single out the diffusion signal. The intensity of the diffusion signal should be proportional to the diffusion constant, which is directly related to the size of the simulation box (Figure 4.6).

Acknowledgement

First and foremost, I wish to thank my mentor, Professor Peter Hamm. He always found the important points in a jungle of information and has ways to explain complicated subjects in a simple manner. Without his guidance, this work would not have been possible.

Many thanks also for past and present group members of the Hamm group, for creating such a good working atmosphere. The members of the THz subgroup, Dr. Andrey Shalit, Dr. Saima Ahmed, Arian Berger, Dr. Gustavo Ciardi, and Jabbar Mousavi were always open for discussion. Moreover, I thank Dr. Jan Helbing. and Dr. David Paleček for taking the time to explain various aspects of spectroscopy to me.

I would also like to thank Professor Markus Meuwly and his group members for welcoming me in their group seminars, and for the valuable discussions that spawned from it.

Moreover, I would like to acknowledge the staff members of UZH for keeping the university running smoothly. In paricular, I thank Sascha Giger who always had swift solutions to my IT related problems.

I would like to thank the CMSZH graduate school for creating wonderful events such as the graduate school retreats, as well as for financial support.

The work has been supported by the Swiss National Science Foundation (SNF) through the NCCR MUST.

This work made use of infrastructure provided by S3IT, the Service and Support for Science IT team at the University of Zurich.

Last but not least, I thank my family, Esther, Walter, Eveline, Simon, Sing and Ailin, for constant help and support during these times. A special thanks goes to my girlfriend Sing and my daughter Ailin for making my life more joyful.

Bibliography

[1] P. Ball, Water as an active constituent in cell biology, Chem. Rev. **108**, 74 (2008).

[2] P. Ball, Water: Water - An enduring mystery, Nature **452**, 291 (2008).

[3] I. Brovchenko and A. Oleinikova, Multiple phases of liquid water, ChemPhysChem **9**, 2660 (2008).

[4] O. Mishima and H. E. Stanley, The relationship between liquid, supercooled and glassy water, Nature **396**, 329 (1998).

[5] W. Wagner and A. Pruß, The IAPWS formulation 1995 for the thermodynamic properties of ordinary water substance for general and scientific use, J. Phys. Chem. Ref. Data **31**, 387 (2002).

[6] R. J. Speedy and C. A. Angell, Isothermal compressibility of supercooled water and evidence for a thermodynamic singularity at -45C, J. Chem. Phys. **65**, 851 (1976).

[7] F. Mallamace, C. Corsaro, and H. E. Stanley, A singular thermodynamically consistent temperature at the origin of the anomalous behavior of liquid water, Scientific Reports **2**, 1 (2012).

[8] C. Huang, T. M. Weiss, D. Nordlund, K. T. Wikfeldt, L. G. Pettersson, and A. Nilsson, Increasing correlation length in bulk supercooled H2O, D2O, and NaCl solution determined from small angle x-ray scattering, J. Chem. Phys. **133**, 134504 (2010).

[9] T. S. Carlton, Using heat capacity and compressibility to choose among two-state models of liquid water, J. Phys. Chem. B **111**, 13398 (2007).

[10] F. X. Prielmeier, E. W. Lang, R. J. Speedy, and H. D. Luedemann, Pressure dependence of self diffusion in supercooled light and heavy water, Ber. Bundesges. Phys. Chem **92**, 1111 (1988).

[11] A. Striolo, The mechanism of water diffusion in narrow carbon nanotubes, Nano Lett. **6**, 633 (2006).

[12] W. H. Bragg, The crystal structure of ice, Proc. Phys. Soc. London **34**, 98 (1921).

[13] R. J. Speedy, Stability-limit conjecture. An interpretation of the properties of water, J. Phys. Chem. **86**, 982 (1982).

[14] H. E. Stanley and J. Teixeira, Interpretation of the unusual behavior of H2O and D2O at low temperatures: Tests of a percolation model, J. Chem. Phys. **73**, 3404 (1980).

[15] S. Sastry, P. G. Debenedetti, F. Sciortino, and H. E. Stanley, Singularity-free interpretation of the thermodynamics of supercooled water, Phys. Rev. E **53**, 6144 (1996).

[16] P. H. Poole, F. Sciortino, U. Essmann, and H. E. Stanley, Phase behaviour of metastable water, Nat. Commun. **360**, 324 (1992).

[17] D. H. Kim et al., Maxima in the thermodynamic response and correlation functions of deeply supercooled water, Science **360**, 1589 (2018).

[18] J. C. Palmer, F. Martelli, Y. Liu, R. Car, A. Z. Panagiotopoulos, and P. G. Debenedetti, model of water, Nature **510**, 385 (2014).

[19] P. Wernet et al., The Structure of the First Coordination Shell in Liquid Water, Science **304**, 995 (2004).

[20] S. Naserifar and W. A. Goddard III, Liquid water is a dynamic polydisperse branched polymer, Proc. Natl. Acad. Sci. USA **116**, 1998 (2019).

[21] J. E. Bertie and Z. Lan, Infrared Intensities of Liquids XX: The Intensity of the OH Stretching Band of Liquid Water Revisited, and the Best Current Values of the Optical Constants of H2O(l) at 25°C between 15,000 and 1 cm^{-1}, Appl. Spectrosc. **50**, 1047 (1996).

[22] D. M. Carey and G. M. Korenowski, Measurement of the Raman spectrum of liquid water, J. Chem. Phys. **108**, 2669 (1998).

[23] M. Heyden, J. Sun, S. Funkner, G. Mathias, H. Forbert, M. Havenith, and D. Marx, Dissecting the THz spectrum of liquid water from first principles via correlations in time and space, Proc. Natl. Acad. Sci. USA **107**, 12068 (2010).

[24] H. Yada, M. Nagai, and K. Tanaka, Origin

of the fast relaxation component of water and heavy water revealed by terahertz time-domain attenuated total reflection spectroscopy, Chem. Phys. Lett. **464**, 166 (2008).

[25] I. Popov, P. B. Ishai, A. Khamzin, and Y. Feldman, The mechanism of the dielectric relaxation in water, Phys. Chem. Chem. Phys **18**, 13941 (2016).

[26] D. C. Elton, The origin of the Debye relaxation in liquid water and fitting the high frequency excess response, Phys. Chem. Chem. Phys **19**, 18739 (2017).

[27] C. Choe, J. Lademann, and M. E. Darvin, Depth profiles of hydrogen bound water molecule types and their relation to lipid and protein interaction in the human stratum corneum: In vivo, Analyst **141**, 6329 (2016).

[28] S. T. Roberts, K. Ramasesha, and A. Tokmakoff, Structural rearrangements in water viewed through two-dimensional infrared spectroscopy, Acc. Chem. Res. **42**, 1239 (2009).

[29] P. Hamm and M. T. Zanni, *Concepts and Methods of 2D Infrared Spectroscopy*, Cambridge University Press, Cambridge, 2011.

[30] S. Woutersen, U. Emmerichs, and H. J. Bakker, Femtosecond mid-IR pump-probe spectroscopy of liquid water: Evidence for a two-component structure, Science **278**, 658 (1997).

[31] R. Laenen, C. Rauscher, and A. Laubereau, Dynamics of local substructures in water observed by ultrafast infrared hole burning, Phys. Rev. Lett. **80**, 2622 (1998).

[32] N. Lascoux, G. Gallot, F. Hache, G. M. Gale, S. Bratos, and J. C. Leicknam, Femtosecond dynamics of hydrogen bonds in liquid water: A real time study, Phys. Rev. Lett. **47**, 685 (2000).

[33] P. Salucci et al., Ultrafast Hydrogen-Bond Dynamics in the Infrared, Science **301**, 1698 (2003).

[34] S. Yeremenko, M. S. Pshenichnikov, and D. A. Wiersma, Hydrogen-bond dynamics in water explored by heterodyne-detected photon echo, Chem. Phys. Lett. **369**, 107 (2003).

[35] J. B. Asbury, T. Steinel, K. Kwak, S. A. Corcelli, C. P. Lawrence, J. L. Skinner, and M. D. Fayer, Dynamics of water probed with vibrational echo correlation spectroscopy, J. Chem. Phys. **121**, 12431 (2004).

[36] M. L. Cowan, B. D. Bruner, N. Huse, J. R. Dwyer, B. Chugh, E. T. Nibbering, T. Elsaesser, and R. J. Miller, Ultrafast memory loss and energy redistribution in the hydrogen bond network of liquid H2O, Nature **434**, 199 (2005).

[37] L. Chuntonov, R. Kumar, and D. G. Kuroda, Non-linear infrared spectroscopy of the water bending mode: Direct experimental evidence of hydration shell reorganization?, Phys. Chem. Chem. Phys **16**, 13172 (2014).

[38] S. Ashihara, N. Huse, A. Espagne, E. T. J. Nibbering, and T. Elsaesser, Vibrational couplings and ultrafast relaxation of the O-H bending mode in liquid H2O, Chem. Phys. Lett. **424**, 66 (2006).

[39] J. Lindner, D. Cringus, M. S. Pshenichnikov, and P. Vöhringer, Anharmonic bend-stretch coupling in neat liquid water, Chem. Phys. **341**, 326 (2007).

[40] W. B. Carpenter, J. A. Fournier, R. Biswas, G. A. Voth, and A. Tokmakoff, Delocalization and stretch-bend mixing of the HOH bend in liquid water, J. Chem. Phys. **147**, 084503 (2017).

[41] P. Hamm and A. Shalit, Perspective: Echoes in 2D-Raman-THz spectroscopy, J. Chem. Phys. **146**, 130901 (2017).

[42] H. Y. Hwang, S. Fleischer, N. C. Brandt, B. G. Perkins, M. Liu, K. Fan, A. Sternbach, X. Zhang, R. D. Averitt, and K. A. Nelson, A review of non-linear terahertz spectroscopy with ultrashort tabletop-laser pulses, J. Mod. Opt. **62**, 1447 (2015).

[43] W. Kuehn, K. Reimann, M. Woerner, and T. Elsaesser, Phase-Resolved Two-Dimensional Spectroscopy based on Collinear n-Wave Mixing in the Ultrafast Time Domain, J. Chem. Phys. **130**, 164503 (2009).

[44] W. Kuehn, K. Reimann, M. Woerner, T. Elsaesser, and R. Hey, Two-Dimensional Terahertz Correlation Spectra of Electronic Excitations in Semiconductor Quantum Wells, J. Phys. Chem. B **115**, 5448 (2011).

[45] W. Kuehn, K. Reimann, M. Woerner, T. Elsaesser, R. Hey, and U. Schade, Strong Correlation of Electronic and Lattice Excitations in GaAs/AlGaAs Semiconductor Quantum Wells Revealed by Two-Dimensional Terahertz Spectroscopy, Phys. Rev. Lett. **107**, 067401 (2011).

[46] C. Somma, G. Folpini, K. Reimann, M. Woerner, and T. Elsaesser, Phase-Resolved Two-Dimensional Terahertz Spectroscopy including Off-Resonant Interactions beyond the $\chi(3)$limit, J. Chem. Phys. **144**, 184202 (2016).

[47] T. Elsaesser, K. Reimann, and M. Woerner, Focus: Phase-resolved Nonlinear Terahertz Spectroscopy - From Charge Dynamics in Solids to Molecular Excitations in Liquids, J. Chem. Phys. **142**, 212301 (2015).

[48] J. Lu, Y. Zhang, H. Y. Hwang, B. K. Ofori-Okai, S. Fleischer, and K. A. Nelson, Nonlinear Two-Dimensional Terahertz Photon Echo and Rotational Spectroscopy in the Gas Phase, Proc. Natl. Acad. Sci. USA **113**, 11800 (2016).

[49] G. E. Walrafen, M. R. Fisher, M. S. Hokmabadi, and W. H. Yang, Temperature dependence of the low- and high-frequency Raman scattering from liquid water, J. Chem. Phys. **85**, 6970 (1986).

[50] E. W. Castner, Y. J. Chang, Y. C. Chu, and G. E. Walrafen, The Intermolecular Dynamics of Liquid Water, J. Chem. Phys. **102**, 653 (1995).

[51] C. J. Fecko, J. D. Eaves, and A. Tokmakoff, Isotropic and anisotropic Raman scattering from molecular liquids measured by spatially masked optical Kerr effect spectroscopy, J. Chem. Phys. **117**, 1139 (2002).

[52] R. Torre, P. Bartolini, and R. Righini, Structural relaxation in supercooled water by time-resolved spectroscopy, Nature **428**, 296 (2004).

[53] N. T. Hunt, L. Kattner, R. P. Shanks, and K. Wynne, The dynamics of water-protein interaction studied by ultrafast optical Kerr-effect spectroscopy, J. Am. Chem. Soc. **129**, 3168 (2007).

[54] N. T. Hunt, A. A. Jaye, and S. R. Meech, Ultrafast dynamics in complex fluids observed through the ultrafast optically-heterodyne-detected optical-Kerr-effect (OHD-OKE), Phys. Chem. Chem. Phys. **9**, 2167 (2007).

[55] D. S. Jin et al., Low-frequency modes of aqueous alkali halide solutions: glimpsing the hydrogen bonding bibration, Science **327**, 857 (2010).

[56] K. Mazur, I. A. Heisler, and S. R. Meech, THz spectra and dynamics of aqueous solutions studied by the ultrafast optical Kerr effect, J. Phys. Chem. B **115**, 2563 (2011).

[57] A. Taschin, P. Bartolini, R. Eramo, R. Righini, and R. Torre, Evidence of two distinct local structures of water from ambient to supercooled conditions, Nat. Commun. **4**, 2401 (2013).

[58] D. Vanden Bout, L. J. Muller, and M. Berg, Ultrafast Raman Echoes in Liquid Acetonitrile, Phys. Rev. Lett. **67**, 3700 (1991).

[59] L. J. Muller, D. Vanden Bout, and M. Berg, Broadening of Vibrational Lines by Attractive Forces: Ultrafast Raman Echo Experiments in a CH3I:CDCl3 Mixture, J. Chem. Phys. **99**, 810 (1993).

[60] K. Tominaga, G. P. Keogh, and K. Yoshihara, Liquid Dynamics Studied by Higher Order Non-Linear Optical Spectroscopy, J. Mol. Liquids **66**, 389 (1995).

[61] Y. Tanimura and S. Mukamel, Two-dimensional femtosecond vibrational spectroscopy of liquids, J. Chem. Phys. **99**, 9496 (1993).

[62] A. Tokmakoff, M. J. Lang, D. S. Larsen, G. R. Fleming, V. Chernyak, and S. Mukamel, Two-Dimensional Raman Spectroscopy of Vibrational Interactions in Liquids, Phys. Rev. Lett. **79**, 2702 (1997).

[63] D. A. Blank, L. J. Kaufman, and G. R. Fleming, Fifth-Order Two-Dimensional Raman Spectra of CS2 are Dominated by Third-Order Cascades, J. Chem. Phys. **111**, 3105 (1999).

[64] O. Golonzka, N. Demirdöven, M. Khalil, and A. Tokmakoff, Separation of Cascaded and Direct Fifth-Order Raman Signals using Phase-Sensitive Intrinsic Heterodyne Detection, J. Chem. Phys. **113**, 9893 (2000).

[65] D. A. Blank, L. J. Kaufman, and G. R. Fleming, Direct Fifth-Order Electronically Nonresonant Raman Scattering from CS2 at Room Temperature, J. Chem. Phys. **113**, 771 (2000).

[66] L. J. Kaufman, J. Heo, L. D. Ziegler, and G. R. Fleming, Heterodyne-Detected Fifth-Order Nonresonant Raman Scattering from Room Temperature CS2, Phys. Rev. Lett. **88**, 207402 (2002).

[67] Y. L. Li, L. Huang, R. J. Miller, T. Hasegawa, and Y. Tanimura, Two-Dimensional Fifth-Order Raman Spectroscopy of Liquid Formamide: Experiment and Theory, J. Chem. Phys. **128**, 234507 (2008).

[68] T. Steffen, J. T. Fourkas, and K. Duppen, Time resolved four- and six-wave mixing in liquids. I. Theory, J. Chem. Phys. **105**, 7364 (1996).

[69] T. Steffen and K. Duppen, Population relaxation and non-Markovian frequency fluctuations in third- and fifth-order Raman scattering, Chem. Phys. **233**, 267 (1998).

[70] S. Saito and I. Ohmine, Off-resonant fifth-order nonlinear response of water and CS_2: Analysis based on normal modes, J. Chem. Phys. **108**, 240 (1998).

[71] K. Okumura and Y. Tanimura, Interplay of inhomogeneity and anharmonicity in 2D Raman spectroscopy of liquids, Chem. Phys. Lett. **277**, 159 (1997).

[72] A. Ma and R. M. Stratt, Fifth-order Raman spectrum of an atomic liquid: simulation and instantaneous-normal-mode calculation, Phys. Rev. Lett. **85**, 1004 (2000).

[73] T. I. Jansen, J. G. Snijders, and K. Duppen, Third- and fifth-order nonlinear Raman response of liquid CS2 calculated using a finite field nonequilibrium molecular dynamics method, J. Chem. Phys. **113**, 307 (2000).

[74] K. Okumura and Y. Tanimura, Energy-level diagrams and their contribution to fifth-order Raman and second-order infrared responses: Distinction between relaxation models by two-dimensional spectroscopy, Journal of Physical Chemistry A **107**, 8092 (2003).

[75] S. Saito and I. Ohmine, Fifth-order two-dimensional Raman spectroscopy of liquid water, crystalline ice lh and amorphous ices: Sensitivity to anharmonic dynamics and local hydrogen bond network structure, J. Chem. Phys. **125**, 084506 (2006).

[76] T. Hasegawa and Y. Tanimura, Calculating Fifth-Order Raman Signals for various Molecular Liquids by Equilibrium and Nonequilibrium Hybrid Molecular Dynamics Simulation Algorithms, J. Chem. Phys. **125** (2006).

[77] S. Ahmed, J. Savolainen, and P. Hamm, The Effect of the Gouy Phase in Optical-Pump-THz-Probe Spectroscopy, Opt. Express **22**, 4256 (2014).

[78] A. Berger, G. Ciardi, D. Sidler, P. Hamm, and A. Shalit, Impact of nuclear quantum effects on the structural inhomogeneity of liquid water, Proc. Natl. Acad. Sci. USA **116**, 2458 (2019).

[79] A. Shalit, S. Ahmed, J. Savolainen, and P. Hamm, Terahertz echoes reveal the inhomogeneity of aqueous salt solutions, Nat. Chem. **9**, 273 (2017).

[80] G. Ciardi, A. Berger, P. Hamm, and A. Shalit, Signatures of Intra- and Intermolecular Vibrational Coupling in Halogenated Liquids Revealed by Two-Dimensional Raman-Terahertz Spectroscopy, J. Phys. Chem. Lett. **10**, 4463 (2019).

[81] I. A. Finneran, R. Welsch, M. A. Allodi, T. F. Miller, and G. A. Blake, Coherent Two-Dimensional Terahertz-Terahertz-Raman Spectroscopy, Proc. Natl. Acad. Sci. USA **113**, 6857 (2016).

[82] I. A. Finneran, R. Welsch, M. A. Allodi, T. F. Miller, and G. A. Blake, 2D THz-THz-Raman Photon-Echo Spectroscopy of Molecular Vibrations in Liquid Bromoform, J. Phys. Chem. Lett. **8**, 4640 (2017).

[83] I. B. Magdu, G. J. Mead, G. A. Blake, and T. F. Miller, Interpretation of the THz-THz-Raman Spectrum of Bromoform, J. Phys. Chem. A **123**, 7278 (2019).

[84] C. L. Johnson, B. E. Knighton, and J. A. Johnson, Distinguishing Nonlinear Terahertz Excitation Pathways with Two-Dimensional Spectroscopy, Phys. Rev. Lett. **122**, 073901 (2019).

[85] M. Bass, P. A. Franken, and J. F. Ward, Optical rectification, Phys. Rev. **138**, 28 (1965).

[86] D. F. Nelson and E. H. Turner, Electro-optic and piezoelectric coefficients and refractive index of gallium phosphide, J. Appl. Phys. **39**, 3337 (1968).

[87] P. Hamm and J. Savolainen, Two-Dimensional-Raman-Terahertz Spectroscopy of Water: Theory, J. Chem. Phys. **136**, 094516 (2012).

[88] P. Hamm, J. Savolainen, J. Ono, and Y. Tanimura, Note: Inverted Time-Ordering in Two-Dimensional-Raman-Terahertz Spectroscopy of Water, J. Chem. Phys. **136**, 1 (2012).

[89] P. Hamm, 2D-Raman-THz spectroscopy: A sensitive test of polarizable water models, J. Chem. Phys. **141**, 184201 (2014).

[90] H. Ito, T. Hasegawa, and Y. Tanimura, Calculating two-dimensional THz-Raman-THz and Raman-THz-THz signals for various molecular liquids: The samplers, J. Chem. Phys. **141**, 124503 (2014).

[91] T. Ikeda, H. Ito, and Y. Tanimura, Analysis of 2D THz-Raman Spectroscopy Using a non-Markovian Brownian Oscillator Model with Nonlinear System-Bath Interactions, J. Chem. Phys. **142** (2015).

[92] H. Ito, T. Hasegawa, and Y. Tanimura, Effects of Intermolecular Charge Transfer in Liquid Water on Raman Spectra, J. Phys. Chem. Lett. **7**, 4147 (2016).

[93] M. Cho, Theoretical Description of the Vibrational Echo Spectroscopy by Time-Resolved Infrared-Infrared-Visible Difference-Frequency Generation, J. Chem. Phys. **111**, 10587 (1999).

[94] M. Cho, Theoretical Description of Two-Dimensional Vibrational Spectroscopy by Infrared-Infrared-Visible Sum Frequency

Generation, Phys. Rev. A. **61**, 12 (2000).

[95] P. Tröster, K. Lorenzen, M. Schwörer, and P. Tavan, Polarizable water models from mixed computational and empirical optimization, J. Phys. Chem. B **117**, 9486 (2013).

[96] R. Inaba, K. Tominaga, M. Tasumi, K. A. Nelson, and K. Yoshihara, Observation of homogeneous vibrational dephasing in benzonitrile by ultrafast raman echoes, Chem. Phys. Lett. **211**, 183 (1993).

[97] K. J. Kubarych, C. J. Milne, and R. J. Miller, Fifth-Order Two-Dimensional Raman Spectroscopy: A New Direct Probe of the Liquid State, Int. Rev. Phys. Chem. **22**, 497 (2003).

[98] J. Savolainen, S. Ahmed, and P. Hamm, Two-Dimensional Raman-THz Spectroscopy of Water, Proc. Natl. Acad. Sci. **110**, 20402 (2013).

[99] W. Zhao and J. C. Wright, Doubly vibrationally enhanced four wave mixing: The optical analog to 2d nmr, Phys. Rev. Lett. **84**, 1411 (2000).

[100] R. Guo, F. Fournier, P. M. Donaldson, E. M. Gardner, I. R. Gould, and D. R. Klug, Detection of Complex Formation and Determination of Intermolecular Geometry through Electrical Anharmonic Coupling of Molecular Vibrations using Electron-Vibration-Vibration Two-Dimensional Infrared Spectroscopy, Phys. Chem. Chem. Phys **11**, 8417 (2009).

[101] M. Grechko, T. Hasegawa, F. D'Angelo, H. Ito, D. Turchinovich, Y. Nagata, and M. Bonn, Coupling Between Intra-and Intermolecular Motions in Liquid Water Revealed by Two-Dimensional Terahertz-Infrared-Visible Spectroscopy, Nat. Commun. **9** (2018).

[102] H. Ito, J. Y. Jo, and Y. Tanimura, Notes on simulating two-dimensional Raman and terahertz-Raman signals with a full molecular dynamics simulation approach, Struct. Dyn. **2** (2015).

[103] Z. Pan, T. Wu, T. Jin, Y. Liu, Y. Nagata, R. Zhang, and W. Zhuang, Low Frequency 2D Raman-THz Spectroscopy of Ionic Solution: A Simulation Study, J. Chem. Phys. **142** (2015).

[104] H. Ito and Y. Tanimura, Simulating Two-Dimensional Infrared-Raman and Raman Spectroscopies for Intermolecular and Intramolecular Modes of Liquid Water, J. Chem. Phys. **144** (2016).

[105] P. W. Atkins and R. S. Friedman, *Molecular Quantum Mechanics*, Oxford University Press, 2010.

[106] C. Cohen-Tannoudji, B. Diu, and F. Laloe, *Quantum Mechanics, Volume 2*, Wiley-VCH, 1991.

[107] J. D. Eaves, J. J. Loparo, C. J. Fecko, S. T. Roberts, A. Tokmakoff, and P. L. Geissler, Hydrogen bonds in liquid water are broken only fleetingly, Proc. Natl. Acad. Sci. USA **102**, 13019 (2005).

[108] F. Perakis and P. Hamm, Two-Dimensional Infrared Spectroscopy of Supercooled Water, J. Phys Chem. B **115**, 5289 (2011).

[109] S. Habershon, T. E. Markland, and D. E. Manolopoulos, Competing quantum effects in the dynamics of a flexible water model, J. Chem. Phys. **131**, 024501 (2009).

[110] D. Sidler, M. Meuwly, and P. Hamm, An efficient water force field calibrated against intermolecular THz and Raman spectra, J. Chem. Phys. **148**, 244504 (2018).

[111] P. G. Debenedetti, Supercooled and glassy water, J. Phys.: Condens.Matter **15**, R1669 (2003).

[112] A. Tokmakoff, Structural Rearrangements in Water Viewed Through Two-Dimensional Infrared Spectroscopy, Acc. Chem. Res **42**, 1239 (2009).

[113] R. A. Nicodemus, S. A. Corcelli, J. L. Skinner, and A. Tokmakoff, Collective hydrogen bond reorganization in water studied with temperature-dependent ultrafast infrared spectroscopy, J. Phys. Chem. B **115**, 5604 (2011).

[114] K. Ramasesha, L. De Marco, A. Mandal, and A. Tokmakoff, Water vibrations have strongly mixed intra- and intermolecular character, Nat. Chem. **5**, 935 (2013).

[115] F. N. Keutsch and R. J. Saykally, Water clusters: Untangling the mysteries of the liquid, one molecule at a time, Proc. Natl Acad. Sci. **98**, 10533 (2001).

[116] S. Palese, J. T. Buontempo, L. Schilling, W. T. Lotshaw, Y. Tanimura, S. Mukamel, and R. J. Miller, Femtosecond two-dimensional Raman spectroscopy of liquid water, J. Phys. Chem. **98**, 12466 (1994).

[117] G. Lamoureux, A. D. MacKerell, and B. Roux, A simple polarizable model of water based on classical Drude oscillators, J. Chem. Phys **119**, 5185 (2003).

[118] G. Lamoureux and B. Roux, Modeling induced polarization with classical Drude oscillators: Theory and molecular dynamics simu-

lation algorithm, J. Chem. Phys. **119**, 3025 (2003).

[119] G. Lamoureux, E. Harder, I. V. Vorobyov, B. Roux, and A. D. MacKerell, A polarizable model of water for molecular dynamics simulations of biomolecules, Chem. Phys. Lett. **418**, 245 (2006).

[120] P. T. Kiss and A. Baranyai, A systematic development of a polarizable potential of water, J. Chem. Phys. **138**, 204507 (2013).

[121] W. Yu, P. E. M. Lopes, B. Roux, A. D. Mackerell, W. Yu, P. E. M. Lopes, B. Roux, and A. D. Mackerell, Six-site polarizable model of water based on the classical Drude oscillator, J. Chem. Phys. **138**, 034508 (2013).

[122] S. W. Rick, A polarizable, charge transfer model of water using the drude oscillator, J. Comput. Chem. **37**, 2060 (2016).

[123] A. J. Stone, Predictions of the properties of water from first principles, Science **315**, 1249 (2007).

[124] J. Liu, W. H. Miller, G. S. Fanourgakis, S. S. Xantheas, S. Imoto, and S. Saito, Insights in quantum dynamical effects in the infrared spectroscopy of liquid water from a semiclassical study with an ab initio-based flexible and polarizable force field, J. Chem. Phys. **135** (2011).

[125] V. Babin, G. R. Medders, and F. Paesani, Toward a universal water model: First principles simulations from the dimer to the liquid phase, J. Phys. Chem. Lett. **3**, 3765 (2012).

[126] C. J. Tainter, P. A. Pieniazek, Y. S. Lin, and J. L. Skinner, Robust three-body water simulation model, J. Chem. Phys. **134**, 184501 (2011).

[127] C. J. Tainter, L. Shi, and J. L. Skinner, Reparametrized E3B (explicit three-body) water model using the TIP4P/2005 model as a reference, J. Chem. Theory Comput. **11**, 2268 (2015).

[128] S. W. Rick, S. J. Stuart, and B. J. Berne, Dynamical Fluctuating Charge Force Fields: Application to Liquid Water, J. Chem. Phys **101**, 6141 (1994).

[129] H. A. Stern, F. Rittner, B. J. Berne, and R. A. Friesner, Combined fluctuating charge and polarizable dipole models: Application to a five-site water potential function, J. Chem. Phys. **115**, 2237 (2001).

[130] P. Ahlström, A. Wallqvist, S. Engström, and B. Jönsson, A molecular dynamics study of polarizable water, Mol. Phys. **68**, 563 (1989).

[131] D. N. Bernardo, Y. Ding, K. Krogh-Jespersen, and R. M. Levy, An anisotropic polarizable water model: Incorporation of all-atom polarizabilities into molecular mechanics force fields, Journal of Physical Chemistry **98**, 4180 (1994).

[132] L. X. Dang, T.-m. Chang, L. X. Dang, and T.-m. Chang, Molecular dynamics study of water clusters , liquid , and liquid vapor interface of water with many-body potentials, J. Chem. Phys. **106**, 8149 (1997).

[133] P. Ren and J. W. Ponder, Polarizable Atomic Multipole Water Model for Molecular Mechanics Simulation, J. Phys. Chem. B **107**, 5933 (2003).

[134] P. Paricaud, M. Pedota, A. A. Chialvo, and P. T. Cummings, From dimer to condensed phases at extreme conditions: Accurate predictions of the properties of water by a Gaussian charge polarizable model, J. Chem. Phys. **122**, 244511 (2005).

[135] G. S. Fanourgakis and S. S. Xantheas, Development of transferable interaction potentials for water. V. Extension of the flexible, polarizable, Thole-type model potential (TTM3-F, v. 3.0) to describe the vibrational spectra of water clusters and liquid water, J. Chem. Phys. **128**, 074506 (2008).

[136] T. Hasegawa and Y. Tanimura, A Polarizable Water Model for Intramolecular and Intermolecular Vibrational Spectroscopies, J. Phys. Chem. B **115**, 5545 (2011).

[137] M. L. Laury, L. P. Wang, V. S. Pande, T. Head-Gordon, and J. W. Ponder, Revised Parameters for the AMOEBA Polarizable Atomic Multipole Water Model, J. Phys. Chem. B **119**, 9423 (2015).

[138] M. Schwörer, C. Wichmann, P. Tavan, M. Schwörer, C. Wichmann, and P. Tavan, A polarizable QM / MM approach to the molecular dynamics of amide groups solvated in water, J. Chem. Phys. **144**, 114504 (2016).

[139] L.-P. Wang, T. Head-Gordon, J. W. Ponder, P. Ren, J. D. Chodera, P. K. Eastman, T. J. Martinez, and V. S. Pande, Systematic Improvement of a Classical Molecular Model of Water, J. Phys. Chem. B **117**, 9956 (2013).

[140] R. Qi, L.-P. Wang, Q. Wang, V. S. Pande, and P. Ren, United polarizable multipole water model for molecular mechanics simulation, Journal of Physical Chemistry B **143**, 014504 (2015).

[141] B. T. Thole, Molecular polarizabilities calcu-

lated with a modified dipole interaction, Chem. Phys. **59**, 341 (1981).

[142] D. Elking, T. O. M. Darden, R. J. Woods, T. Park, and N. Carolina, Gaussian Induced Dipole Polarization Model, J. Comput. Chem. **28**, 1261 (2007).

[143] T. M. Nymand and P. Linse, Ewald summation and reaction field methods for potentials with atomic charges, dipoles, and polarizabilities, J. Chem. Phys. **112**, 6152 (2000).

[144] J. L. Abascal and C. Vega, A general purpose model for the condensed phases of water: TIP4P/2005., J. Chem. Phys. **123**, 234505 (2005).

[145] P.-O. Åstrand, K. Ruud, K. V. Mikkelsen, and T. Helgaker, Atomic Charges of the Water Molecule and the Water Dimer, J. Phys. Chem. A **102**, 7686 (1998).

[146] J. Korchowiec and T. Uchimaru, New energy partitioning scheme based on the self-consistent charge and configuration method for subsystems: Application to water dimer system, J. Chem. Phys. **112**, 1623 (2000).

[147] O. Gálvez, P. C. Gómez, and L. F. Pacios, Variation with the intermolecular distance of properties dependent on the electron density in hydrogen bond dimers, J. Chem. Phys. **115**, 11166 (2001).

[148] E. D. Glendening, Natural energy decomposition analysis: Extension to density functional methods and analysis of cooperative effects in water clusters, J. Phys. Chem. A **109**, 11936 (2005).

[149] R. Kumar, J. R. Schmidt, and J. L. Skinner, Hydrogen bonding definitions and dynamics in liquid water, J. Chem. Phys. **126**, 204107 (2007).

[150] R. Z. Khaliullin, A. T. Bell, and M. Head-Gordon, Electron donation in the water-water hydrogen bond, Chem. Eur. J. **15**, 851 (2009).

[151] H. Torii, Cooperative contributions of the intermolecular charge fluxes and intramolecular polarizations in the far-infrared spectral intensities of liquid water, J. Chem. Theory Comput. **10**, 1219 (2014).

[152] M. W. Lee, J. K. Carr, M. Göllner, P. Hamm, and M. Meuwly, 2D IR spectra of cyanide in water investigated by molecular dynamics simulations, J. Chem. Phys. **139**, 54506 (2013).

[153] A. J. Lee and S. W. Rick, The effects of charge transfer on the properties of liquid water, J. Chem. Phys. **134**, 184507 (2011).

[154] T. A. Kesselring, E. Lascaris, G. Franzese, S. V. Buldyrev, H. J. Herrmann, and H. E. Stanley, Finite-size scaling investigation of the liquid-liquid critical point in ST2 water and its stability with respect to crystallization, J. Chem. Phys. **138** (2013).

[155] W. C. Swope, H. C. Andersen, P. H. Berens, K. R. Wilson, W. C. Swope, H. C. Andersen, P. H. Berens, and K. R. Wilson, computer simulation method for the caluculation of equilibrium constats for the formation of physical clusters of molecules: Application to small water clusters, J. Chem. Phys **637**, 637 (1982).

[156] V. Kräutler, W. F. Van Gunsteren, and P. H. Hünenberger, A fast SHAKE algorithm to solve distance constraint equations for small molecules in molecular dynamics simulations, J. Comput. Chem. **22**, 501 (2001).

[157] G. Bussi, D. Donadio, and M. Parrinello, Canonical sampling through velocity rescaling, J. Chem. Phys. **126**, 014101 (2007).

[158] H. Bekker, E. J. Dijkstra, M. K. R. Renardus, and H. J. C. Berendsen, An Efficient, Box Shape Independent Non-Bonded Force and Virial Algorithm for Molecular Dynamics, Mol. Simul. **14**, 137 (1995).

[159] J. Hutter, M. Iannuzzi, F. Schiffmann, and J. Vandevondele, Cp2k: Atomistic simulations of condensed matter systems, Wiley Interdiscip. Rev.-Comput. Mol. Sci. **4**, 15 (2014).

[160] J. VandeVondele and J. Hutter, An efficient orbital transformation method for electronic structure calculations, J. Chem. Phys. **118**, 4365 (2003).

[161] J. P. Perdew, K. Burke, and M. Ernzerhof, Generalized Gradient Approximation Made Simple., Phys. Rev. Lett. **77**, 3865 (1996).

[162] j. vandevondele and j. hutter, gaussian basis sets for accurate calculations on molecular systems in gas and condensed phases, j. chem. phys. **127**, 114105 (2007).

[163] S. Goedecker, M. Teter, and J. Hutter, Separable dual-space Gaussian pseudopotentials, Phys Rev. B Condens. Matter **54**, 1703 (1996).

[164] M. Krack, Pseudopotentials for H to Kr optimized for gradient-corrected exchange-correlation functionals, Theor. Chem. Acc. **114**, 145 (2005).

[165] W. F. Murphy, The Rayleigh depolarization ratio and rotational Raman spectrum of wa-

ter vapor and the polarizability components for the water molecule, J. Chem. Phys. **67**, 5877 (1977).

[166] G. Jancso and W. A. Van Hook, Condensed phase isotope effects (especially vapor pressure isotope effects), Chem. Rev. **74**, 689 (1974).

[167] L. B. Skinner, C. Huang, D. Schlesinger, L. G. Pettersson, A. Nilsson, and C. J. Benmore, Benchmark oxygen-oxygen pair-distribution function of ambient water from x-ray diffraction measurements with a wide Q-range, J. Chem. Phys **138**, 074506 (2013).

[168] M. Neumann, Dipole moment fluctuation formulas in computer simulations of polar systems, Molecular Physics **50**, 841 (1983).

[169] K. A. Motakabbir and M. Berkowitz, Isothermal compressibility of SPC/E water, J. Phys. Chem. **94**, 8359 (1990).

[170] I. G. Tironi and W. F. Van Gunsteren, A molecular dynamics simulation study of chloroform, Mol. Phys. **83**, 381 (1994).

[171] B. Dünweg and K. Kremer, Molecular dynamics simulation of a polymer chain in solution Molecular dynamics simulation of a polymer chain in solution, J. Chem. Phys **99**, 6983 (1993).

[172] I.-C. Yeh and G. Hummer, System-size dependence of diffusion coefficients and viscosities from molecular dynamics simulations with periodic boundary conditions, J. Phys. Chem. B **108**, 15873 (2004).

[173] G. S. Kell, Density, Thermal Expansivity, and Compressibility of Liquid Water from 0° to 150°C: Correlations and Tables for Atmospheric Pressure and Saturation Reviewed and Expressed on 1968 Temperature Scale, J. Chem. Eng. Data **20**, 97 (1975).

[174] U. Kaatze, Complex Permittivity of Water as a Function of Frequency and Temperature, J. Chem. Eng. Data **34**, 371 (1989).

[175] K. Krynicki, C. D. Green, and D. W. Sawyer, Pressure and temperature dependence of self-diffusion in water, Faraday Discuss. Chem. Soc **66**, 199 (1978).

[176] K. R. Harris and L. A. Woolf, Temperature and volume dependence of the viscosity of water and heavy water at low temperatures, J. Chem. Eng. Data **49**, 1064 (2004).

[177] G. S. Kell, Precise Representation of Volume Properties of Water at One Atmosphere, J. Chem. Eng. Data **12**, 66 (1967).

[178] S. Iuchi, A. Morita, and S. Kato, Molecular dynamics simulation with the charge response kernel: Vibrational spectra of liquid water and N-methylacetamide in aqueous solution, J. Phys. Chem. B **106**, 3466 (2002).

[179] R. Ramírez, T. López-Ciudad, P. Kumar P, and D. Marx, Quantum corrections to classical time-correlation functions: Hydrogen bonding and anharmonic floppy modes, J. Chem. Phys. **121**, 3973 (2004).

[180] Z. H. Xu and M. Meuwly, Vibrational Spectroscopy and Proton Transfer Dynamics in Protonated Oxalate, J. Phys. Chem. A **121**, 5389 (2017).

[181] K. Mackeprang, Z. H. Xu, Z. Maroun, M. Meuwly, and H. G. Kjaergaard, Spectroscopy and dynamics of double proton transfer in formic acid dimer, Phys. Chem. Chem. Phys. **18**, 24654 (2016).

[182] C. Vega and J. L. F. Abascal, Simulating water with rigid non-polarizable models: a general perspective, Phys. Chem. Chem. Phys. **13**, 19663 (2011).

[183] J. S. Tse and M. L. Klein, Pressure-induced phase transformations in ice, Phys. Rev. Lett. **58**, 1672 (1987).